BOSTON UNIVERSITY

GRADUATE SCHOOL OF ARTS AND SCIENCES

Dissertation

SEARCH FOR NEUTRINOLESS DOUBLE BETA DECAY TO EXCITED STATES OF BARIUM IN KAMLAND-ZEN

by

HASUNG SONG

B.A. Physics, University of California, Berkeley, 2018

Submitted in partial fulfillment of the

requirements for the degree of

Doctor of Philosophy

2026

Approved by

First Reader

Christopher Grant, PhD
Professor of Physics

Acknowledgments

Here go all your acknowledgments. You know, your advisor, funding agency, lab mates, etc., and of course your family.

As for me, I would like to thank Jonathan Polimeni for cleaning up old LaTeX style files and templates so that Engineering students would not have to suffer typesetting dissertations in MS Word. Also, I would like to thank IDS/ISS group (ECE) and CV/CNS lab graduates for their contributions and tweaks to this scheme over the years (after many frustrations when preparing their final document for BU library). In particular, I would like to thank Limor Martin who has helped with the transition to PDF-only dissertation format (no more printing hardcopies – hooray !!!)

The stylistic and aesthetic conventions implemented in this LaTeX thesis/dissertation format would not have been possible without the help from Brendan McDermot of Mugar library and Martha Wellman of CAS.

Finally, credit is due to Stephen Gildea for the MIT style file off which this current version is based, and Paolo Gaudiano for porting the MIT style to one compatible with BU requirements.

Hasung Song

Boston University

Department of Physics

SEARCH FOR NEUTRINOLESS DOUBLE BETA DECAY TO EXCITED STATES OF BARIUM IN KAMLAND-ZEN

HASUNG SONG

Boston University, Graduate School of Arts and Sciences, 2026

Major Professor: Christopher Grant, PhD
Professor of Physics

ABSTRACT

Have you ever wondered why this is called an *abstract*? Weird thing is that its legal to cite the abstract of a dissertation alone, apart from the rest of the manuscript.

Contents

List of Tables

List of Figures

List of Abbreviations

As per BU library instructions, the list of abbreviations must be in alphabetical order by the **abbreviation**, not by the explanation, or it will be returned to you for re-ordering. **This comment must be removed in the final document.**

CAD	.....	Computer-Aided Design
CO	.....	Cytochrome Oxidase
DOG	.....	Difference Of Gaussian (distributions)
FWHM	.....	Full-Width at Half Maximum
LGN	.....	Lateral Geniculate Nucleus
ODC	.....	Ocular Dominance Column
PDF	.....	Probability Distribution Function
$\mathbb{R}^2$	.....	the Real plane

Chapter 1

Introduction

One of the most striking features of the universe is that it exists in a form capable of forming stars, planets, and ultimately life. This fact alone points to a deep asymmetry in nature: matter is abundant, while antimatter is almost entirely absent. In the early universe, following the Big Bang, energy was readily converted into particle–antiparticle pairs under extreme temperatures and densities. According to the known laws of physics, these processes should have produced matter and antimatter in equal quantities, leading to their mutual annihilation as the universe cooled. The survival of matter therefore signals that a subtle but fundamental imbalance must have emerged during the universe's earliest moments, the origin of which remains one of the central open questions in modern physics.

The existence of this imbalance implies that the fundamental symmetries governing particle interactions are not exact. In particular, charge–parity (CP) symmetry determines whether the laws of physics treat matter and antimatter in the same way. Although CP violation has been observed in the quark sector, its measured effects within the Standard Model are far too weak to account for the matter dominance inferred from cosmological observations. This gap between theory and observation suggests that additional sources of CP violation, or entirely new particles and interactions, played a role in shaping the universe we observe today.

Neutrinos offer a compelling window into this missing physics. Unlike other fermions in the Standard Model, neutrinos are exceptionally light, weakly interact-

ing, and exhibit properties that already require physics beyond the Standard Model. Many theoretical frameworks link these unusual features to the origin of the cosmic matter asymmetry through the mechanism of leptogenesis. In such scenarios, CP-violating processes involving heavy neutrino states in the early universe generate an excess of leptons over antileptons, which is later converted into a baryon asymmetry by electroweak interactions. A key ingredient in many of these models is that neutrinos are Majorana particles, identical to their own antiparticles. This possibility can be tested experimentally through the search for neutrinoless double beta decay ($0\nu\beta\beta$), a rare nuclear process whose observation would reveal lepton number violation and provide direct evidence for the Majorana nature of neutrinos and for new physics beyond the Standard Model.

Neutrinoless double beta decay ($0\nu\beta\beta$) is a hypothetical nuclear transition in which two neutrons decay into two protons and two electrons without the emission of neutrinos. If observed, this process would demonstrate the violation of lepton number and provide a direct link between nuclear decay rates and fundamental neutrino properties. While experimental searches for $0\nu\beta\beta$ continue to improve in sensitivity, the interpretation of any observed signal, or increasingly stringent null result, depends critically on the reliability of nuclear matrix element calculations.

At present, theoretical predictions for the nuclear matrix elements governing $0\nu\beta\beta$ differ substantially among nuclear-structure approaches, leading to significant uncertainties in the inferred neutrino mass scale. Reducing these uncertainties is therefore essential for fully realizing the physics potential of $0\nu\beta\beta$ experiments. One promising avenue for constraining nuclear matrix element calculations is provided by measurements of Standard Model two-neutrino double beta decay ($2\nu\beta\beta$), which serve as important benchmarks for nuclear theory. In addition to the well-studied decays to the ground state of the daughter nucleus, double beta decay can also proceed to ex-

cited nuclear states. Although such excited-state transitions are strongly suppressed by reduced phase space, they probe complementary aspects of nuclear structure and provide additional experimental constraints on the models used to calculate $0\nu\beta\beta$ nuclear matrix elements.

In particular, $2\nu\beta\beta$ to excited states of the daughter nucleus ($2\nu\beta\beta^*$) offers a unique opportunity to test nuclear-structure calculations beyond the single ground-state transition. These decays involve different combinations of nuclear wave-function components and intermediate-state contributions, and are accompanied by characteristic gamma-ray cascades as the daughter nucleus de-excites. As a result, excited-state decays provide sensitivity to modeling assumptions that may not be fully constrained by ground-state $2\nu\beta\beta$ data alone. Experimental information on these suppressed channels can therefore help discriminate among competing nuclear models and reduce the spread of predicted $0\nu\beta\beta$ nuclear matrix element calculations.

This thesis focuses on a search for double beta decay of ^{136}Xe to excited states of ^{136}Ba using data from the KamLAND-Zen 800 experiment. Owing to the extreme rarity of these processes and the presence of substantial radioactive and instrumental backgrounds, such a search is inherently challenging. The analysis is sensitive primarily to the most dominant excited-state decay modes and is largely agnostic to the specific excited state involved. Rather than targeting a particular transition, the search is designed to address a more fundamental question: whether any statistically significant indication of excited-state double beta decay can be observed in the available dataset. Establishing an observation, or setting improved limits in the absence of a signal, provides valuable new experimental input for nuclear matrix element calculations and strengthens the interpretation of ^{136}Xe-based searches for $0\nu\beta\beta$.

The remainder of this dissertation is organized as follows. Chapter 2 reviews the

theoretical framework of neutrinos, neutrino mass, and double beta decay, with emphasis on the relationship between two-neutrino and neutrinoless modes and their associated nuclear matrix elements. Subsequent Chapters 3 – 7 describe the KamLAND-Zen detector and dataset, the modeling of signal and background processes, the analysis techniques used to search for excited-state decays, and the resulting constraints and their implications for nuclear theory and future $0\nu\beta\beta$ sensitivity.

Chapter 2

Theory of Neutrinos and Double Beta Decay

While this chapter reviews the theoretical foundations of neutrino mass and lepton number violation, particular emphasis is placed on Standard Model two-neutrino double beta decay ($2\nu\beta\beta$). In addition to serving as an irreducible background to neutrinoless double beta decay ($0\nu\beta\beta$) searches, $2\nu\beta\beta$ to excited nuclear states provides a unique experimental probe of nuclear structure that directly informs the interpretation of $0\nu\beta\beta$ results.

2.1 Neutrinos in the Standard Model

Neutrinos remain the least understood component of the Standard Model (SM) of particle physics [22]. Their elusive nature and extremely weak interactions make them challenging to study, yet they play a central role in both particle physics and cosmology. The modern understanding of neutrinos began in 1914, when James Chadwick used magnetic spectrometry to measure the energy spectrum of electrons emitted in beta decay. He observed that the spectrum was continuous rather than discrete, implying an apparent violation of energy conservation.

To resolve this puzzle, Pauli postulated in 1930 the existence of a new neutral and very light particle that carried away the missing energy [23]. He introduced this idea in his famous letter addressed to the "Radioactive Ladies and Gentlemen." Enrico Fermi later incorporated Pauli's proposal into his theory of beta decay and named the

particle the neutrino, meaning "little neutral one." The neutrino was experimentally detected in 1956 by Cowan and Reines [24], firmly establishing its existence. Since that time, the Standard Model has been extended to include three flavors of neutrinos, each associated with a corresponding charged lepton.

The Standard Model is a gauge theory based on the symmetry group $SU(3)_C \times SU(2)_L \times U(1)_Y$ [22]. Neutrinos participate only in the weak interaction, which is mediated by the charged $W^{\pm}$ bosons and the neutral Z^0 boson, and they carry no electric charge. Their extremely small interaction cross sections make them difficult to detect, but also allow them to propagate over vast distances with little attenuation. This unique property enables neutrinos to serve as powerful messengers from otherwise inaccessible regions of the universe.

2.1.1 Neutrino Interactions

The Standard Model unifies the strong, weak, and electromagnetic interactions within the gauge symmetry $SU(3)_C \times SU(2)_L \times U(1)_Y$. The $SU(3)_C$ sector governs the strong interaction through quantum chromodynamics, while the $SU(2)_L \times U(1)_Y$ sector describes the electroweak interaction. In this framework, the weak interaction is mediated by the charged $W^{\pm}$ bosons and the neutral Z^0 boson.

Neutrinos appear in the Standard Model as components of left handed lepton doublets, which transform as weak isospin doublets under $SU(2)_L$:

$$L_\ell = \begin{pmatrix} \nu_{\ell L} \\ \ell_L \end{pmatrix}, \quad \ell = e, \mu, \tau. \tag{2.1}$$

Here, $\nu_{\ell L}$ and ℓ_L denote the neutrino and charged lepton fields of flavor ℓ, respectively. Only the left handed components of these fermion fields participate in weak interactions. This chiral structure is implemented through the projection operator:

$$P_L = \frac{1 - \gamma_5}{2}, \tag{2.2}$$

where $\gamma_5 = i\gamma^0\gamma^1\gamma^2\gamma^3$ is constructed from the Dirac matrices.

Electroweak interactions are characterized by two quantum numbers: weak isospin I and weak hypercharge Y. The electric charge operator is given by:

$$Q = I_3 + \frac{Y}{2}, \tag{2.3}$$

where I_3 is the third component of weak isospin. For lepton doublets, the total weak isospin is $I = 1/2$ and the hypercharge is $Y = -1$. These assignments correctly reproduce the observed electric charges, yielding $Q = 0$ for neutrinos and $Q = -1$ for charged leptons.

Table 2.1 summarizes the weak isospin, hypercharge, and electric charge assignments for the fermion doublets and singlets in the Standard Model. Right handed charged leptons and quarks are singlets under $SU(2)_L$, with $I = 0$, and therefore do not participate in charged weak interactions. Their hypercharge values are chosen to reproduce the observed electric charges through Eq. 2.3.

The neutrino components of the lepton doublets are referred to as active neutrinos, reflecting their participation in weak interactions. In contrast, hypothetical sterile

			I	I_3	Y	Q
lepton doublet	$L_L \equiv$	$\begin{pmatrix} \nu_{eL} \\ e_L \end{pmatrix}$	$1/2$	$+1/2$	-1	0
			$1/2$	$-1/2$	-1	-1
lepton singlet	e_R		0	0	-2	-1
quark doublet	$Q_L \equiv$	$\begin{pmatrix} u_L \\ d_L \end{pmatrix}$	$1/2$	$+1/2$	$1/3$	$2/3$
			$1/2$	$-1/2$	$1/3$	$-1/3$
quark singlets	u_R		0	0	$4/3$	$2/3$
	d_R		0	0	$-2/3$	$-1/3$

Table 2.1: Weak isospin I, third component of weak isospin I_3, hypercharge Y, and electric charge $Q = I_3 + Y/2$ for fermion doublets and singlets in the Standard Model.

neutrinos would be singlets under the full Standard Model gauge group and would not couple to the $W^{\pm}$ or Z^0 bosons. Within the Standard Model, there is exactly one active neutrino associated with each charged lepton flavor: e, μ, and τ.

Gauge invariance under $SU(2)_L$ dictates the form of the weak charged current and neutral current interactions involving leptons. These interactions are described by the Lagrangian terms:

$$-\mathcal{L}_{\mathrm{CC}} = \frac{g}{\sqrt{2}} \sum_{\ell} \bar{\nu}_{\ell L} \gamma^{\mu} \ell_L W^{+}_{\mu} + \mathrm{h.c.}, \tag{2.4}$$

$$-\mathcal{L}_{\mathrm{NC}} = \frac{g}{2\cos\theta_W} \sum_{\ell} \bar{\nu}_{\ell L} \gamma^{\mu} \nu_{\ell L} Z^0_{\mu}, \tag{2.5}$$

where g is the weak coupling constant and θ_W is the Weinberg angle. The charged current interaction governs processes such as beta decay and double beta decay, while the neutral current interaction allows neutrinos to scatter elastically from matter without changing flavor.

Precision measurements of the invisible decay width of the Z^0 boson provide a direct constraint on the number of light, active neutrino species [25]. The experimentally measured value,

$$N_{\nu} = 2.984 \pm 0.008, \tag{2.6}$$

is consistent with three active neutrino flavors and provides strong experimental support for the Standard Model neutrino sector.

The purely left handed nature of weak interactions in the Standard Model has important consequences for neutrino mass and for processes that violate lepton number. Because only left handed neutrino fields appear in the electroweak Lagrangian, no renormalizable mass term for neutrinos can be constructed using Standard Model fields alone. As a result, neutrinos are massless in the minimal Standard Model. Any mechanism that generates neutrino mass must therefore extend the theory, either

by introducing new fields or by allowing higher dimensional operators. This chiral structure also plays a central role in double beta decay. In particular, the connection between left handed weak currents, neutrino mass, and lepton number violation underlies the theoretical interpretation of both $2\nu\beta\beta$ and $0\nu\beta\beta$ decay processes, which are discussed in detail in the following sections.

2.2 Neutrino Oscillations

The discovery of neutrino oscillations represents one of the most significant breakthroughs in particle physics in recent decades. This achievement was recognized with the 2015 Nobel Prize in Physics, awarded to Art McDonald of the SNO collaboration and Takaaki Kajita of the Super-Kamiokande collaboration [26]. The underlying concept of neutrino flavor oscillations was first proposed by Bruno Pontecorvo in the late 1950s, inspired by the phenomenon of neutral kaon mixing, $K^0 \leftrightarrow \overline{K}^0$ [27]. Pontecorvo suggested that neutrinos, like kaons, could change identity as they propagate, provided that the states produced in weak interactions were not identical to the states of definite mass.

Neutrino oscillations arise from the misalignment between flavor eigenstates and mass eigenstates. In a weak interaction, a neutrino is produced in a definite flavor state, associated with a charged lepton of the same flavor. However, the flavor eigenstates $|\nu_\alpha\rangle$, with $\alpha = e, \mu, \tau$, are quantum superpositions of mass eigenstates $|\nu_k\rangle$, where $k = 1, 2, 3$:

$$|\nu_\alpha\rangle = \sum_k U^*_{\alpha k} \, |\nu_k\rangle \, . \tag{2.7}$$

This relationship may also be written in matrix form as:

$$\begin{pmatrix} \nu_e \\ \nu_\mu \\ \nu_\tau \end{pmatrix} = \begin{pmatrix} U_{e1} & U_{e2} & U_{e3} \\ U_{\mu 1} & U_{\mu 2} & U_{\mu 3} \\ U_{\tau 1} & U_{\tau 2} & U_{\tau 3} \end{pmatrix} \begin{pmatrix} \nu_1 \\ \nu_2 \\ \nu_3 \end{pmatrix}, \tag{2.8}$$

where the coefficients $U_{\alpha k}$ are elements of the Pontecorvo-Maki-Nakagawa-Sakata (PMNS) matrix.

The PMNS matrix is parameterized by three mixing angles, θ_{12}, θ_{23}, and θ_{13}, a Dirac charge parity violating phase δ_{CP}, and two additional phases ξ_1 and ξ_2 that appear if neutrinos are Majorana particles. A commonly used parameterization of the PMNS matrix is:

$$\begin{aligned} U = & \begin{pmatrix} 1 & 0 & 0 \\ 0 & \cos\theta_{23} & \sin\theta_{23} \\ 0 & -\sin\theta_{23} & \cos\theta_{23} \end{pmatrix} \begin{pmatrix} \cos\theta_{13} & 0 & \sin\theta_{13}e^{-i\delta_{CP}} \\ 0 & 1 & 0 \\ -\sin\theta_{13}e^{i\delta_{CP}} & 0 & \cos\theta_{13} \end{pmatrix} \\ & \times \begin{pmatrix} \cos\theta_{12} & \sin\theta_{12} & 0 \\ -\sin\theta_{12} & \cos\theta_{12} & 0 \\ 0 & 0 & 1 \end{pmatrix} \begin{pmatrix} 1 & 0 & 0 \\ 0 & e^{i\xi_1} & 0 \\ 0 & 0 & e^{i\xi_2} \end{pmatrix}. \end{aligned} \tag{2.9}$$

The final diagonal matrix containing the Majorana phases does not affect neutrino oscillation probabilities, as these phases cancel when forming the inner products relevant for flavor transitions. Nevertheless, they play a crucial role in lepton number violating processes such as $0\nu\beta\beta$ decay and therefore remain of central interest in neutrino physics.

To illustrate how neutrino oscillation parameters are extracted experimentally, it

is instructive to derive the oscillation probability in vacuum. Unlike quarks, which are confined within hadrons, neutrinos propagate freely over macroscopic distances. The massive neutrino states $|\nu_k\rangle$ can therefore be treated as plane wave solutions to the Schrödinger equation, evolving in time as:

$$|\nu_k(t)\rangle = e^{-iE_k t}\,|\nu_k\rangle\,, \qquad E_k = \sqrt{m_k^2 + \vec{p}^2}. \tag{2.10}$$

A neutrino produced at time $t = 0$ in a flavor state $|\nu_\alpha\rangle$ evolves as a coherent superposition of mass eigenstates,

$$|\nu_\alpha(t)\rangle = \sum_k U^*_{\alpha k} e^{-iE_k t}\,|\nu_k\rangle\,. \tag{2.11}$$

Using the unitarity of the PMNS matrix, $U^\dagger U = \mathbb{1}$, this expression may be rewritten in the flavor basis as:

$$|\nu_\alpha(t)\rangle = \sum_{\beta=e,\mu,\tau} \left(\sum_k U^*_{\alpha k} e^{-iE_k t} U_{\beta k} \right) |\nu_\beta\rangle\,. \tag{2.12}$$

The probability that a neutrino produced in flavor state ν_α is later detected as flavor ν_β is then given by:

$$P(\nu_\alpha \to \nu_\beta) = |\,\langle \nu_\beta | \nu_\alpha(t)\rangle\,|^2 = \sum_{k,j} U^*_{\alpha k} U_{\beta k} U_{\alpha j} U^*_{\beta j} e^{-i(E_k - E_j)t}. \tag{2.13}$$

For ultra relativistic neutrinos, where $m_k \ll |\vec{p}|$, the energy may be expanded as:

$$E_k \simeq E + \frac{m_k^2}{2E}, \tag{2.14}$$

leading to

$$E_k - E_j = \frac{\Delta m^2_{kj}}{2E}, \qquad \Delta m^2_{kj} \equiv m_k^2 - m_j^2. \tag{2.15}$$

Since oscillation experiments measure the source detector separation L rather than the

propagation time, the approximation $t \simeq L$ may be used. The oscillation probability then becomes:

$$P(\nu_\alpha \to \nu_\beta) = \sum_{k,j} U^*_{\alpha k} U_{\beta k} U_{\alpha j} U^*_{\beta j} e^{-i\Delta m^2_{kj} L/2E}. \tag{2.16}$$

Separating the real and imaginary components yields the familiar form:

$$P(\nu_\alpha \to \nu_\beta) = \delta_{\alpha\beta} - 4\sum_{k>j} \mathfrak{Re}\left[U^*_{\alpha k} U_{\beta k} U_{\alpha j} U^*_{\beta j}\right] \sin^2\left(\frac{\Delta m^2_{kj} L}{4E}\right) + 2\sum_{k>j} \mathfrak{Im}\left[U^*_{\alpha k} U_{\beta k} U_{\alpha j} U^*_{\beta j}\right] \sin\left(\frac{\Delta m^2_{kj} L}{2E}\right). \tag{2.17}$$

The oscillation amplitudes are governed by the elements of the PMNS matrix, while the oscillation frequency is set by the ratio $\Delta m^2_{kj} L/E$. In practical units, this phase may be written as:

$$\frac{\Delta m^2_{kj} L}{2E} \approx 1.27 \frac{\Delta m^2_{kj}\,[\mathrm{eV}^2]\, L\,[\mathrm{km}]}{E\,[\mathrm{GeV}]}. \tag{2.18}$$

Within the past two decades, the majority of neutrino oscillation parameters have been measured with impressive precision. The three mixing angles θ_{12}, θ_{23}, and θ_{13}, along with the two independent squared mass splittings Δm^2_{21} and $|\Delta m^2_{31}|$, are now known to the level of a few percent or better. These measurements have been achieved using a diverse set of experiments that study neutrinos originating from the Sun, the Earth's atmosphere, nuclear reactors, and particle accelerators.

Despite this progress, two fundamental questions remain unresolved within the oscillation framework. The first concerns the value of the charge parity violating phase δ_{CP}, which governs potential differences between neutrino and antineutrino oscillation probabilities. The second is the ordering of the neutrino mass eigenstates, commonly referred to as the neutrino mass hierarchy.

Because oscillation experiments are sensitive only to differences in squared masses, they cannot determine the absolute neutrino mass scale. As a result, two distinct mass

orderings remain consistent with current data. In the normal ordering scenario, the third mass eigenstate is the heaviest, with $m_3 > m_2 > m_1$. In the inverted ordering scenario, the third mass eigenstate is the lightest, with $m_2 > m_1 > m_3$. These two possibilities correspond to opposite signs of the atmospheric mass splitting, Δm^2_{31} or Δm^2_{32}, which current experiments have not yet been able to determine conclusively.

Table 2.2 summarizes the current best fit values and one standard deviation uncertainties for the neutrino oscillation parameters, reproduced from the NuFIT version 6.0 global analysis [28]. This fit incorporates data from a wide range of experiments, including atmospheric neutrino measurements from Super-Kamiokande, and provides results for both normal and inverted mass orderings. The solar mass splitting Δm^2_{21} is common to both orderings, while the atmospheric mass splitting Δm^2_{3k} differs in sign depending on the assumed hierarchy. In Table 2.2, the notation Δm^2_{sol} refers to Δm^2_{21}, while Δm^2_{atm} denotes either Δm^2_{31} or Δm^2_{32}, depending on the ordering. This convention reflects the historical sensitivity of solar neutrino experiments to Δm^2_{21} and of atmospheric neutrino experiments to $|\Delta m^2_{31}| \approx |\Delta m^2_{32}|$.

Future experiments are expected to resolve the remaining ambiguities in the oscillation framework. Medium baseline reactor experiments such as JUNO [29] aim to determine the mass ordering through precision measurements of oscillation interference effects. Long baseline accelerator experiments, including Hyper-Kamiokande [30] and DUNE [31], are designed to probe both the mass ordering and the value of δ_{CP} through detailed studies of neutrino and antineutrino appearance channels.

Equation 2.17 shows that neutrino oscillation experiments are sensitive only to differences in the squared neutrino masses, Δm^2_{jk}, and provide no information on the absolute values of the individual mass eigenstates. As a result, determining the absolute neutrino mass scale requires experimental approaches that are complementary to oscillation measurements.

Oscillation parameter	Normal	Inverted
$\Delta m^2_{21}[10^{-5}\,\mathrm{eV}^2]$	$7.49^{+0.19}_{-0.19}$	$7.49^{+0.19}_{-0.19}$
$\Delta m^2_{3k}[10^{-3}\,\mathrm{eV}^2]$	$+2.513^{+0.021}_{-0.019}$	$-2.484^{+0.020}_{-0.020}$
$\sin^2\theta_{12}$	$0.308^{+0.012}_{-0.011}$	$0.308^{+0.012}_{-0.011}$
$\sin^2\theta_{23}$	$0.470^{+0.17}_{-0.13}$	$0.550^{+0.012}_{-0.015}$
$\sin^2\theta_{13}$	$0.02215^{+0.00056}_{-0.00058}$	$0.02231^{+0.00056}_{-0.00056}$
$\delta_{CP}[^\circ]$	212^{+26}_{-41}	274^{+22}_{-25}

Table 2.2: Best-fit values $\pm 1\sigma$ from a global analysis of neutrino oscillation parameters reproduced from NuFIT version 6.0 in Reference [28]. Note that $\Delta m^2_{3k} \equiv \Delta m^2_{31} > 0$ for normal ordering and $\Delta m^2_{3k} \equiv \Delta m^2_{32} < 0$ for inverted ordering.

One such approach is pursued by the KATRIN experiment, which directly probes the kinematics of β decay. KATRIN measures the energy spectrum of electrons emitted in the decay of tritium, which has a Q-value of 18.6 keV. If neutrinos are massive, a small but measurable fraction of the available decay energy is carried away by the neutrino. Precise measurements of the endpoint of the electron energy spectrum therefore place a constraint on the effective mass of the electron flavor neutrino, which is a superposition of the neutrino mass eigenstates,

$$m_{\nu_e} = \sqrt{\sum_i |U_{ei}|^2 m_i^2}. \tag{2.19}$$

Achieving sensitivity to this quantity is experimentally challenging and requires sub electron volt energy resolution near the endpoint of the beta decay spectrum. The most stringent direct limit to date has been set by the KATRIN experiment, which reports $m_{\nu_e} < 0.8\,\mathrm{eV}$ at 90% confidence level [32]. Future experiments, such as

Project 8, aim to further improve this sensitivity using Cyclotron Radiation Emission Spectroscopy, a technique that measures the frequency of radiation emitted by beta decay electrons spiraling in a magnetic field [33].

An alternative, indirect probe of neutrino masses is provided by cosmological observations. Neutrinos influence the formation and evolution of large scale structure in the universe due to their relativistic nature in the early universe and their contribution to the total matter density at later times. Measurements of the Cosmic Microwave Background, Baryon Acoustic Oscillations, and Redshift Space Distortions can therefore be combined to constrain the sum of the neutrino mass eigenstates, $\sum m_i = m_1 + m_2 + m_3$. Currently, the strongest cosmological constraint yields an upper limit of $\sum m_i < 0.09\,\text{eV}$ at 95% confidence level [34].

A third and potentially most sensitive approach to determining the absolute neutrino mass scale involves $0\nu\beta\beta$ decay. Observation of this decay would not only provide access to an effective neutrino mass parameter, but would also demonstrate the violation of lepton number and establish the Majorana nature of neutrinos. Before discussing aspects of $2\nu\beta\beta$ and $0\nu\beta\beta$ decay, we will first review the theoretical framework of neutrino mass generation that motivates and underpins these searches.

2.3 Neutrino Mass

The observation of neutrino oscillations establishes that neutrinos possess nonzero masses and that flavor eigenstates are superpositions of mass eigenstates. Despite this, the underlying mechanism responsible for neutrino mass generation remains unknown. Numerous extensions of the Standard Model have been proposed to explain this phenomenon, as discussed below.

Here we follow the derivation presented in Ref. [35]. Landau, Lee and Yang, and independently Salam, showed that a massless fermion can be consistently described

by a chiral field within a two-component theory of massless neutrinos. We begin with the Dirac equation:

$$(i\gamma^\mu \partial_\mu - m)\psi = 0, \tag{2.20}$$

for a fermion field ψ. Decomposing the Dirac spinor into its left- and right-handed chiral components:

$$\psi = \psi_L + \psi_R, \tag{2.21}$$

where $\psi_{L,R} = P_{L,R}\psi$ and $P_{L,R} = \frac{1}{2}(1 \mp \gamma^5)$ are the chiral projection operators, the Dirac equation can be written as the coupled system:

$$i\gamma^\mu \partial_\mu \psi_L = m\psi_R, \tag{2.22}$$

$$i\gamma^\mu \partial_\mu \psi_R = m\psi_L, \tag{2.23}$$

where the space-time evolution of the left- and right-handed fields is coupled through the mass term m.

In the massless limit, $m = 0$, Eqs. (2.22) and (2.23) decouple:

$$i\gamma^\mu \partial_\mu \psi_L = 0, \tag{2.24}$$

$$i\gamma^\mu \partial_\mu \psi_R = 0. \tag{2.25}$$

In this case, a massless fermion may be fully described by a single chiral field (either left-handed or right-handed) which contains only two independent degrees of freedom. These equations are known as the Weyl equations, and the corresponding spinors ψ_L and ψ_R are referred to as Weyl spinors.

The minimal formulation of the Standard Model adopts this two-component description for neutrinos, treating them as massless fermions. In this framework, the neutrino is described entirely by a left-handed Weyl spinor, ν_L, which participates in the weak interaction, while no right-handed neutrino field, ν_R, is included.

2.3.1 Dirac Masses

If right-handed neutrino fields ν_R exist, neutrinos may acquire mass through a Dirac mass term analogous to those of the charged leptons. In this case, a Yukawa interaction can be written as:

$$-\mathcal{L}_{\text{Dirac}} = Y^{\nu}_{ij}\, \overline{L}_{Li}\, \tilde{\Phi}\, \nu_{Rj} + \text{h.c.}, \tag{2.26}$$

where L_{Li} is the left-handed lepton doublet of generation i, $\tilde{\Phi} = i\sigma_2 \Phi^*$ is the conjugate Higgs doublet, and Y^{ν}_{ij} are the neutrino Yukawa couplings. After electroweak symmetry breaking, when the Higgs field acquires a vacuum expectation value v, this interaction generates Dirac neutrino masses:

$$m^{\nu}_{ij} = \frac{v}{\sqrt{2}}\, Y^{\nu}_{ij}. \tag{2.27}$$

This mechanism is entirely analogous to mass generation for the charged leptons and quarks in the Standard Model, where fermion masses arise through Yukawa couplings to the Higgs field following spontaneous symmetry breaking of the $SU(2)_L \times U(1)_Y$ gauge symmetry. In the unitary gauge, the Higgs doublet may be written as:

$$\Phi = \frac{1}{\sqrt{2}} \begin{pmatrix} 0 \\ v + h \end{pmatrix}, \tag{2.28}$$

where h denotes the physical Higgs boson. Coupling this field (or its conjugate) to left- and right-handed fermion fields yields Dirac mass terms proportional to the Higgs vacuum expectation value, as well as Higgs–fermion interaction terms.

Applying this same mechanism to neutrinos, however, presents two conceptual difficulties. First, right-handed neutrino fields are absent from the minimal Standard Model and must be introduced as gauge-singlet states. Such fields do not participate in the weak interaction and are therefore often referred to as *sterile* neutrinos. The inclusion of ν_R thus constitutes a minimal extension of the Standard Model.

Second, even if right-handed neutrinos exist and neutrinos are purely Dirac fermions, the observed smallness of neutrino masses poses a naturalness problem. Current experimental constraints require neutrino masses to be below the eV scale, implying Yukawa couplings:

$$Y_{ij}^{\nu} \lesssim 10^{-12}, \tag{2.29}$$

which are many orders of magnitude smaller than those of the charged fermions. This extreme hierarchy is difficult to justify within the Standard Model framework and stands in sharp contrast to the mass spectrum of the other fermions.

The striking disparity between neutrino masses and those of the charged leptons and quarks strongly suggests the presence of an underlying mechanism that suppresses neutrino masses relative to the electroweak scale. This observation has motivated a wide class of neutrino mass models that extend the Standard Model and generate light neutrino masses in a more natural way. Several such mechanisms are discussed in the following sections.

2.3.2 Majorana Neutrino Mass

Since neutrinos have been experimentally shown to possess nonzero masses, the two-component theory of massless neutrinos is no longer sufficient. In 1937, Majorana proposed an alternative formulation of the Dirac equation in which a massive fermion can be described by a single spinor field rather than independent left- and right-handed components. The key assumption of the Majorana construction is that the right-handed field is not independent, but instead related to the left-handed field by charge conjugation:

$$\psi_R = C\,\overline{\psi_L}^{T}, \tag{2.30}$$

where C is the charge conjugation matrix.

Using the properties of the charge conjugation operator and the chiral projection

operators, one finds that:

$$P_L\big(C\,\overline{\psi_L}^{\,T}\big) = 0, \tag{2.31}$$

which demonstrates that the charge-conjugated left-handed field transforms as a right-handed field. In other words, charge conjugation converts a left-handed Weyl spinor into a right-handed one.

With this identification, the fermion field may be written entirely in terms of a single chiral component:

$$\psi = \psi_L + \psi_L^C, \tag{2.32}$$

where $\psi_L^C \equiv C\overline{\psi_L}^{\,T}$. The corresponding equation of motion takes the form:

$$i\gamma^\mu \partial_\mu \psi = m\psi^C, \tag{2.33}$$

where ψ^C denotes the charge-conjugated field. This leads directly to the Majorana condition:

$$\psi = \psi^C, \tag{2.34}$$

which implies that the fermion is identical to its antiparticle.

Equation (2.34) can only be satisfied by electrically neutral fermions. Among the known elementary fermions, only neutrinos meet this criterion, making them unique candidates for Majorana particles. Since neutrinos interact solely through the weak interaction, the overall charge parity of the neutrino field has no observable consequence and may be chosen arbitrarily.

If neutrinos are Majorana particles, neutrinos and antineutrinos are not distinct states but differ only by their helicities. By convention, negative-helicity states are referred to as neutrinos, while positive-helicity states are referred to as antineutrinos.

In the Standard Model framework, the simplest Majorana mass term that can be constructed using only Standard Model fields and respecting gauge symmetries is a

lepton-number-violating dimension-five operator:

$$\mathcal{L}_5 = \frac{Z^{\nu}_{ij}}{\Lambda}\big(\overline{L^i_L}\,\tilde{\Phi}\big)\big(\tilde{\Phi}^T L^j_L\big) + \text{h.c.}, \tag{2.35}$$

where Z^{ν}_{ij} is a dimensionless 3×3 coupling matrix, $\tilde{\Phi} = i\sigma_2\Phi^*$ is the conjugate Higgs doublet, and Λ denotes the scale of new physics beyond the Standard Model.

After electroweak symmetry breaking, this effective interaction generates a Majorana mass term for the light neutrinos:

$$\mathcal{L}_{M_\nu} = \frac{1}{2}\,\frac{v^2}{\Lambda} Z^{\nu}_{ij}\,\overline{\nu_{L_i}}\,\nu^C_{L_j} + \text{h.c.}, \tag{2.36}$$

corresponding to the Majorana neutrino mass matrix:

$$\mathcal{M}_\nu = Z^{\nu}_{ij}\,\frac{v^2}{\Lambda}. \tag{2.37}$$

Compared to the renormalizable Dirac mass terms of the charged fermions, this effective operator contains two Higgs fields and is therefore of mass dimension five. As a result, it is non-renormalizable and must be interpreted as a low-energy manifestation of new physics at the scale Λ. Notably, this operator is the only dimension-five operator that can be constructed within the Standard Model field content and gauge symmetries to generate neutrino masses.

The suppression factor v^2/Λ naturally explains the smallness of neutrino masses if Λ lies far above the electroweak scale. This structure mirrors the mass suppression obtained in seesaw mechanisms, which provide explicit ultraviolet completions of the effective operator in Eq. (2.35). These mechanisms are discussed in the following section.

2.3.3 Seesaw Mechanism

We now discuss an extension of the Standard Model that naturally generates light active neutrino masses through the introduction of one or more heavy sterile neutrinos. Adding m sterile neutrino fields, ν_{si} $(i = 1, \ldots, m)$, allows for two distinct types of neutrino mass terms. The most general neutrino mass Lagrangian can be written as:

$$-\mathcal{L}_{M_\nu} = M_{D_{ij}}\, \overline{\nu}_{si} \nu_{Lj} + \frac{1}{2} M_{N_{ij}}\, \overline{\nu}_{si} \nu^c_{sj} + \text{h.c.}, \tag{2.38}$$

where M_D is a complex $m \times 3$ Dirac mass matrix and M_N is a complex symmetric $m \times m$ Majorana mass matrix.

The first term in Eq. (2.38) corresponds to a Dirac mass term, generated after electroweak symmetry breaking through Yukawa couplings between the sterile neutrinos, the left-handed lepton doublets, and the Higgs field:

$$Y^\nu_{ij}\, \overline{\nu}_{si}\, \tilde{\Phi}^\dagger L_{Lj} \quad \Rightarrow \quad M_{D_{ij}} = Y^\nu_{ij}\, \frac{v}{\sqrt{2}}. \tag{2.39}$$

The second term is a Majorana mass term for the sterile neutrinos and violates lepton number by two units.

Equation (2.38) may be rewritten in matrix form as:

$$-\mathcal{L}_{M_\nu} = \frac{1}{2} \begin{pmatrix} \overline{\nu_L} & \overline{\nu_s} \end{pmatrix} \begin{pmatrix} 0 & M_D^T \\ M_D & M_N \end{pmatrix} \begin{pmatrix} \nu_L^c \\ \nu_s^c \end{pmatrix} + \text{h.c.}, \tag{2.40}$$

where $\vec{\nu} = (\vec{\nu}_L, \vec{\nu}_s^{\,c})^T$ is a $(3+m)$-dimensional vector. The full neutrino mass matrix M_ν is complex and symmetric, and may be diagonalized by a unitary transformation:

$$(V^\nu)^T M_\nu V^\nu = \text{diag}(m_1, m_2, \ldots, m_{3+m}), \tag{2.41}$$

with the corresponding mass eigenstates given by:

$$\vec{\nu}_{\rm mass} = (V^{\nu})^{\dagger}\vec{\nu}. \tag{2.42}$$

In terms of the mass eigenstates, the neutrino mass Lagrangian becomes:

$$-\mathcal{L}_{M_\nu} = \frac{1}{2}\sum_{k=1}^{3+m} m_k \left(\overline{\nu}^c_{{\rm mass},k}\nu_{{\rm mass},k} + \overline{\nu}_{{\rm mass},k}\nu^c_{{\rm mass},k}\right) \tag{2.43}$$

$$= \frac{1}{2}\sum_{k=1}^{3+m} m_k\, \overline{\nu}_{M_k}\nu_{M_k}, \tag{2.44}$$

where $\nu_{M_k} = \nu_{{\rm mass},k} + \nu^c_{{\rm mass},k}$ satisfies the Majorana condition $\nu_{M_k} = \nu^c_{M_k}$.

In this mass basis, the original weak-interaction neutrino fields are related to the Majorana mass eigenstates by:

$$\nu_{Li} = P_L \sum_{j=1}^{3+m} V^{\nu}_{ij}\,\nu_{M_j}, \qquad i = 1,2,3. \tag{2.45}$$

In the phenomenologically relevant limit where the eigenvalues of M_N are much larger than the electroweak scale, $M_N \gg v$, the diagonalization of M_ν yields three light neutrino states ν_l and m heavy neutrino states N:

$$-\mathcal{L}_{M_\nu} = \frac{1}{2}\,\overline{\nu}_l M^l \nu_l + \frac{1}{2}\,\overline{N} M^h N, \tag{2.46}$$

with approximate mass matrices:

$$M^l \simeq -V_l^T\, M_D^T\, M_N^{-1}\, M_D\, V_l, \tag{2.47}$$

$$M^h \simeq V_h^T\, M_N\, V_h, \tag{2.48}$$

and mixing matrix:

$$V^{\nu} \simeq \begin{pmatrix} \left(1 - \frac{1}{2} M_D^{\dagger} M_N^{*-1} M_N^{-1} M_D\right) V_l & M_D^{\dagger} M_N^{*-1} V_h \\ -M_N^{-1} M_D V_l & \left(1 - \frac{1}{2} M_N^{-1} M_D M_D^{\dagger} M_N^{*-1}\right) V_h \end{pmatrix}. \tag{2.49}$$

Here, V_l and V_h are 3×3 and $m \times m$ unitary matrices that describe mixing among the light and heavy neutrino sectors, respectively. The matrix V_l may be identified with the Pontecorvo–Maki–Nakagawa–Sakata (PMNS) matrix, which is discussed in detail in a later section.

The structure of the mass eigenvalues illustrates the origin of the term *seesaw*: the heavy neutrino masses scale with M_N, while the light neutrino masses are suppressed by M_N^{-1}. This mechanism is known as the Type-I seesaw, characterized by the introduction of heavy sterile neutrinos. It naturally produces light, predominantly left-handed neutrinos and heavy, predominantly right-handed neutrinos.

The Type-I seesaw mechanism therefore provides a compelling extension of the Standard Model that explains the smallness of neutrino masses without invoking extremely small Yukawa couplings. In addition, the heavy sterile neutrinos introduced in this framework may have important implications for physics beyond the Standard Model, including potential connections to dark matter.

2.3.4 Lepton Number Violation and Leptogenesis

A key consequence of Majorana neutrinos is the violation of lepton number. In the Standard Model, lepton number is an accidental global symmetry. This means that it's not imposed by construction, but instead emerges because no renormalizable operators that violate lepton number are allowed by the gauge symmetries and field content. Many extensions of the Standard Model, however, naturally incorporate lepton number violation.

Lepton number violation also plays a central role in leptogenesis, a proposed

explanation for one of the most fundamental questions in particle physics: why the observable Universe contains more matter than antimatter. A comprehensive review of the phenomenology of matter–antimatter asymmetry is beyond the scope of this chapter. Instead, a brief summary of the key observational and theoretical ingredients relevant to leptogenesis is presented here.

The baryon asymmetry of the Universe is inferred from two independent classes of observations. The first arises from measurements of the primordial abundances of light elements, such as D, ^{3}He, ^{4}He, and ^{7}Li, produced during Big Bang nucleosynthesis (BBN). These abundances depend on the baryon-to-photon asymmetry parameter η, which is measured to be [36]:

$$\eta^{\rm BBN} \equiv \left.\frac{n_B - n_{\bar{B}}}{n_\gamma}\right|_0 = (4.7\text{–}6.5) \times 10^{-10} \tag{2.50}$$

The second constraint comes from observations of anisotropies in the cosmic microwave background (CMB) [37]. A key CMB observable is the speed of sound c_s in the photon–baryon fluid. Measurements of temperature fluctuations in the CMB determine the baryon energy density ρ_B, commonly expressed in terms of the baryon density parameter:

$$\Omega_B = \frac{\rho_B}{\rho_{\rm crit}} \tag{2.51}$$

The corresponding baryon asymmetry inferred from CMB observations is:

$$\eta^{\rm CMB} = 2.74 \times 10^{-8}\, \Omega_B h^2 = 6.1^{+0.3}_{-0.2} \times 10^{-10} \tag{2.52}$$

where $h = H_0/(100\,{\rm km\,s^{-1}\,Mpc^{-1}}) = 0.682 \pm 0.0028$ is the dimensionless Hubble parameter [38]. The remarkable agreement between the BBN and CMB determinations of the baryon asymmetry represents a major success of hot Big Bang cosmology.

Any dynamical mechanism responsible for generating the observed baryon asymmetry must satisfy three necessary conditions, first identified by Sakharov and now

known as the Sakharov conditions:

1. Baryon number violation
2. C and CP violation
3. Departure from thermal equilibrium

Although the Standard Model contains all three ingredients in principle, it fails to produce a baryon asymmetry of sufficient magnitude.

Leptogenesis provides a compelling beyond-the-Standard-Model framework in which these conditions can be satisfied. In this scenario, the heavy sterile neutrinos introduced in the Type-I seesaw mechanism undergo CP-violating, out-of-equilibrium decays that generate a net lepton asymmetry. Electroweak sphaleron processes subsequently convert a fraction of this lepton asymmetry into a baryon asymmetry, linking the origin of neutrino mass to the matter–antimatter asymmetry of the Universe.

2.4 Double Beta Decay

As discussed in the previous sections, the observation of neutrino oscillations establishes that neutrinos are massive and motivates extensions of the Standard Model that may violate lepton number. Double beta decay arises naturally in this context, providing an experimental probe that is simultaneously sensitive to neutrino properties and to the nuclear many-body dynamics governing rare weak processes. In particular, $0\nu\beta\beta$ offers a direct test of lepton number violation and the Majorana nature of neutrinos. However, the interpretation of $0\nu\beta\beta$ searches is fundamentally limited by uncertainties in the associated nuclear matrix elements (NMEs).

The $2\nu\beta\beta$ decay process, which is allowed within the Standard Model and has been experimentally observed in multiple nuclei, plays a critical complementary role. Measurements of this process provide an essential experimental benchmark for nuclear

structure calculations. Of particular interest are two-neutrino double beta decay transitions to excited states of the daughter nucleus, which offer an underexplored but highly informative probe of nuclear dynamics. Measurements or limits on these transitions directly test the same nuclear operators that appear in $0\nu\beta\beta$ decay and are therefore especially relevant for reducing theoretical uncertainties in $0\nu\beta\beta$ decay searches. In the following sections, the theoretical framework of double beta decay is reviewed, with emphasis on two-neutrino double beta decay to excited states and their connection to nuclear matrix elements relevant for $0\nu\beta\beta$.

2.5 Two-Neutrino Double Beta Decay

Most unstable nuclei decay through first-order weak processes such as single β^- decay or electron capture, converting a neutron into a proton or vice versa while conserving lepton number. In some even–even nuclei, however, single beta decay is energetically forbidden or strongly suppressed, while a second-order weak process involving the simultaneous conversion of two neutrons into two protons becomes allowed. This $2\nu\beta\beta$ process was first proposed by Goeppert-Mayer in 1935 and is permitted within the Standard Model [39].

The canonical $2\nu\beta\beta$ process proceeds as

$$(A, Z) \rightarrow (A, Z + 2) + 2e^- + 2\bar{\nu}_e, \tag{2.53}$$

conserving total lepton number. The decay changes the nuclear charge by two units while leaving the mass number unchanged and occurs only if the resulting daughter nucleus is more tightly bound than the parent. The available energy, or Q value, is given by

$$Q_{\beta\beta} = m_N({}^A_Z X) - m_{N-2}({}^A_{Z+2} X') - 2m_e \tag{2.54}$$

which sets the scale for the phase space available to the emitted leptons. Here, m_e is the electron mass in the rest frame, $m_N\left({}^{A}_{Z}X\right)$ is the mass of the mother nucleus in the rest frame, and $m_{N-2}\left({}^{A}_{Z+2}X'\right)$ represents the mass of the daughter nucleus in the rest frame.

Not all nuclei are capable of undergoing double beta decay. Whether a given isotope can decay via the $2\nu\beta\beta$ process is determined by nuclear binding energies and the relative stability of neighboring isobars. Insight into this behavior can be obtained from the semi-empirical description of nuclear masses.

The mass of an atomic nucleus with mass number A and atomic number Z may be written as:

$$M = Zm_p + (A - Z)m_n - E(A, Z) \tag{2.55}$$

where m_p and m_n are the proton and neutron rest masses, respectively, and $E(A, Z)$ is the nuclear binding energy. The binding energy is well approximated by the semi-empirical mass formula:

$$E = a_v A - a_s A^{2/3} - a_C \frac{Z(Z-1)}{A^{1/3}} - a_A \frac{(N-Z)^2}{A} + \delta(N, Z) \tag{2.56}$$

which captures the dominant contributions to nuclear stability. The volume and surface terms describe the short-range attractive strong force, the Coulomb term accounts for proton–proton repulsion, and the asymmetry term reflects the energy cost of unequal numbers of protons and neutrons imposed by the Pauli exclusion principle.

The final contribution, $\delta(N, Z)$, represents the pairing energy and depends on

whether the nucleus contains even or odd numbers of protons and neutrons:

$$\delta(N,Z) = \begin{cases} -a_p A^{-1/2} & \text{even–even nuclei,} \\ 0 & \text{even–odd or odd–even nuclei,} \\ +a_p A^{-1/2} & \text{odd–odd nuclei} \end{cases} \tag{2.57}$$

This term favors nuclei with paired nucleons, making even–even nuclei systematically more tightly bound than their odd–odd neighbors.

As a result, nuclei with odd mass number A typically possess a single stable isobar and undergo ordinary beta decay if energetically allowed. In contrast, nuclei with even mass number exhibit two possible pairing configurations, leading to the familiar parabolic dependence of nuclear mass on Z for fixed A as shown in Figure 2·1. In some even–even nuclei, single β^- decay is energetically forbidden or strongly suppressed due to angular momentum and parity constraints, while the nucleus two units away in Z is more tightly bound. In such cases, the nucleus may decay directly to this lower-energy configuration through the simultaneous emission of two electrons and two antineutrinos.

This structure explains why $2\nu\beta\beta$ decay is observed only in a limited set of even–even nuclei and highlights the close connection between double beta decay and nuclear pairing effects. These same nuclear structure considerations also influence transitions to excited states of the daughter nucleus and play an important role in shaping the nuclear matrix elements relevant for both $2\nu\beta\beta$ and $0\nu\beta\beta$ decay.

The rate of $2\nu\beta\beta$ decay can be calculated using Fermi's golden rule, treating the process as a second-order weak interaction involving the emission of four leptons in the final state. The inverse half-life for $2\nu\beta\beta$ decay may be written in the standard

factorized form:

$$\Gamma^{2\nu} \equiv \left(T^{2\nu}_{1/2}\right)^{-1} = G^{2\nu}(Q_{\beta\beta}, Z) \left| \mathcal{M}^{2\nu}_{GT} + \frac{g_V^2}{g_A^2} \mathcal{M}^{2\nu}_{F} \right|^2 \tag{2.58}$$

where $G^{2\nu}(Q_{\beta\beta}, Z)$ is the phase-space factor, g_V and g_A are the vector and axial-vector weak coupling constants, and $\mathcal{M}^{2\nu}_F$ and $\mathcal{M}^{2\nu}_{GT}$ are the Fermi and Gamow–Teller nuclear matrix elements, respectively.

The phase-space factor $G^{2\nu}$ accounts for the integration over the energies and angles of the two emitted electrons and two antineutrinos and depends strongly on the available decay energy $Q_{\beta\beta}$ and the nuclear charge Z. These phase-space factors can be calculated with relatively high precision using relativistic electron wave functions and Coulomb corrections and are among the best-controlled theoretical inputs to the $2\nu\beta\beta$ decay rate [40, 41].

In contrast, the nuclear matrix elements encode the details of nuclear structure and many-body correlations. The Fermi matrix element $\mathcal{M}^{2\nu}_F$ corresponds to tran-

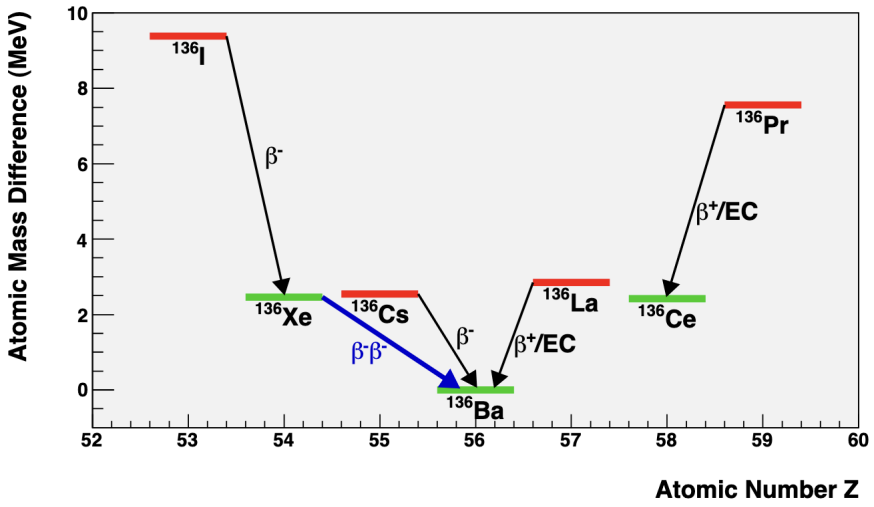

Figure 2·1: Atomic masses of $A = 136$ isotopes. Masses are given as differences with respect to the most bound isotope, ^{136}Ba. The red (green) levels indicate odd-odd (even-even) nuclei. Figure taken from [3].

sitions with no change in nuclear spin and arises from the vector component of the weak interaction, while the Gamow–Teller matrix element $\mathcal{M}_{GT}^{2\nu}$ corresponds to spin-changing transitions mediated by the axial-vector current. For two-neutrino double beta decay, Fermi transitions are strongly suppressed due to isospin conservation, as the dominant contribution proceeds through intermediate 1^+ states, corresponding to $0^+ \to 1^+ \to 0^+$ nuclear transitions. As a result, the decay rate is overwhelmingly dominated by the Gamow–Teller contribution.

Because $2\nu\beta\beta$ decay is a second-order weak process, its half-life is extremely long, with experimentally measured values typically in the range of 10^{19} to 10^{22} years [42]. While calculations of $G^{2\nu}$ are robust, theoretical predictions of $\mathcal{M}_{GT}^{2\nu}$ depend sensitively on the nuclear model employed and often fail to reproduce experimental half-lives without additional modifications. To account for this discrepancy, it is common to introduce an effective axial-vector coupling constant, g_A^{eff}, which is quenched relative to the free-nucleon value g_A. This is typically implemented through a rescaling of the Gamow–Teller matrix element,

$$\mathcal{M}_{GT}^{2\nu,\text{eff}} = \left(\frac{g_A^{\text{eff}}}{g_A}\right)^2 \mathcal{M}_{GT}^{2\nu}. \tag{2.59}$$

The magnitude and physical origin of this quenching remain subjects of active investigation and are thought to arise from a combination of missing many-body correlations, non-nucleonic degrees of freedom, and limitations of model spaces used in nuclear calculations [43]. Importantly, uncertainties associated with g_A^{eff} directly impact predictions for both $2\nu\beta\beta$ and $0\nu\beta\beta$ decay rates, further motivating experimental studies of $2\nu\beta\beta$ decay, including transitions to excited nuclear states.

2.6 Neutrinoless Double Beta Decay

Building on Goeppert-Mayer's work on $2\nu\beta\beta$ decay, Wendell Furry proposed the neutrinoless mode, now known as $0\nu\beta\beta$ decay [44]:

$$(A, Z) \rightarrow (A, Z + 2) + 2e^{-} \tag{2.60}$$

Unlike the two-neutrino mode, this process violates total lepton number by two units and is therefore forbidden within the Standard Model. Observation of $0\nu\beta\beta$ would constitute direct evidence of lepton number violation and establish that neutrinos are Majorana particles.

From an experimental standpoint, $0\nu\beta\beta$ and $2\nu\beta\beta$ share many similarities. Both are second-order weak processes and occur in the same set of even–even nuclei for which single beta decay is energetically forbidden. In both cases, nuclear recoil is negligible, and the decay energy is carried almost entirely by the emitted electrons. The key experimental distinction is that while $2\nu\beta\beta$ produces a continuous electron energy spectrum extending up to the endpoint energy $Q_{\beta\beta}$, $0\nu\beta\beta$ would manifest as a monoenergetic peak at the endpoint, smeared only by detector energy resolution.

Although phase-space considerations alone would favor the neutrinoless mode, the requirement of lepton number violation renders the decay rate extremely small, leading to half-lives exceeding 10^{26} years for experimentally accessible isotopes. As a result, $0\nu\beta\beta$ is among the rarest processes sought in modern experimental physics.

In general, several mechanisms beyond the Standard Model could mediate $0\nu\beta\beta$ decay, including heavy particle exchange or other lepton-number-violating interactions. However, a model-independent result known as the Schechter–Valle (or "Black Box") theorem demonstrates that the observation of $0\nu\beta\beta$, regardless of the underlying mechanism, necessarily implies that neutrinos possess a Majorana mass [45]. The theorem does not specify which mechanism dominates the decay rate, nor does

it require a direct connection to neutrino oscillation phenomenology. Specifically, it proposes the following:

- Should $0\nu\beta\beta$ be observed, its Feynman diagram must feature two electrons, two up-quark fields, and two down-quark fields. The process connecting these fields is arbitrary and is referred to as the "black box process". The theorem argues that this "black box process" effectively establishes the dimension-9 operator.
- The up and down quarks are contracted by the W boson.
- On the other end of the W boson propagators, electron fields are converted into neutrino fields.
- The entire diagram can be rotated to turn into a process that converts anti-neutrinos to neutrinos as shown in Figure 2·2.
- Finally, the possible cancelation of this process by other diagrams is dismissed by naturalness arguments.

The key conclusion of the black-box theorem is that should $0\nu\beta\beta$ be observed, even if the observed mechanism is not light Majorana neutrino exchange, the neutrino is a Majorana particle. It should be noted that since the theorem's original proposal,

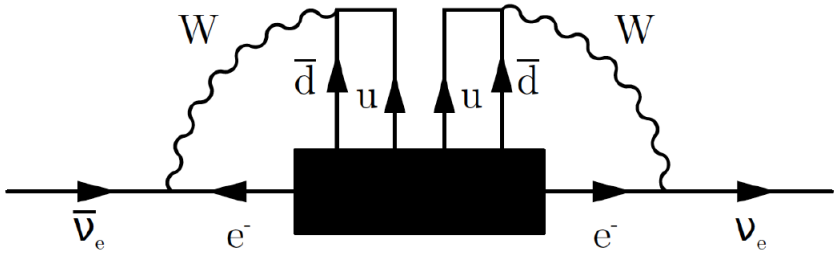

Figure 2·2: Depiction of the $0\nu\beta\beta$ black box theorem, the black box represents an arbitrary $0\nu\beta\beta$ process, which can be used to convert antineutrinos into neutrinos. Figure taken from Reference [4].

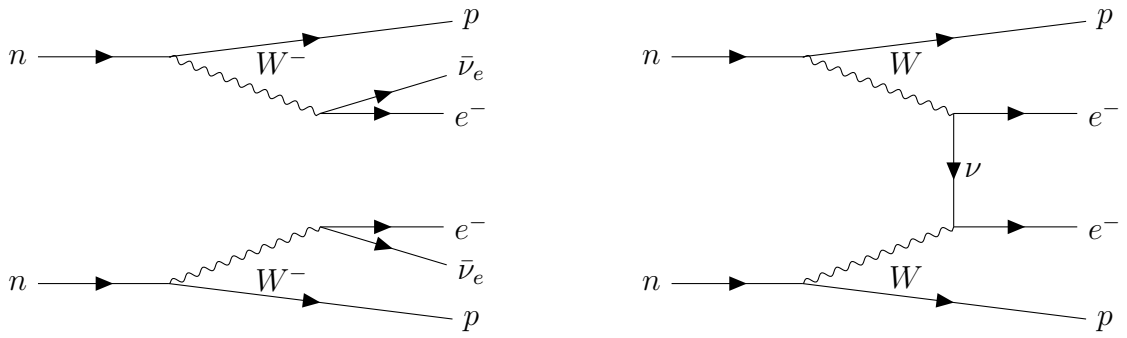

Figure 2·3: Feynman diagrams for $2\nu\beta\beta$ decay (left) and $0\nu\beta\beta$ decay (right).

counterexamples have been found allowing $0\nu\beta\beta$ without Majorana neutrinos [46], but the theorem still indicates potential links between $0\nu\beta\beta$, Majorana mass, and lepton number violation more broadly.

The most widely studied and experimentally motivated scenario is the light Majorana neutrino exchange mechanism. In this case, the decay proceeds through the exchange of a virtual neutrino between two Standard Model weak vertices as illustrated in comparison to $2\nu\beta\beta$ decay in Figure 2·3. The amplitude is nonzero only if neutrinos are massive and Majorana, as the process requires a helicity flip proportional to the neutrino mass. This mechanism provides a direct link between $0\nu\beta\beta$ decay and the absolute neutrino mass scale.

Under the assumption that light Majorana neutrino exchange dominates, the inverse half-life for $0\nu\beta\beta$ decay can be written in factorized form as:

$$\left(T_{1/2}^{0\nu}\right)^{-1} = G^{0\nu}(Q_{\beta\beta}, Z) \left|\mathcal{M}^{0\nu}\right|^2 \left(\frac{m_{\beta\beta}}{m_e}\right)^2 \tag{2.61}$$

where $G^{0\nu}$ is the phase-space factor, $\mathcal{M}^{0\nu}$ is the nuclear matrix element, m_e is the electron mass, and $m_{\beta\beta}$ is the effective Majorana neutrino mass:

$$m_{\beta\beta} = \left|m_1 U_{e1}^2 + m_2 U_{e2}^2 e^{2i\xi_1} + m_3 U_{e3}^2 e^{2i\xi_2}\right| \tag{2.62}$$

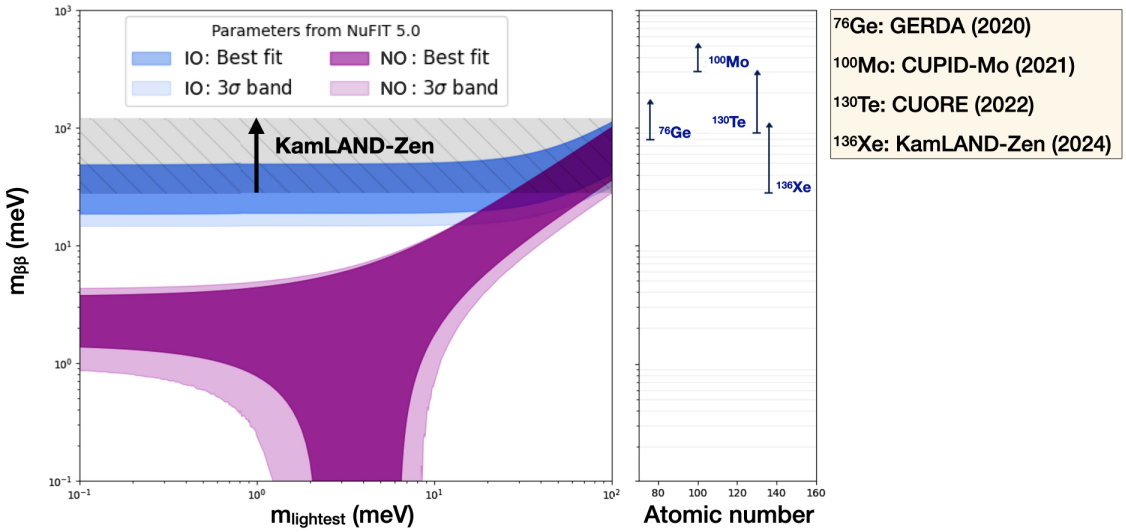

Figure 2·4: Possible Majorana masses for normal (magenta) and inverted (blue) mass orderings, calculated with mixing angles and mass differences from the PMNS matrix. The error bands come from uncertainties in the mixing parameters [28]. The KamLAND-Zen experimental limit on $m_{\beta\beta}$ is shown in gray. Recent limits [47, 48, 49] for other key isotopes are shown in the panel on the right. Figure taken from Reference [50].

Here, m_i are the light neutrino mass eigenvalues, U_{ei} are elements of the PMNS mixing matrix, and ξ_i are the Majorana CP-violating phases. Unlike neutrino oscillation experiments, which are insensitive to the absolute mass scale and Majorana phases, $0\nu\beta\beta$ decay probes both. The unknown values of the Majorana phases lead to allowed bands for $m_{\beta\beta}$ as a function of the lightest neutrino mass, with distinct regions corresponding to normal and inverted mass orderings. As a result, experimental limits on the $0\nu\beta\beta$ half-life translate into ranges of allowed $m_{\beta\beta}$ values rather than a single constraint which is illustrated in Figure 2·4.

While the phase-space factor $G^{0\nu}$ can be calculated with high precision, the NME $\mathcal{M}^{0\nu}$ remains the largest source of theoretical uncertainty in interpreting $0\nu\beta\beta$ searches. The calculation of $\mathcal{M}^{0\nu}$ requires detailed knowledge of nuclear wave func-

tions and many-body correlations and depends on the treatment of short-range physics, nuclear deformation, and the effective axial-vector coupling. For the standard light Majorana neutrino exchange mechanism, the NME can be written schematically as a sum of long- and short-range contributions:

$$\mathcal{M}^{0\nu}_{\text{light}} = g_A^4 \left(\mathcal{M}^{0\nu}_{\text{long}} + \mathcal{M}^{0\nu}_{\text{short}} \right) \tag{2.63}$$

The axial-vector coupling constant g_A governs the long-range weak interaction of nucleons and is factored out explicitly, serving as an important parameter in nuclear many-body calculations. The short-range contribution depends additionally on a two-nucleon coupling, g^{NN}, which is not written explicitly here. As in the case of $2\nu\beta\beta$ decay, the phase-space factors relevant for $0\nu\beta\beta$ are known with high precision for all experimentally relevant isotopes [40, 41]. In contrast, the NMEs themselves, along with some associated hadronic couplings, remain a dominant source of theoretical uncertainty despite significant recent progress.

The nuclear matrix elements (NMEs) encode the influence of nuclear structure on the rate of neutrinoless double beta decay and are obtained by combining nuclear wave functions for the initial and final states with the appropriate transition operators. In practice, NMEs are evaluated using nuclear many-body methods that attempt to capture correlations among nucleons across a wide range of length and energy scales. When limits on the $0\nu\beta\beta$ half-life are translated into constraints on the effective Majorana mass $m_{\beta\beta}$, the resulting uncertainty is presently dominated by the spread in available NME calculations rather than by experimental systematics. A detailed theoretical treatment of the construction of the transition operators, the treatment of short-range correlations, and the associated theoretical uncertainties lies beyond the scope of this thesis. Comprehensive reviews of modern NME calculations can be found in Reference [5].

In general, NME calculations proceed by first specifying an effective nuclear Hamiltonian that includes nucleon–nucleon interactions relevant to the decay process. A second step then introduces a framework for describing collective nuclear structure and many-body correlations beyond the mean-field level. The most widely used approaches are summarized below.

- The **Nuclear Shell Model (NSM)** has long served as a foundational tool for describing nuclear structure. In this framework, nucleons are treated as moving independently within a mean-field potential, augmented by a strong spin–orbit interaction. This potential, often modeled using harmonic oscillator or Woods–Saxon forms, represents the averaged interaction of a nucleon with the rest of the nucleus. The resulting single-particle states organize into energy shells, with particularly stable configurations occurring at so-called magic numbers. For practical calculations, the nucleus is typically separated into an inert core of filled shells and a smaller set of active valence nucleons. While the shell model provides a highly detailed description of nuclear correlations within the chosen model space, computational limitations restrict its applicability to relatively small valence spaces.

- The **Quasiparticle Random Phase Approximation (QRPA)** extends mean-field approaches by incorporating collective excitations and pairing correlations across a large set of nuclear orbitals. It is particularly well suited for medium and heavy nuclei, where shell-model calculations become computationally prohibitive. QRPA calculations rely on effective proton–neutron interactions, commonly parameterized by the coupling strength g_{pp}, which governs proton–neutron pairing. This parameter is often constrained by requiring agreement with experimentally measured $2\nu\beta\beta$ decay rates and subsequently applied to predictions of $0\nu\beta\beta$ decay. As a result, QRPA provides an explicit link be-

tween two-neutrino and neutrinoless decay calculations.

- **Energy Density Functional (EDF)** methods describe nuclei using energy functionals that depend on local densities and currents, extending the concept of mean-field theory in a self-consistent manner. These methods allow for the inclusion of important nuclear effects such as deformation, pairing, configuration mixing, and collective motion. EDF calculations have proven effective in describing medium and heavy nuclei, which are of primary interest for double beta decay searches. However, EDF-based NMEs are often among the largest reported values, in part because certain proton–neutron correlations are not treated explicitly.

- The **Interacting Boson Model (IBM)** provides a simplified, phenomenological description of nuclear structure by mapping pairs of valence nucleons onto bosonic degrees of freedom. In the context of double beta decay, the IBM has been extended to distinguish between proton and neutron bosons (IBM-2), enabling calculations of NMEs for even–even nuclei. While the model sacrifices microscopic detail, it offers a computationally efficient framework for exploring systematic trends across isotopic chains.

- ***Ab initio*** methods aim to describe nuclei starting from fundamental interactions derived from quantum chromodynamics via chiral effective field theory. These methods treat all nucleons explicitly and employ nuclear Hamiltonians with minimal phenomenological input. A key advantage of ab initio calculations is their systematic improvability and the ability to assess convergence. While these methods successfully reproduce properties of light and some medium-mass nuclei, extending them to the heavy nuclei relevant for $0\nu\beta\beta$ decay remains an active area of research [51].

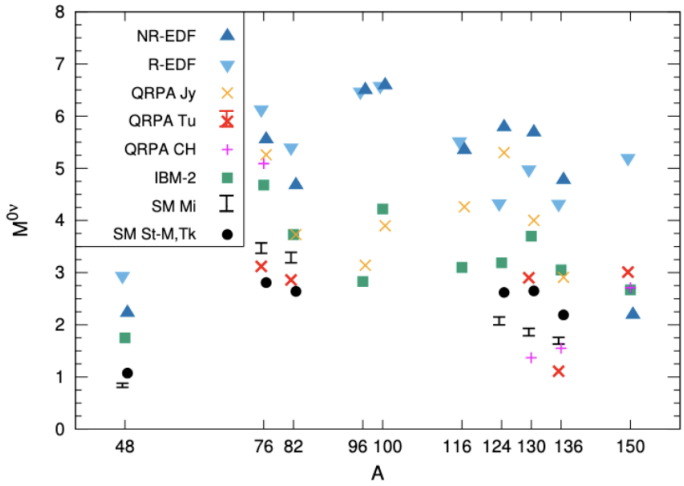

Figure 2·5: Results from various NME calculation of $M_{0\nu}$ on particular $0\nu\beta\beta$ decaying isotopes versus atomic mass. Figure taken from Reference [5].

To illustrate the level of agreement among different approaches, Figure 2·5 summarizes recent NME calculations for several candidate $0\nu\beta\beta$ isotopes. For a given nucleus, the predicted NMEs typically vary by factors of two to three across models. This spread constitutes one of the primary theoretical limitations in extracting neutrino mass information from $0\nu\beta\beta$ decay searches and provides strong motivation for experimental probes, such as two-neutrino double beta decay to excited states, that can help benchmark and constrain nuclear structure calculations.

Current nuclear structure methods yield values of $\mathcal{M}^{0\nu}$ that differ by factors of two to three for the same isotope. These discrepancies directly propagate into uncertainties on the extracted limits or measurements of $m_{\beta\beta}$. As a result, the physics reach of $0\nu\beta\beta$ experiments is no longer limited solely by exposure or background reduction, but increasingly by the reliability of nuclear matrix element calculations. Reducing these uncertainties has therefore become a central goal in the field.

2.7 Double Beta Decay to Excited States

An additional class of processes can provide valuable experimental input into NME calculations and aid in the interpretation of $0\nu\beta\beta$ decay searches: two-neutrino double beta decay to excited states of the daughter nucleus, denoted $2\nu\beta\beta^*$. In these Standard Model–allowed transitions, the parent nucleus undergoes double beta decay but populates an excited state of the daughter rather than its ground state. The subsequent de-excitation of the daughter nucleus produces a characteristic gamma-ray cascade.

Decays to excited states are suppressed by several orders of magnitude relative to ground-state transitions due to the reduced available phase space arising from the smaller effective Q value [52]. As a consequence, theoretical predictions for the corresponding half-lives span multiple orders of magnitude, reflecting the same nuclear-structure uncertainties that dominate predictions for $0\nu\beta\beta$ decay. Figure 2·6 illustrates representative predictions for $T^{2\nu^*}_{1/2}$ obtained using different nuclear models. An experimental observation of $2\nu\beta\beta^*$ in xenon would therefore provide a powerful constraint on nuclear matrix element calculations and help reduce theoretical uncertainties relevant to $0\nu\beta\beta$ searches.

The discussion below follows closely the formalism presented in Ref. [7], which explores the relationship between $2\nu\beta\beta$ and $0\nu\beta\beta$ NMEs within the NSM and the proton–neutron quasiparticle random-phase approximation (pnQRPA). The experimental signature of $2\nu\beta\beta^*$ consists of a standard $2\nu\beta\beta$ decay, followed (after a delay of order picoseconds) by the emission of one or more gamma rays as the daughter nucleus relaxes to its ground state. Experimentally, identifying this process requires either particle identification techniques capable of tagging the de-excitation gamma rays or the observation of distortions in the electron energy spectrum relative to the dominant ground-state $2\nu\beta\beta$ background. While challenging, these signatures provide

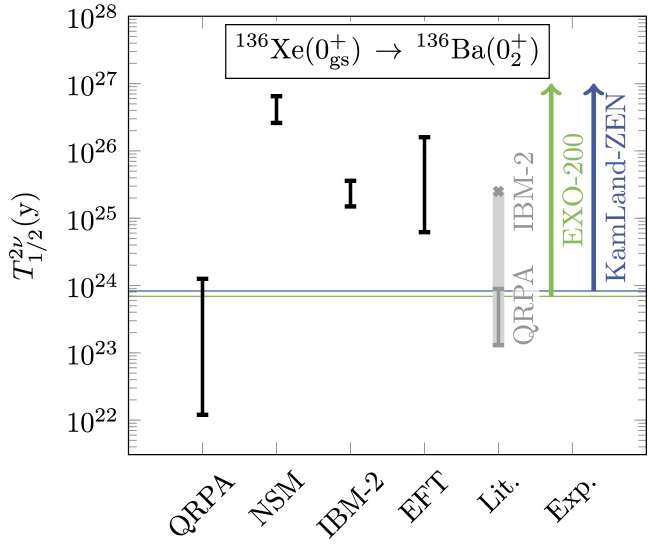

Figure 2·6: Predictions of $T^{2\nu^*}_{1/2}$ using various NME calculation methods. Figure taken from [6].

additional handles for background discrimination compared to ground-state decays.

As mentioned in Section 2.5 the half-life for $2\nu\beta\beta$ decay can be reasonably approximated with a single nuclear matrix element [7]:

$$\mathcal{M}^{2\nu} = -\sum_k \frac{\left(0^+_f \middle\| \sum_a \tau^-_a \sigma_a \middle\| 1^+_k\right)\left(1^+_k \middle\| \sum_b \tau^-_b \sigma_b \middle\| 0^+_i\right)}{\left[E_k - (E_i + E_f)/2\right]/m_e} \tag{2.64}$$

where the indices a and b run over all nucleons, τ^- is the isospin-lowering operator converting neutrons into protons, and σ is the spin operator. The sum extends over all intermediate 1^+ states of the odd–odd nucleus, with the energy denominator involving the excitation energy of each intermediate state relative to the average of the initial and final nuclear energies.

In contrast, the $0\nu\beta\beta$ nuclear matrix element (assuming the standard light Majorana neutrino exchange mechanism) is conventionally decomposed into three spin–isospin components:

$$\mathcal{M}^{0\nu}_L = \mathcal{M}^{0\nu}_{GT} - \mathcal{M}^{0\nu}_F + \mathcal{M}^{0\nu}_T\,, \tag{2.65}$$

corresponding to Gamow–Teller (GT), Fermi (F), and tensor (T) contributions.

These components are defined in terms of two-body operators:

$$\mathcal{M}_K^{0\nu} = \sum_{k,ab} \left\langle 0_f^+ \middle\| \mathcal{O}_{ab}^K \tau_a^- \tau_b^- H_K(r_{ab}) f_{\mathrm{SRC}}^2(r_{ab}) \middle\| 0_i^+ \right\rangle \tag{2.66}$$

where $\mathcal{O}_{ab}^F = \mathbb{1}$, $\mathcal{O}_{ab}^{GT} = \sigma_a \cdot \sigma_b$, and

$$\mathcal{O}_{ab}^T = 3(\sigma_a \cdot \hat{r}_{ab})(\sigma_b \cdot \hat{r}_{ab}) - \sigma_a \cdot \sigma_b$$

The quantity r_{ab} denotes the distance between nucleons a and b, and $f_{\mathrm{SRC}}(r)$ accounts for short-range correlations.

The neutrino potential $H_K(r_{ab})$ encodes the momentum dependence of the virtual neutrino exchange and is given by:

$$H_K(r_{ab}) = \frac{2R}{\pi g_A^2} \int_0^\infty \frac{h_K \, j_\lambda(p r_{ab}) \, p^2 \, dp}{\epsilon_K}, \tag{2.67}$$

where $\epsilon_K = p\,[p + E_k - (E_i + E_f)/2]$, $g_A = 1.27$, and $R = 1.2A^{1/3}$ fm. The structure of this potential introduces a characteristic radial dependence into the NME, allowing the matrix elements to be expressed in terms of radial distributions:

$$M_L^{0\nu}(1b) = \int_0^\infty C^{0\nu}(r)\, dr, \qquad M^{2\nu} = \int_0^\infty C^{2\nu}(r)\, dr. \tag{2.68}$$

For $0\nu\beta\beta$ decay, the radial distribution may be decomposed as:

$$C^{0\nu}(r) = C_{GT}^{0\nu}(r) - C_F^{0\nu}(r) + C_T^{0\nu}(r), \tag{2.69}$$

with:

$$C_K^{0\nu}(r) = \sum_{k,ab} \left\langle 0_f^+ \middle\| \mathcal{O}_{ab}^K \tau_a^- \tau_b^- H_K(r_{ab}) f_{\mathrm{SRC}}^2(r_{ab}) \delta(r - r_{ab}) \middle\| 0_i^+ \right\rangle. \tag{2.70}$$

Reference [53] demonstrated that the radial distributions $C^{2\nu}(r)$ and $C^{0\nu}(r)$ exhibit striking qualitative similarities across a wide range of nuclei and model assumptions.

Figure 2·7 shows representative radial distributions for ^{76}Ge calculated within the pnQRPA framework. The similarity in the spatial structure of the two matrix elements suggests that both processes probe related nuclear correlations, despite their different momentum transfers.

While neither $2\nu\beta\beta$ nor $2\nu\beta\beta^*$ decay rates are accurately predicted *a priori* by nuclear models, strong correlations between $2\nu\beta\beta$ and $0\nu\beta\beta$ NMEs have been observed. In practice, calculated $2\nu\beta\beta$ NMEs are often renormalized using an effective axial coupling to reproduce measured half-lives. Despite this adjustment, the relative trends among isotopes remain robust.

Figure 2·8 illustrates the correlation between $2\nu\beta\beta$ and $0\nu\beta\beta$ NMEs obtained using both NSM and pnQRPA calculations. The presence of a clear correlation across different nuclear models supports the idea that improved experimental constraints on $2\nu\beta\beta$, and especially on the more selective $2\nu\beta\beta^*$ transitions, can provide meaningful benchmarks for nuclear structure calculations relevant to $0\nu\beta\beta$ decay.

These theoretical insights provide strong motivation for experimental searches

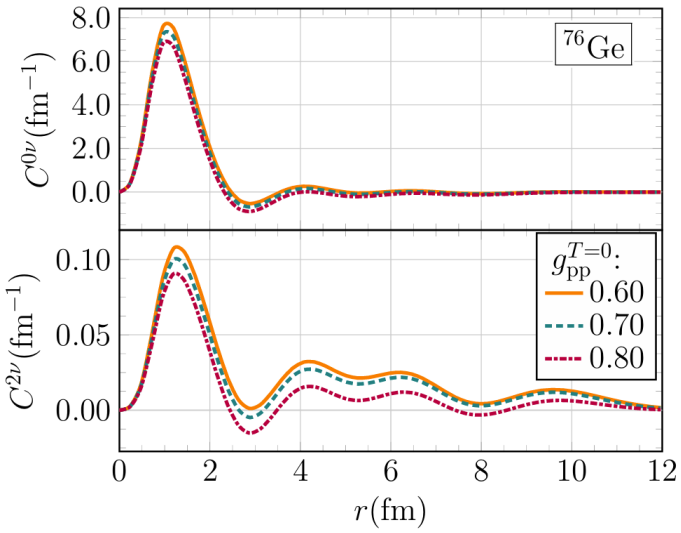

Figure 2·7: Radial distributions of $0\nu\beta\beta$ (top) and $2\nu\beta\beta$ (bottom) NMEs of ^{76}Ge obtained via pnQRPA. Figure taken from Reference [7].

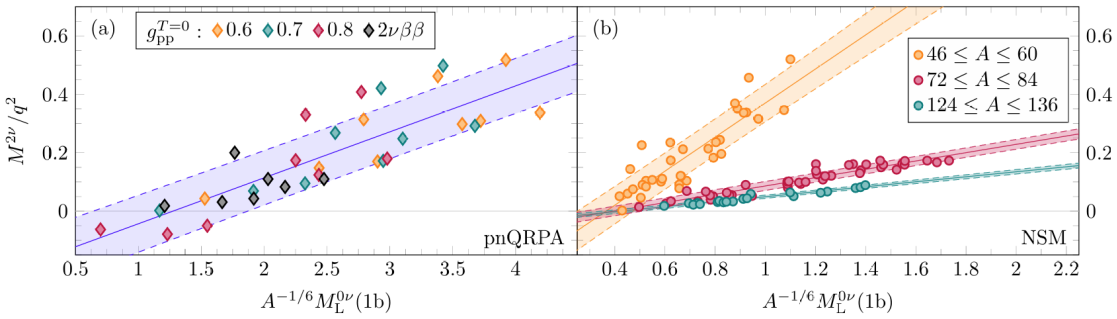

Figure 2·8: Correlation of $2\nu\beta\beta$ and $0\nu\beta\beta$ NME as calculated by NSM (Nuclear Shell Model) and pnQRPA (proton-neutron quasiparticle random-phase approximation) methods. Figure taken from Reference [8].

for $2\nu\beta\beta$ to excited states. Such measurements offer a unique opportunity to test nuclear many-body methods, constrain NME calculations, and ultimately improve the reliability of neutrino mass limits extracted from $0\nu\beta\beta$ decay experiments.

2.8 Double Beta Decay Experiments

If neutrinoless double beta decay ($0\nu\beta\beta$) exists, it is an extraordinarily rare process, with an expected half-life exceeding 10^{26} years for the most favorable isotopes. A confirmed observation would represent the slowest natural radioactive decay ever measured and would provide direct evidence for lepton number violation and the Majorana nature of neutrinos. The extreme rarity of this process imposes stringent requirements on experimental design. Successful $0\nu\beta\beta$ searches must simultaneously maximize signal efficiency while suppressing backgrounds to unprecedented levels. Several key criteria therefore define the performance of modern double beta decay experiments:

- **Excellent Energy Resolution:** The experimental signature of $0\nu\beta\beta$ is a monoenergetic peak at the decay Q value, coincident with the endpoint of the continuous $2\nu\beta\beta$ spectrum. Precise energy resolution is essential to minimize contamination from the $2\nu\beta\beta$ tail within the region of interest (ROI). State-of-

the-art experiments now achieve fractional energy resolutions of order $\sigma_E/E \simeq 0.1\%$, effectively eliminating $2\nu\beta\beta$ as a limiting background.

- **Large Isotope Mass:** Sensitivity to extremely long half-lives requires large exposures, motivating the deployment of tonne-scale quantities of double beta decaying isotopes. Achieving such isotope masses typically demands both isotopic enrichment and scalable detector technologies. In practice, enrichment cost and isotope availability often set the ultimate experimental scale.

- **Ultra-Low Background Environment:** Backgrounds from natural radioactivity and cosmic-ray interactions must be suppressed to levels below one count per tonne-year in the ROI. This necessitates operation in deep underground laboratories, stringent material screening, and detector designs that enable powerful background discrimination.

Among current-generation experiments, KamLAND-Zen has demonstrated world-leading sensitivity to $0\nu\beta\beta$ decay in ^{136}Xe. The most recent KamLAND-Zen result places a 90% confidence level limit on the effective Majorana neutrino mass of $m_{\beta\beta} < (28\text{–}122)$ meV, where the range reflects uncertainties associated with NME calculations. Figure 2·9 shows the corresponding constraints in the $m_{\beta\beta}$–m_{lightest} plane for multiple NME models. The figure highlights the critical role of nuclear theory: for larger NMEs, the KamLAND-Zen limit begins to probe the non-degenerate region of the inverted neutrino mass ordering, whereas for smaller NMEs the constraint remains within the quasi-degenerate regime. KamLAND-Zen is currently the only $0\nu\beta\beta$ experiment whose sensitivity reaches the inverted-ordering parameter space for any NME calculation.

Two-neutrino double beta decay to excited states ($2\nu\beta\beta^*$) has been experimentally observed in only a small subset of known double beta decay isotopes. To date, positive detections have been reported for just two transitions:

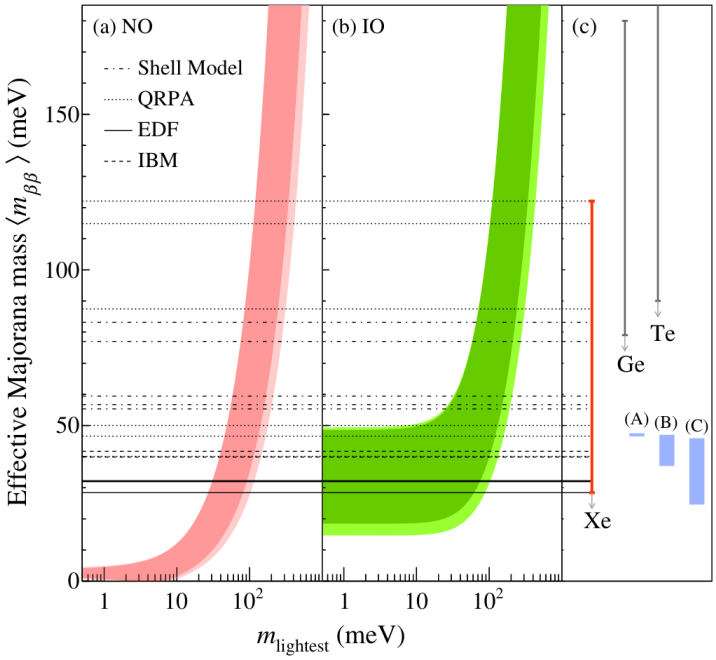

Figure 2·9: Effective Majorana neutrino mass as a function of the lightest neutrino mass state $m_{lightest}$. The shaded regions are based on best-fit values of neutrino oscilation parameters for (a) the normal ordering (NO) and (b) the inverted ordering (IO), the lighter shaded regions indicate the 3σ ranges based on oscillation parameter uncertainties. The horizontal lines indicate 90% C.L. limits on $m_{\beta\beta}$ considering multiple NME calculations. Figure taken from Reference [9].

- $^{100}\text{Mo} \rightarrow {}^{100}\text{Ru}(0_1^+)$, with $T_{1/2} = 5.9^{+0.9}_{-0.6} \times 10^{20}$ years,
- $^{150}\text{Nd} \rightarrow {}^{150}\text{Sm}(0_1^+)$, with $T_{1/2} = 1.33^{+0.45}_{-0.26} \times 10^{20}$ years.

The scarcity of observed $2\nu\beta\beta^*$ transitions reflects the substantial experimental challenges associated with these decays. Relative to ground-state $2\nu\beta\beta$, decays to excited states suffer from significantly reduced phase space and therefore much longer half-lives. However, their distinctive experimental signature, characterized by the coincident emission of de-excitation gamma rays, offers additional handles for background suppression and provides a powerful probe of nuclear structure.

To date, $2\nu\beta\beta^*$ decay has not been observed in ^{136}Xe, the isotope used by KamLAND-Zen and the primary focus of this thesis. The current most stringent limit on this

process:

$$T^{2\nu}_{1/2}(0^+ \to 0^+_1) > 1.4 \times 10^{24} \text{ years} \quad (90\% \text{ C.L.})$$

was established by the EXO-200 experiment [10]. Figure 2·10 shows the EXO-200 spectral fits used to extract this limit. No statistically significant excess consistent with an excited-state signal was observed.

The analysis presented in this dissertation reports the latest search for $2\nu\beta\beta^*$ using KamLAND-Zen 800 data. Leveraging KamLAND-Zen's large ^{136}Xe mass, low background environment, and excellent energy resolution, this work achieves sensitivity beyond the existing EXO-200 limit. An improved constraint on $2\nu\beta\beta^*$ decay in ^{136}Xe would provide an important experimental benchmark for NME calculations and directly inform the interpretation of current and future $0\nu\beta\beta$ searches.

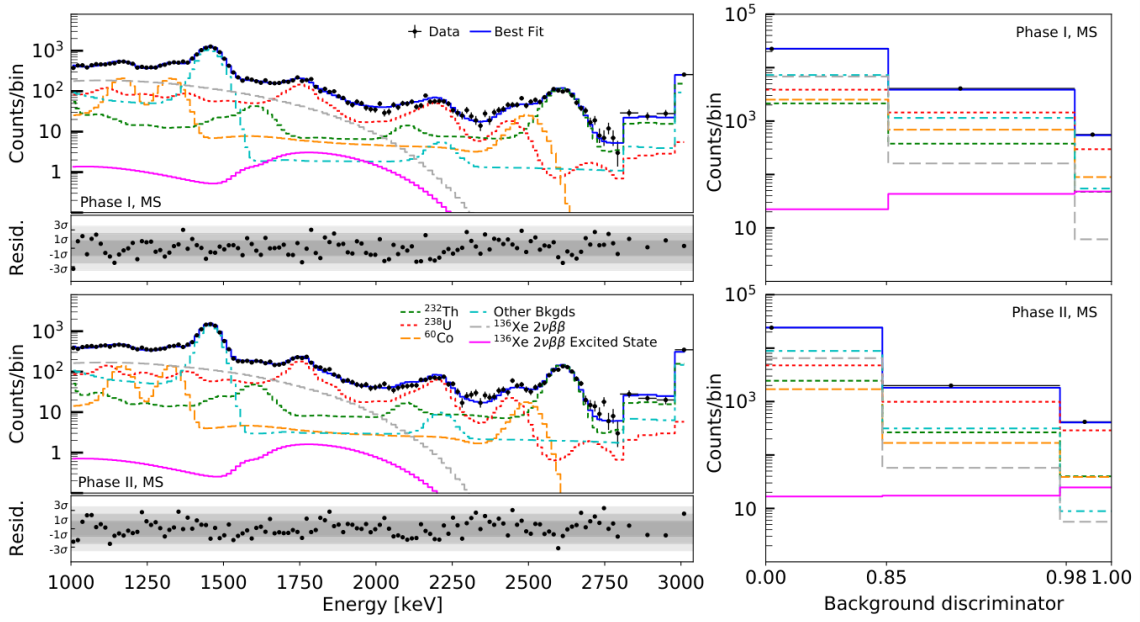

Figure 2·10: EXO-200's fit over energy spectrum (left) and particle ID discriminator spectrum (right) in two data-taking phases of the excited state signal and background. The decay to excited states was not found, and a lower limit was placed. Figure taken from [10].

Chapter 3

The KamLAND-Zen Experiment

KamLAND, the **Kam**ioka **L**iquid-scintillator **A**nti Neutrino **D**etector, is a large liquid scintillator calorimeter detector situated 1km below mt. Ikenoyama in Gifu prefecture, Japan. I will describe the KamLAND detector's and the corresponding KamLAND experimental area's important components and features in this chapter. I will also explain how each component contributes to the KamLAND's scientific goals and the work of this thesis.

3.1 KamLAND

One can think of KamLAND as an onion made up of many spherical layers, each layer serving the ultimate goal of shielding and observing the central core, the xenon-loaded liquid scintillator.

3.1.1 Detector Infrastructure and Outer Detector

The KamLAND detector is surrounded by the KamLAND experimental area, situated in an old iron mine, multiple caverns and passageways were excavated and set aside for KamLAND experimental use.

The KamLAND site is shown in Figure 3·1. The control room contains networking and monitoring equipment which on-site shifters use to observe real-time detector activity. The first LS purification areas contain liquid-liquid extraction and nitrogen purge purification systems. The second LS purification area contains a distillation

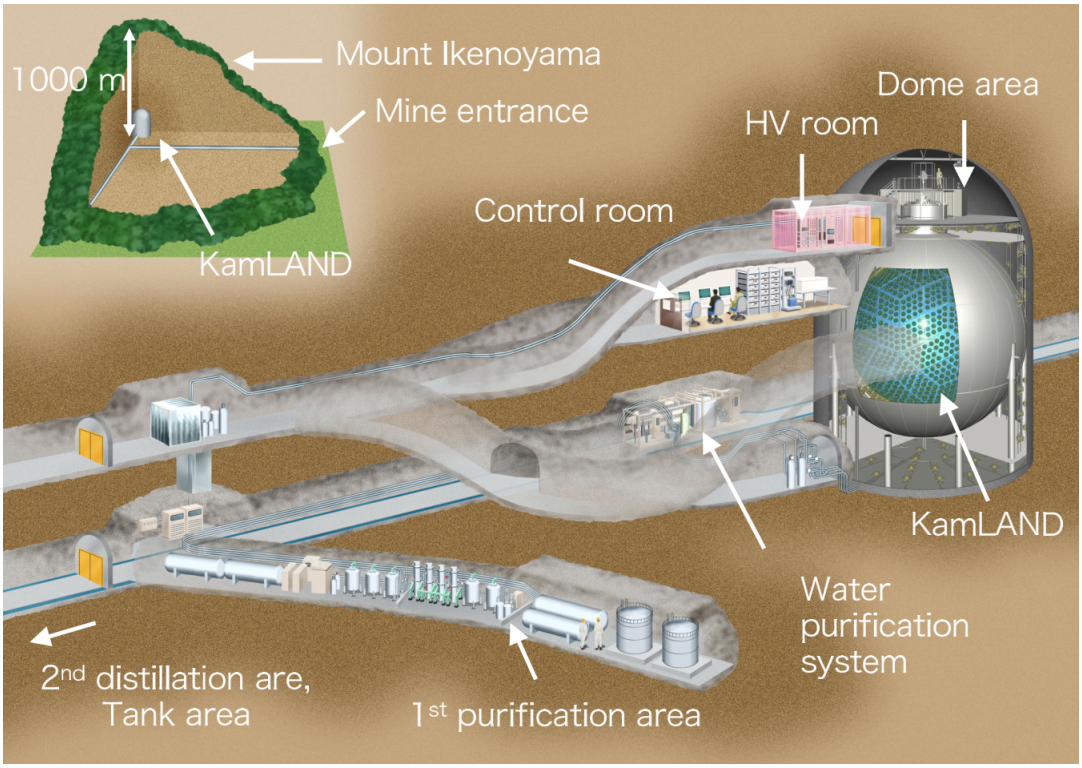

Figure 3·1: KamLAND site

purification system. A new Xenon purification area was built for KamLAND-Zen. The dome area is a class 1,000 clean area atop the detector and includes a calibration source preparation room and electronics enclosure (electronics hut or e-hut). At the center of the dome area, there is a secondary class 100-1000 clean tent covering the KamLAND chimney. The inner balloon installations took place in August 2016 and May 2018 inside this clean tent.

The outer detector (OD) is a cylindrical water tank 20m tall and with 20m diameter and filled with pure water. The OD was refurbished in 2016, and 140 new 20-inch PMTs (R3600) were installed inside the cavity. The inner wall of the outer tank and the outer surface of the inner detector stainless steel spherical tank are covered highly reflective Tyvek sheets (Tyvek 1073B and 1082D) to collect as much of the light generated by crossing cosmic ray muons as possible. The outer detector's role is

to tag cosmic ray muons, shield radioactivity and fast neutrons from the outer rock, and to stabilize the temperature of the ID.

3.1.2 Inner Detector

KamLAND's inner detector (ID) is the main spherical liquid scintillator detector, it is shown in Figure 3·2. The ID is contained in a 18m diameter stainless steel sphere tank. 1,879 PMTs are mounted onto the inner wall of the ID, 1,325 17-inch and 554 20-inch PMTs. The PMTs are submerged in non-scintillating buffer oil (BO). An acrylic panel separates the buffer layer into two shells. This panel prevents the convection of radon out-gassed from PMT glasses into the central parts of the detector.

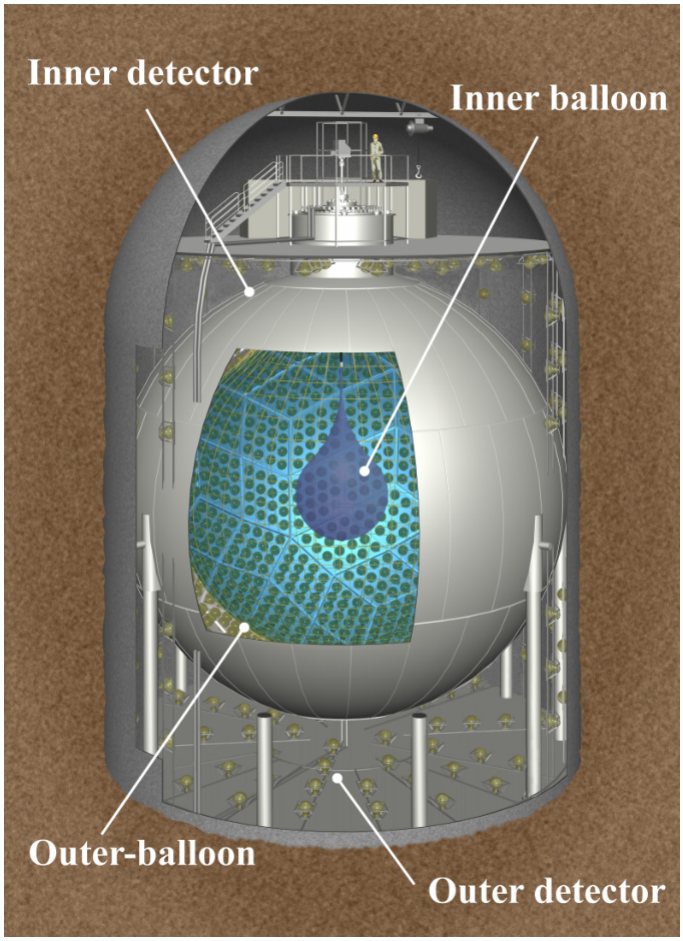

Figure 3·2: KamLAND-Zen detector

Photomultiplier tubes (PMTs) are KamLAND's eyes, detecting individual photons of light emitted by the passage of charged particles through the liquid scintillator volumes. Photons that hit PMT photocathodes are converted into a photoelectron. This photoelectron is then guided by electric fields to a series of dynodes. Each dynode multiplies the photoelectrons many times over, until the first photoelectron becomes 10^{6-7} electrons. Should multiple photons hit the photocathode simultaneously, the output voltage increases proportionally. This current is converted to a voltage by a coupling capacitor and read out via long coaxial cables. Figure 3·3 is a diagram of the 17in and 20in PMTs.

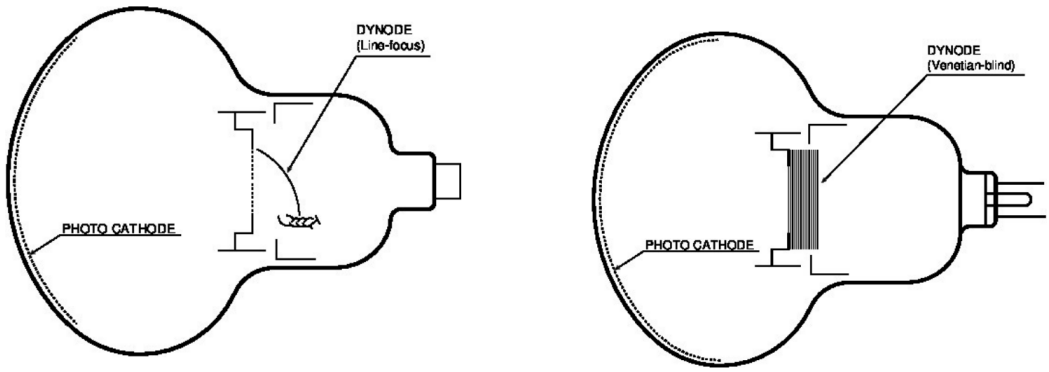

Figure 3·3: 17-inch and 20-inch PMTs, both have the same footprint, but the 17-inch PMT photocathode is masked to a 17-inch diameter.

The 1,325 17-inch PMTs are Hamamatsu R7250s while the 554 20-inch PMTs are Hamamatsu R1449s and R3600s. The 20-inch PMTs were inherited from the Kamiokande experiment to increase our light collection. Both sets of PMTs have a bialkali photocathode sensitive to 300-650nm light which is well-suited for the emission spectrum of the LS. The pmts also differ by dynode design; while the 17-inch PMTs feature "box-and-line" designs, the 20-inch PMTs have "venetian-blind styles". The different dynode designs along with the masking on the 17-inch PMTs, give us 17-in PMTs with better transit time spread (TTS) and 20-inch PMTs with better light collection efficiency. In total, the photocathode coverage of the ID is 34%, with 23%

contributed by the 17-inch PMTs.

Furthermore, the PMT performance can be affected by the earth's magnetic field. To reduce this unwanted effect, the entire KamLAND detector is surrounded by geomagnetic compensation coils to counteract this external magnetic field. The residual magnetic field is less than 50mG, which has negligible effect on the PMT performance.

Another important characteristic of PMTs is their quantum efficiency (QE). The QE quantifies the probability that a photon arriving on the photocathode will produce a photoelectron. A PMT's QE varies over the wavelength of the incoming light. To improve our light collection, KamLAND's LS is doped with PPO to shift the wavelength of the incoming light to where the PMTs are most sensitive. Figure 3·4 shows the PMT QE curve and the PPO reemission spectrum.

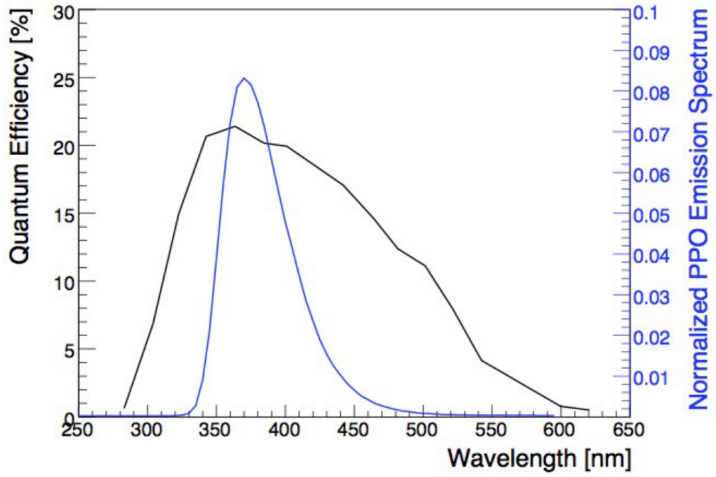

Figure 3·4: Quantum Efficiency of the KamLAND inner PMTs and PPO emission over wavelength. Figure taken from [11]

Next, is the 13m diameter outer balloon (OB). The OB is suspended in the center of the ID within the buffer oil, it is filled with one kiloton of highly purified organic liquid scintillator.

3.1.3 Liquid Scintillator

Liquid scintillator (LS) is the vital medium that sensitizes KamLAND to internal radioactivity. The KamLAND LS (KamLS), found in between the outer balloon and inner balloon, is composed of 80.2% of dodecane (D12),1,2,4-trimethyl benzene, and 19.8% pseudocumene (PC). A wavelength shifter called 2,5-diphenyloxazole (PPO) is added to the LS at a concentration of 1.36 ± 0.03 g/L. KamLAND-Zen has achieved 5×10^{-18} g/g and 1.3×10^{-17} g/g contamination for 238U and 232Th, respectively. The chemical composition of the KamLS can be found in Table 3.1

	D12	PC	PPO
Chemical Formula	$C_{12}H_{26}$	C_9H_{12}	$C_{15}H_{11}NO$
Density $[g/cm^3]$	0.7526	0.8796	-
Boiling Point [°C]	216	169	360
Melting Point [°C]	-10	-44	72
Flash Point [°C]	83	54	-

Table 3.1: Composition and properties of KamLAND Liquid Scintillator (KamLS)

3.1.4 KamLAND-Zen and XeLS

At the center of KamLAND-Zen lies the Xenon-loaded Liquid Scintillator (XeLS) contained in the 1.9m radius inner balloon (IB). The double-beta decaying isotope ^{136}Xe is thus placed in the cleanest, most sensitive part of the experiment. The Xenon gas is enriched to 90% ^{136}Xe and is dissolved into a modified version of KamLS. The PPO concentration was increased to 4g/L to boost the light yield. This increased PPO concentration compensates for the 10% reduction in emitted scintillation light when Xenon is mixed into the LS. The XeLS density is also tuned to match the surrounding KamLS. The chemical composition of the XeLS is shown in Table 3.2 in each of the different phases of the KamLAND-Zen experiment.

Material	Decane (%)	PC (%)	PPO (%)	Xe (%)
Zen 400 Phase-1	82.3	17.7	2.7	2.44/2.48
Zen 400 Phase-2	80.7	19.3	2.29±0.03	2.91
Zen 800	82.4	17.6	2.38±0.02	3.13

Table 3.2: Composition of XeLS from three phases of KamLAND-ZEN

3.2 Chemical Handling Infrastructure

Background mitigation is crucial for $0\nu\beta\beta$. Maintaining the purity of the liquid volumes inside KamLAND is an important part of background mitigation in KamLAND-Zen. In this section, we will briefly describe the systems that provided or maintain the purity of the LS and XeLS in KamLAND.

3.2.1 Water Extraction

The first purification is shown in Figure **??**. Both the liquid scintillator and buffer oil are filtered in two stages with 1μm and 0.1μm pore sizes respectively. Next, the liquids are flushed with pure water in the water extraction tower where metals such as U, Th, and K, are absorbed by the water. Finally, the liquids are purged with ultra-pure nitrogen gas to remove gaseous contaminants like radon and oxygen.

3.2.2 Distillation

The next purification system utilizes the distillation system shown in Figure **??**. LS from KamLAND is constantly cycled through the distillation system. There boiling is done to separate the individual chemical components of KamLS, namely Pseudocumene (PC) and PPO. Each component is individually distilled and purified. Then, the components are combined in the mixing tank to the original LS composition with an accuracy of $10^{-3} g/cm^3$. Finally high-purity nitrogen gas is used to purge the LS coming out of the mixing tank to eliminate any gaseous contaminants.

3.2.3 Xenon Handling

A schematic diagram of the XeLS handling system is shown in Figure 3·5. The system consists of the following components:

- A **1.1 m^3 Main Tank** directly connected to KamLAND-ZEN's inner balloon. The extracted XeLS first enters this tank.
- A **1.1 m^3 Reservoir Tank** that is connected to the main tank via a vacuum pump and LS trap. It is refrigerated with liquid N_2 to -50°C, at which the LS gas is condensed and trapped. Only Xe gas is allowed to flow into the reservoir tank.
- A **25 m^3 Storage Tank** is connected to the main tank. The degassed LS is poured into this tank for storage.
- A **1.1 m^3 Sub-tank** is also connected to the main tank, the detector, the control tank, and the purified Xe gas system. The Xe gas is mixed into LS inside this tank. The density of chemical cocktails in the sub-tank is monitored and adjusted by the control tank. After mixing, the XeLS is filtered and fed back into the balloon.
- A **1.1 m^3 Control Tank** is directly connected to the second purification area. The control tank controls the density in the sub-tank by adjusting the Decane percentage. The control tank is pressurized with Nitrogen gas.

3.3 Data Acquisition

3.3.1 KamLAND DAQ

KamLAND uses two data acquisition (DAQ) systems in parallel. The first is Kam-FEE (KamLAND Front End Electronics), which has been used since the start of

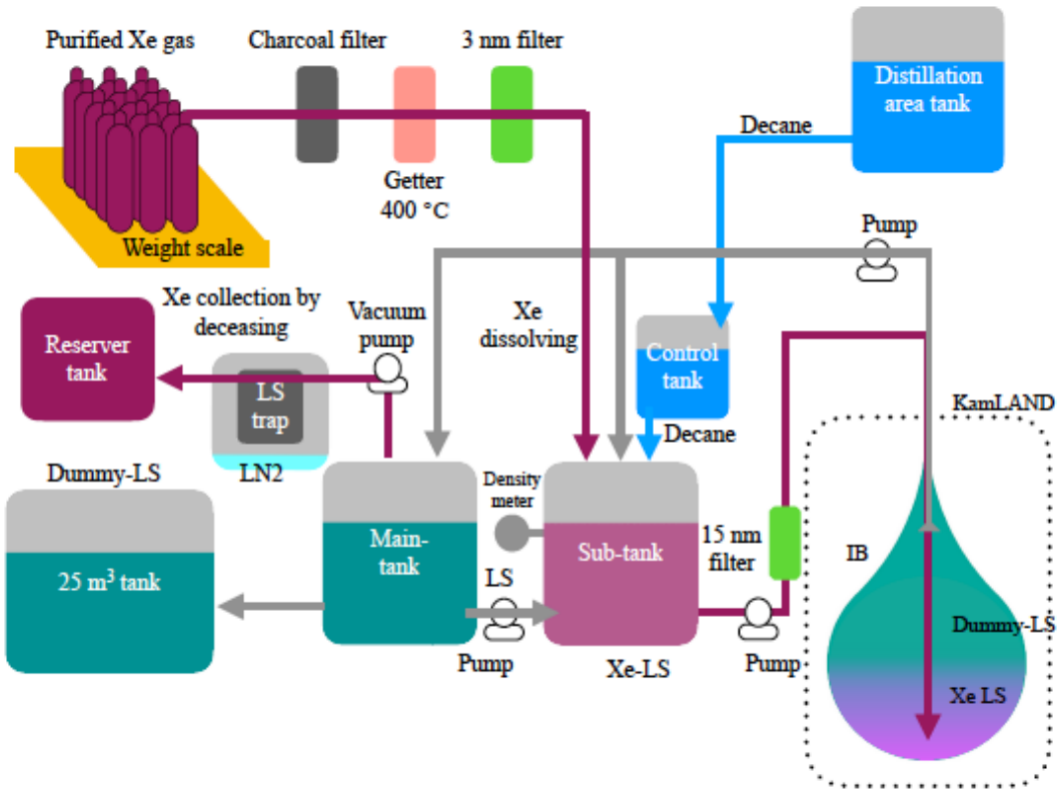

Figure 3·5: Flow diagram of the KLZ Xenon system. The purple lines denote the flow of Xe/XeLS, the blue line denotes the flow of decane, the the grey line denotes the flow of LS. Figure from Reference

KamLAND physics data-taking. The other is MoGURA (Module for General-Use Rapid Application). MoGURA is a data acquisition system developed to eliminate the deadtune just after cosmis ray muon events. An overview of this dual scheme data acquisition system is shown in 3·6. What follows is a brief description of each DAQ system.

3.3.2 KamFEE DAQ

KamFEE are the front end electronics that read and control the KamLAND PMTs. The boards are of VME 9U form factor and are synchronized with a 40 MHz clock. The PMT signals are sent along two parallel channels. The first channel is sent to a

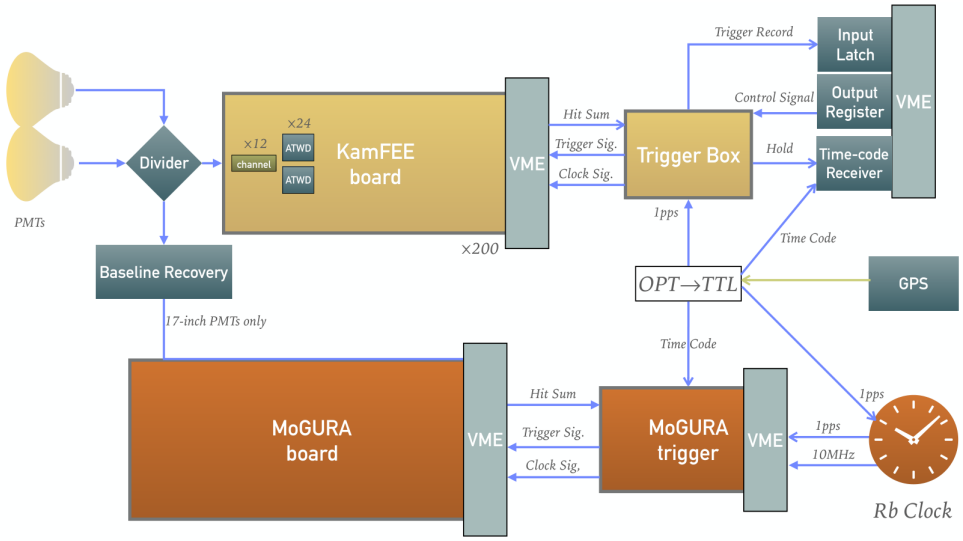

Figure 3·6: Flow diagram of the KamLAND data acquisition system, taken from [12]

discriminator which register a PMT hit if the voltage exceeds a predetermined value that corresponds to approximately 1/6th of a single photoelectron. The second channel, is delayed to give some time to process the discriminator signal and is fed into 3 amplifier stages (x20, x4, x0.5), this amplified signal is digitized by two analog Transient Waveform Digitizers (ATWDs). The ATWD is a 10-bit digitizer and samples every 1.5ns, 128 times per waveform. Each pulse takes 128 μsec to digitize.

The KamFEE boards send a "hitsum" signal to the central KamFEE DAQ trigger, communicating a certain number of hits were received and can be digitized. The trigger board sends a signal back which issues the digitization command to the ATWDs. While the ATWD is digitizing, it cannot record further signals, therefore, two ATWDs are assigned to each channel to reduce deadtime.

3.3.3 MoGURA

MoGURA is the secondary data acquisition system in KamLAND; it is responsible for after pulses and dealing with PMT waveform overshoots caused cosmic muons.

KamLAND has a cosmic muon rate of 0.3 Hz, so it is important to compensate for the effects these high-energy events have on our detector. To accomplish this task, MoGDAQ has a few extra features over KamFEE.

- **Baseline Recovery:** After a high energy muon passes through the detector, the DAQ channels are saturated, which means the voltage exceeds the digitization window, so only the maximum value is read. Simultaneously, the voltage "overshoots" as it returns to normal and swings below the nominal value causing difficulties in digitizing signals that occur soon after these muons.

- **Adaptive mode:** Activates a special trigger mode after muon events to compensate for large after-pulses post-muon. This special trigger is based on differential PMT hits.

MoGURA data is used to tag neutrons created from muon spallation. These tagged spallation neutrons are vital in subsequent analyses to tag events that likely originated from these cosmic ray muons. The baseline restoration and neutron tagging will be further improved with the implementation of MoGURA2 trigger system. This is a planned replacement of the KamLAND data acquisition system (KamFEE and MoGDAQ both) for the KamLAND2-ZEN experiment, which is planned to begin physics data-taking in 2028.

3.4 KamLAND-ZEN Phases

The KamLAND-ZEN experiment has undergone multiple phases and renovations.

3.4.1 KamLAND-ZEN 400

The inner balloon and XeLS was added to the KamLAND experiment in 2011, starting the phase referred to as KamLAND-ZEN 400. This phase of the detector featured

a 3m diameter inner-balloon filled with liquid scintillator loaded with 3% Xenon by weight. The dissolved Xenon gas had 91% proportion of Xe^{136}.

The KamLAND-ZEN 400 data was split into two data-taking periods. Period-I data was contaminated with a high background of Ag^{110m}, the silver appeared to be leeching from the mini-balloon into the XeLS. The Ag^{110m} contamination on the inner balloon was likely due to nuclear fallout from the Fukushima reactor meltdown. The Fukushima meltdown occurred when the inner balloon was being manufactured and in the same geographical region of Japan. Period II started after the XeLS distillation suppressed the Ag^{110m} by a facator of 20. Period II continued data taking for 534.5 total livedays and the combined physics result of Periods I and II produced a $0\nu\beta\beta$ half-life limit of $T^{0\nu}_{1/2} > 1.07 \times 10^{25}$ years at 90% C.L. This half-life limit corresponds to an effective majorana mass limit of $m_{\beta\beta} < 61 - 165$ meV.

3.4.2 KamLAND-Zen 800

KamLAND-Zen 800 was the second phase of KamLAND-Zen. KamLAND-Zen took data from January 2019 to August 2024. Over 2kton·yrs of exposure was observed. KamLAND-Zen 800 was decommission in Fall 2024, and is currently being dissassembled.

Inner Balloon Manufacturing

KamLAND-Zen 800 featured a larger, cleaner inner balloon which was fabricated at Tohoku University in a Class 1 cleanroom. The inner balloon is made from panels of 25 μm nylon-6. Innerballoon fabrication consisted of multiple steps some of these critical steps are listed here:

- **Washing** - the film is cleaned twice in an ultrasonic bathtub, then stored between cover films to prevent dust adhesion

- **Welding** - the cleaned balloon panels are welded with a semi-automatic welding machine. For delicate areas, such as the balloon neck, a hand welding machine was used. The average tensile strength on the balloon surface was 35 N/cm after welding.

- **He Leak Check** - Inevitably leaks will occur during the previous assembly procedures. Helium gas was pumped into the balloon to check for these leaks. The cover film of the balloon was peeled off before this leak check. Found leaks were repaired by patching the film. Over 900 leaks were found during the leak check.

- **Folding** - The inner balloon was folded into a cylinder shape and covered with sheath films to prevent contamination during transport. Teflon sheets and Vectran strings were used to tie the rolled balloon up for shipping.

- **Shipping** - The inner balloon was shipped within a silver gas bag. All corresponding tools were also shipped in airtight bags.

The inner balloon was installed on May 10, 2018. A rehearsal installation was performed in a swimming pool before the final deployment. In the final installation, the balloon is deployed through the 50cm port on the neck of the KamLAND detector. After filling the balloon with KamLS, the Teflon sheets, sheath films, and Vectran strings are pulled out of the detector. The whole operation was monitered in real-time via cameras and endoscope.

The top of the inner balloon is connected to a corrugated tbue made from PEEK (poly-ether-ether-ketone). Twelve suspending belts support the inner balloon, wrapping around the full height of the balloon. The tension of each of these belts are monitored in real time to guarantee the position and stability of the balloon. A schematic of the balloon structure can be seen in Figure 3·7.

Contamination Control

Once deployed and exposed to the KamLAND scintillators, the inner balloon is very difficult to clean. Thus, maintaining balloon cleanliness is vital. After deployment, the IB was filled with distilled LS while the ^{232}Th level was measured at 10^{-15}g/g, exceeding the target background concentration. The PPO distillation tower was suspected to be a source of contamination and was investigated. ICP-MS and neutron activation analysis were used to measure ^{232}Th contamination at different locations along the distillation system. After meticulous washing and filter replacement, LS purification began to lower the ^{232}Th background. After two separate distillation campaigns, ^{238}U and ^{232}Th levels were reduced by a factor of 10 compared to KamLAND-ZEN 400. The contaminations can be estimated by performing a ^{214}Bi-^{214}Po and ^{212}Bi-^{212}Po coincidence analysis. The coincidence event rates plotted over time are shown in Figure 3·8 and listed in Table 3.3.

	^{238}U (10^{-17} g/g)	^{232}Th (10^{-17} g/g)
Zen 400 Phase-1	13±2	190±20
Zen 400 Phase-2	17±1	5.5±0.3
Zen 800	1.5±0.4	30±4

Table 3.3: Film Contamination three phases of KamLAND-ZEN. Values taken from [1]

KamLAND-ZEN 800 was decomissioned in 2024 after observing over 2 kiloton·yrs of exposure. The final half-life limit was reported as $T^{0\nu}_{1/2} > 3.8 \times 10^{26}$ years at 90% C.L. This half-life limit corresponds to an effective majorana mass limit range of 28-122 meV. As of Summer 2025, this is the world-leading limit on effective majorana mass from any double-beta decay isotope and is the only limit in the Inverted Mass Ordering region. The latest limits from KamLAND-ZEN800 are shown in Figure 3·9

3.4.3 KamLAND2-ZEN

KamLAND2 is the next generation of the KamLAND experiment, it will be built in the same detector cavern as KamLAND1. KamLAND2-ZEN will reach a goal limit of $T_{1/2}^{0\nu\beta\beta} > 2 \times 10^{27}$ yrs.

Most of the detector components will be replaced going from KamLAND to KamLAND2. Some of the more notable upgrades are:

- **Inner Detector PMTs** - All of the 1,879 inner PMTs will be replaced with modern low-TTS, high quantum efficiency (QE) phototubes.
- **Light Collecting Mirrors** - Light collecting winston cones will be attached to each of the PMTs to achieve virtually 100% photocoverage. These improvements will contribute to a goal energy resolution of 2%. This energy resolution will lead to a x100 reduction in the $2\nu\beta\beta$ background rate.
- **Improved Inner Balloon** - The new innerballon will be made up of PEN (polyethylenenapthalate) which will scintillate from film radioactive backgrounds
- **MoGURA2** - Replace the 2 DAQ systems with MoGURA2, a newly developed, compact, dead-time free, RFSoC electronics.

KamLAND2-ZEN is scheduled to begin data-taking in 2028.

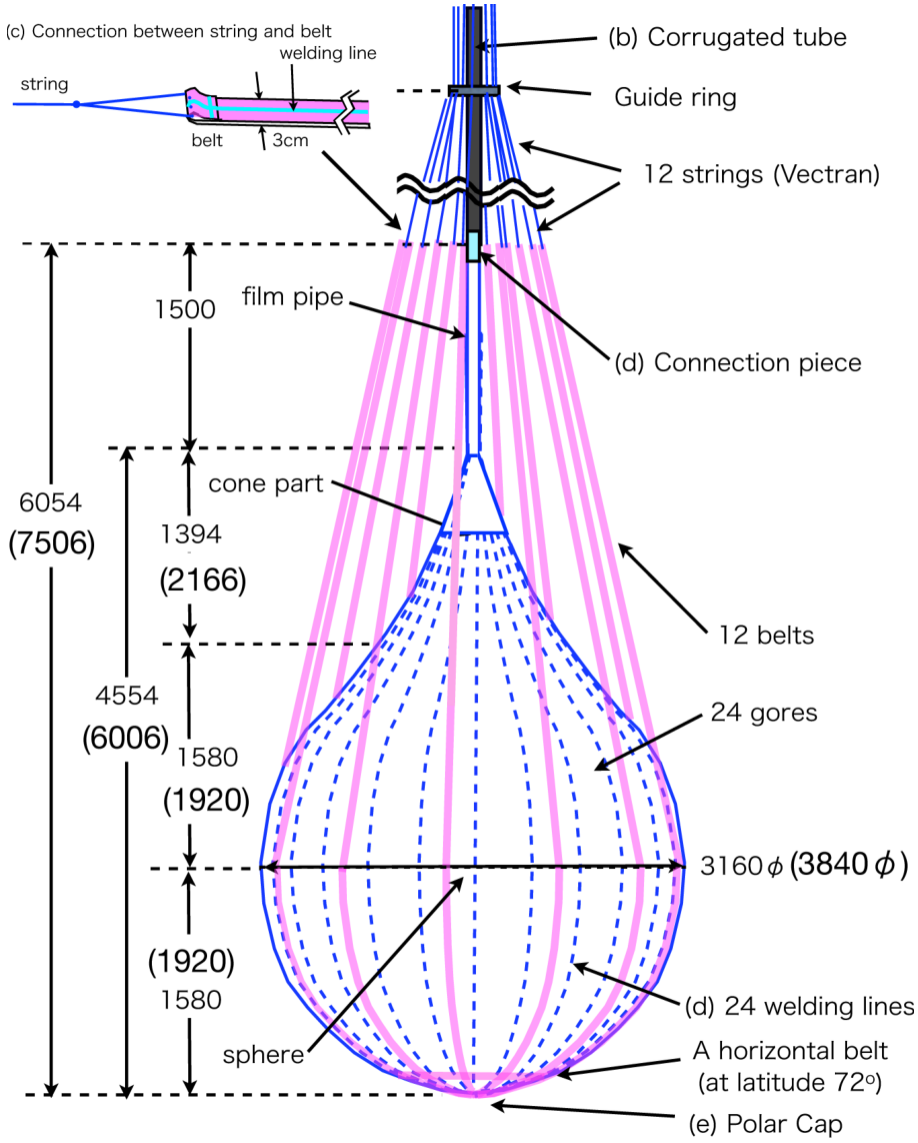

Figure 3·7: Inner balloon structure and measurements for KamLAND-ZEN 800 configuration, taken from [1]

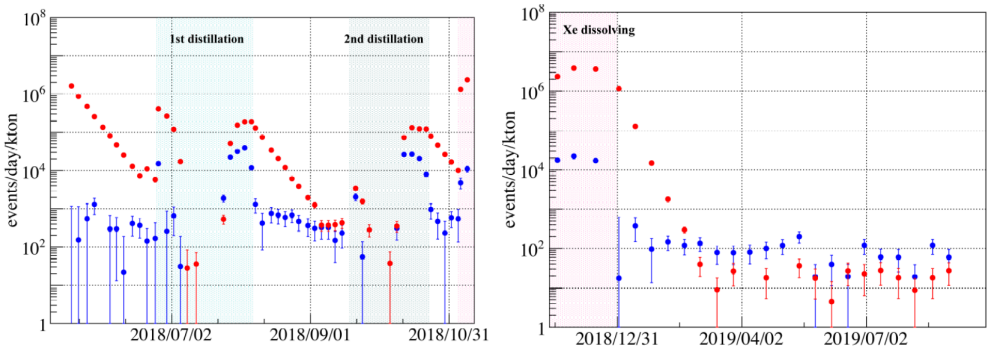

Figure 3·8: Coincidence event rate in KamLAND-ZEN 800 during the first distillation campaign, second distillation campaign, and Zenon loading phase. The red points denote ^{214}Bi and the blue points denote ^{212}Bi. Figure taken from [12].

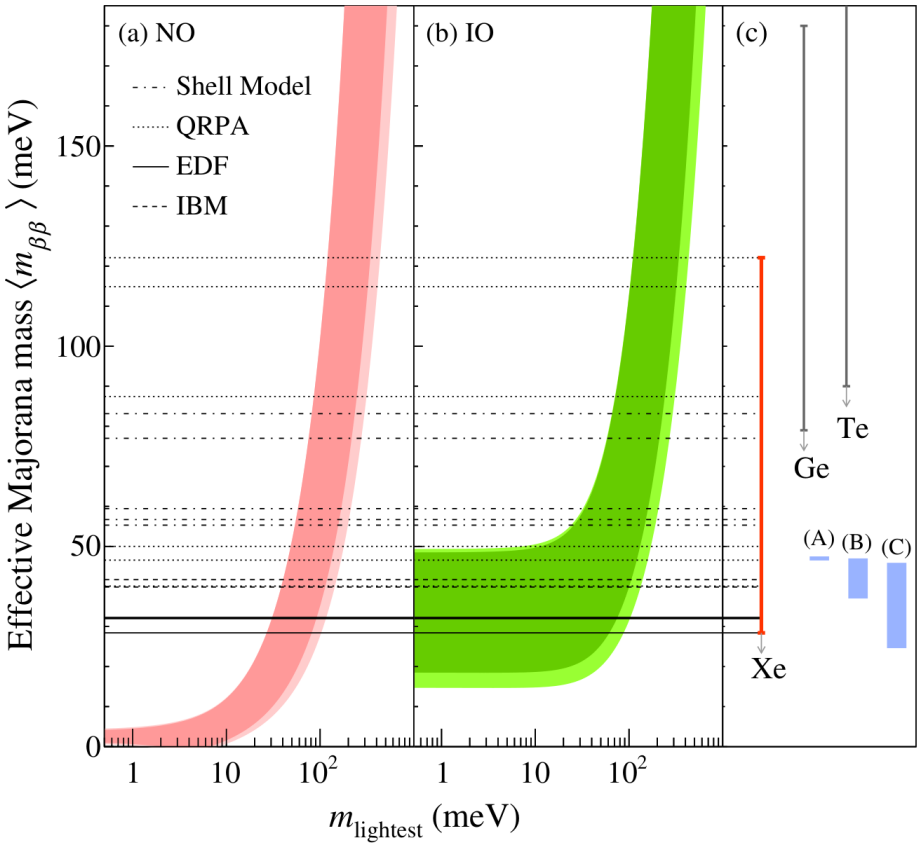

Figure 3·9: Effective Majorana neutrino mass $m_{\beta\beta}$ as a function of the lightest neutrino mass $m_{lightest}$. The dark shaded regions are based on the best-fit neutrino oscillation parameters, while the lighter regions indicate 3σ ranges calculated from oscillation parameter uncertainties [13] [14]. The horizontal lines indicate various 90% C.L. upper limits on $m_{\beta\beta}$ from KamLAND-ZEN's ^{136}Xe results and a few different NME calculations. The blue bars on the right indicate three different theoretical predictions in the IO region. [15]

Chapter 4

Event Reconstruction and Selection

KamLAND-ZEN uses detailed simulations defined in KLG4Sim, a GEANT4-based Monte Carlo (MC) simulation software. The MC simulated events are tuned with real calibration events to carefully match the real detector response. Simulated and physical events produce detector responses that are reconstructed to extract higher-level information such as energy and position. The reconstructed event information is used for data selection and spectrum fitting. This chapter discusses the MC simulation and event reconstruction procedures used in KamLAND-ZEN 800.

4.1 Analysis Framework

4.1.1 Data Flow

Figure 4·1 outlines the data flow in KamLAND-ZEN. PMT signals are digitized in either KamFEE or MoGURA, the two DAQ systems discussed in the previous chapter. The digitized signals are stored in Kinoko Data Format (KDF). KDF files contain trigger information and timestamped, digitized PMT waveforms. KDF files also store run condition information in the header. The EventBuilder collates the waveforms of a single event and stores them in a serial file. A waveform analyzer reconstructs hit time and charge (TQ) information for each of these waveforms. The RTQ files hold the Raw-TQ information for each PMT. Event vertices and visible energy are derived from the RTQ files through their respective reconstruction algorithms. There are secondary reconstructions that are also applied to the RTQ files, such as muon

track fitting, flasher vetoes, double pulse fit, and unphysical event selections. The general vector file (GVF) is used for the main physics analyses like the one presented in this thesis.

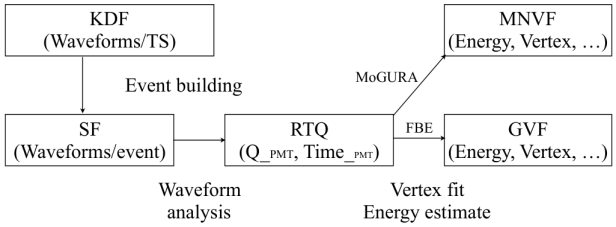

Figure 4·1: Data flow in KamLAND from raw waveforms to analysis variables such as energy, vertex, total hit PMTs, etc. [1]

GVF files contain the following information:

- **run number**
- **event number**
- **TimeStamp** based on DAQ clock time (25 ns for KamFEE, 20 ns for MoG-DAQ)
- **unixtime** is the number of seconds since January 1st, 1970 and is used for some run vetoes
- **trigger type** records which trigger was used
- **event vertex and badness** event vertices and a radius from the detector center are saved, along with a vertex fit quality parameter called badness
- **energy/energy17** visible energies given by the fitter; energy17 is the energy estimate using only 17-inch PMTs
- **TotalChargeID/17/OD** sum of all PMT charges of each PMT type
- **numhit/numhit17** the number of hit PMTs/17-inch PMTs in each event

- **NsumMax** the maximum number of hit PMTs in a single DAQ cycle within each event, a "peak" nhit of the event
- **N200OD** maximum number of simultaneous hit OD PMTs within 200 ns windows
- **muon entrance and direction** muon fitter results are recorded

Finally, MoGURA events are associated with muon events acquired in KamFEE DAQ (FBE) and stored in a Muon-Neutron Vector File (MNVF) to search for neutron capture events that occur shortly after muons.

4.2 Event Reconstruction

4.2.1 Waveform Analysis

Each digitized waveform has 128 samples with 1.5 ns sample intervals, corresponding to a waveform digitization window of 192 ns. The waveforms are processed and TQ values are reconstructed using the following procedure:

- **Smoothing** Each waveform is smoothed using a running-average first derivative.
- **Baseline adjustment** The baseline of each PMT is collected at the beginning of each run. This baseline is subtracted from each waveform.
- **Peak finding** Peaks are found with running-averaged 1st, 2nd, and 3rd derivatives.
- **Leading-edge and Trailing-edge tag** A leading-edge is stamped as 10 ns before the peak voltage. The trailing edge is stamped when the waveform returns to baseline. An example of this time-stamping is shown in Figure 4·2.

- **Waveform Sum calculation** The waveform is integrated from the leading-edge to the trailing-edge.

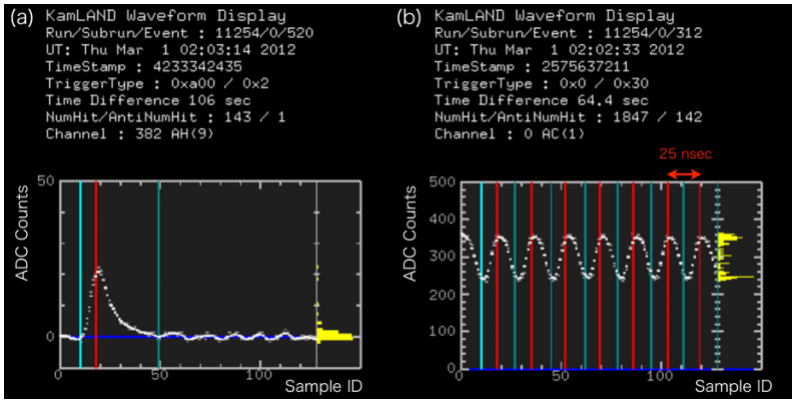

Figure 4·2: An example of waveform analysis from thesis [16]. (left) ADC counts of a real waveform after baseline subtraction. The left cyan line is the leading edge, the center red line is the peak position, and the right dark cyan line is a trailing-edge. (right) Clock calibration example on 25 nsec intervals.

When there are multiple hits in a single PMT waveform, the total charge of the hits and the earliest hit time are returned. This simplified information is used for vertex and energy reconstruction. The multi-photoelectron (multi-pe) information is used for double-pulse fitting and muon shower tagging.

4.2.2 PMT Corrections

Low Gain Problem and HV Reductions

Since approximately 2011, it has been observed that the gain of some 17-inch PMTs gradually decreased. As the gain of the PMTs fell, this compromised the signal-to-background ratio and PMT waveform quality. It was also observed that the PMTs entered a low impedance state before the gain dropped. An HV current and voltage monitor allows for real-time monitoring of this state. Usually, a simple HV power cycle could recover normal PMT behavior. Since 2016, an automatic HV power cycle mechanism has been implemented to mitigate the low gain problem, but the root

cause is still unknown.

Each time the PMTs enter the low impedance state, the HV on that channel was reduced in 50–100 V increments. Over time, some of the channels had their HV reduced by up to 450 V. Figure 4·3 shows the trend in low gain 17-inch PMTs.

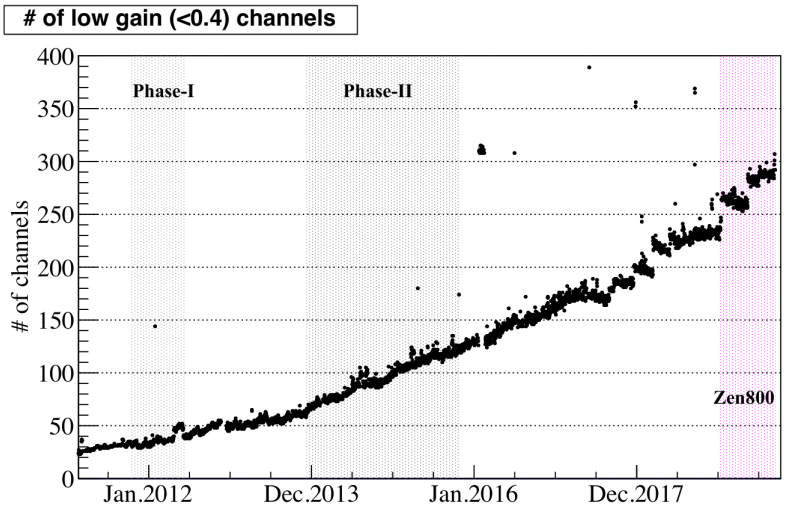

Figure 4·3: The trend in the number of low gain 17-inch PMTs, before ZEN-800. The number of low gain channels increased gradually, while the sudden increases are from HV reductions performed since 2017 [1].

Note about current low pmt gain analysis.

Bad Channel

A channel is considered bad if the PMT meets one or more of the following criteria:

- PMT pulses less than 0.6% of the time over all events
- PMT pulses below 0.48% for non-muon events
- PMT pulses less than 80% of the time for high-energy muon events
- PMT is missing a waveform more than 10% of the time
- Large discrepancy between the two ATWD hits

- High muon charge PMTs. A PMT may read much higher charge ($Q_{detected}$) than the average of its surrounding PMTs ($Q_{expected}$). A run is divided into 100 muon intervals; for each interval the criteria is defined as

$$\frac{1}{N_{interval}} \sum_{i=1}^{N_{interval}} \left(\frac{1}{N_{muon}} \sum_{j=1}^{N_{muon}} \frac{(Q_{expected} - Q_{detected})^2}{Q_{expected}} \right) > 1000 \; p.e.$$

These bad channels are excluded from event reconstruction and physics analyses.

Dark Hit

Thermal fluctuations can emit electrons off the photocathode, leading to a PMT hit signal. These "dark hits" are an unavoidable hit-level background in PMT detectors; lowering the detector temperature reduces this effect. The dark hit rates are measured from run to run and are factored into our likelihood-maximizing reconstruction algorithms. The hit rate observed 50-100 ns before the PMT hit time rising edge is taken as the dark rate. Figure 4·4 shows the PMT hit time distribution and the dark rate window.

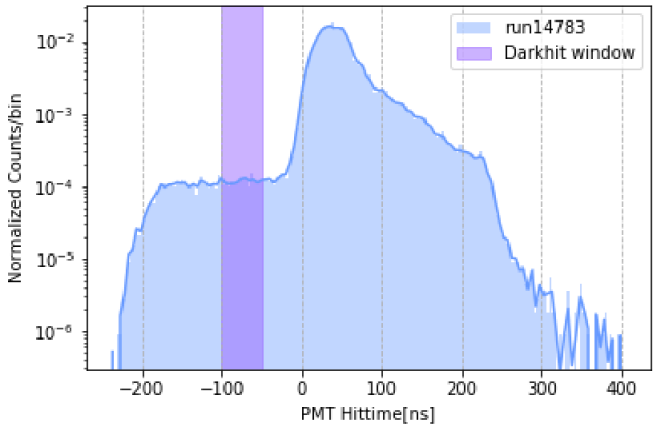

Figure 4·4: An example pmt hit time distribution from data run 14783, the 50-100 ns leading window is taken to measure the pmt dark hit rate. [12].

4.2.3 Primary Vertex Fitter

The primary vertex fitter provides a rough estimate of a scintillating event's location. This estimate serves as the input to a more thorough, but complex, secondary fitter. The fit works by constructing a hit time residual distribution:

$$T_i^{emit} = T_i - TOF_i = T_i - \frac{|R_i - r_{vertex}|}{c_{eff}} \tag{4.1}$$

Here T_i is the hit time of the i^{th} PMT, TOF_i is the time it takes for a scintillation photon to traverse from the vertex position to the i^{th} PMT position, R_i is the PMT position, r_{vertex} is the unknown vertex position to fit for, and c_{eff} is the speed of light in the given medium. By fitting T_i^{emit} to match the standard scintillation time profile, a primary r_{vertex} is produced by the fitter.

4.2.4 Secondary Fitter

The secondary V2 fitter uses the r_{vertex} given by the primary fitter to compute T_0 according to the equation 4.2

$$T_0 = \frac{\sum_i \left(T_i^{pmt} - TOF_i^{pmt}\right) \times Q_i}{\sum_i Q_i} - const. \tag{4.2}$$

This T_0 is the charge weighted sum of T_emit from 4.1. This T_0 serves as the universal start point of an event. From this time, each PMT hit time is

$$\tau(x, y, z, T_0) = T_i^{pomt} - TOF_i^{pmt} - T_0 \tag{4.3}$$

Finally, these time-of-flight corrected and centered hit time distributions are used to create probability distributions for the 17 and 20 inch PMTs respectively. These PDFs are shown in Figure 4·5. The likelihood function for an individual PMT is

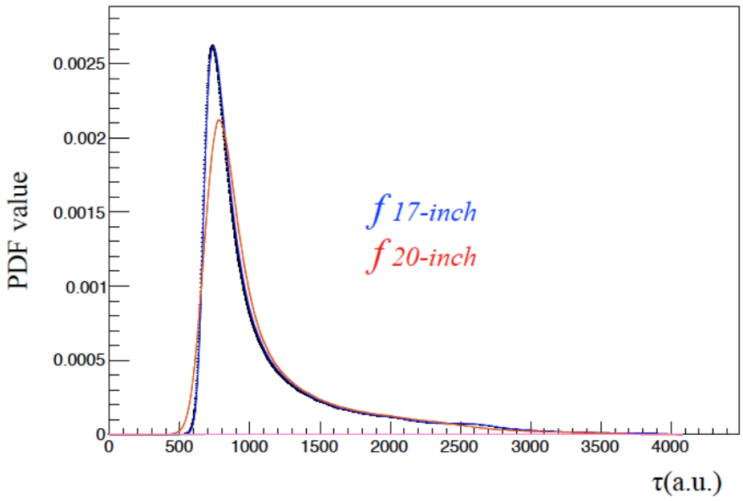

Figure 4·5: Probability density function of 17-inch and 20-inch PMT hit times calculated from calibration data. The plot is from [1] and originally from a 2005 calibration dataset.

defined as:

$$\phi_i = \frac{\mu \times f_i(\tau_i) + D_i}{\mu \times C_{17/20} + D_i} \tag{4.4}$$

Here, μ is the pulse shape determination factor, D_i is the dark hit rate for the i^{th} PMT and $C_{17/20}$ is the normalization constant for the 17 or 20 inch PMTs. The overall log-likelihood is given by the $log(L) = \sum_i log(\phi_i)$. The log-likelihood is maximized by the Newton-Raphson method, in which the x, y, z, T_0 are adjusted to the best-fit values, giving us the V2 reconstructed vertex.

4.2.5 Energy Reconstruction

Likelihood maximization is also used to reconstruct the energy of an event. A likelihood PDF is constructed using the number of hits, charge, and hit timing.

N_{hit} PDF

The expectation of the number of photons hitting PMT i, μ_i, is a function of the visible energy and dark charge.

$$\mu_i = a_i(x, y, z) \times E_{vis} + d_i \tag{4.5}$$

Here, $a_i(x, y, z)$ is a coefficient that converts the event energy to the number of photons, which is calibrated with neutron events. It is determined by the PMT position x, y, z. d_i is the dark noise charge of PMT i, which is electronically measured. The probability that μ_i photons hit the ith PMT j times, k_{ij}, is ideally expressed by the Poisson distribution:

$$k_{ij} = \frac{(\mu_i)^j}{j!} e^{-\mu_i} \tag{4.6}$$

However, in KamLAND waveform analysis, the 1 p.e. detection efficiency is reduced by the 0.3 p.e. software charge threshold. This threshold is set to reduce the acceptance of dark noise but also decreases hit detection efficiency. As a result, the PMT hit probability is reduced to:

$$P_{hit} = 1 - v_i e^{-\mu_i} \tag{4.7}$$

Hit Charge PDF

A Gaussian distribution is assumed for the hit charge PDF of each PMT:

$$f_{i,j(q_i)} = \frac{1}{\sqrt{2\pi j\sigma^2}} exp(-\frac{(q_i - j)^2}{2j\sigma^2}) \tag{4.8}$$

q_i is the observed charge in p.e. units and σ is the charge resolution against 1 p.e. distribution.

Hit Time PDF

PMT hit timing factors into energy reconstruction by helping to discriminate hits unrelated to the physical event. The hit timing model is created using source calibration data.

$$P_{time,i} = \frac{\psi(t_i) a_i E_{vis} + d_i}{\mu_i} \tag{4.9}$$

The PDF is the sum of the signal hit distribution and the constant dark noise.

Energy Likelihood

The likelihood function to be maximized is constructed as

$$L = \prod_{Not\ hit\ PMTs} P_{no-hit,i} \prod_{Hit\ PMTs} \left[P_{hit,i} \left(\sum_{j=1}^{100} f_{i,j} \right) P_{time,i} \right] \tag{4.10}$$

The reconstructed energy is the one which maximizes this likelihood. The Newton-Raphson method is used to search for this energy. This process is implemented independently for the 17-inch PMTs and 20-inch PMTs, then the event energy is calculated with a weighting factor α:

$$E_{vis} = (1 - \alpha) E_{17inch} + \alpha E_{20inch} \tag{4.11}$$

The weighting factor $\alpha = 0.3$ was determined to maximize energy resolution.

Bad Channels in Energy Reconstruction

The increase in the number of low gain PMTs has lead to worsening energy resolution over time, as these PMTs are excluded from the typical energy reconstruction described above. In particular, some of the low gain PMTs still detect photons, but proper gain calibration is not possible. A method for utilizing the information from operational low gain PMTs was developed, and the basic strategy is as follows:

1. The change in gain causes the effect of the 0.3 p.e. threshold on hit probability to change. The no-hit probability was expanded as follows:

$$P'_{no-hit,i} = \left(1 + \epsilon_1\mu_i + \epsilon_2\frac{\mu_i^2}{2!} + \epsilon_3\frac{\mu_i^3}{3!}\right)e^{-\lambda\mu_i} \tag{4.12}$$

   This model was originally a simple expansion of P_{no-hit}, but in the end was adjusted phenomologically to better reproduce real data. This adjustment is why an additional $e^{-\lambda\mu}$ appears in the model.

2. The parameters $\epsilon_1, \epsilon_2, \epsilon_3$, and λ are estimated with actual data. The events satisfying the following selections are collected and the no-hit probability is calcualted for each expected charge. The expected charge of the i-th PMT μ_i is estimated using the vertex and total charge of the events that meet the following conditions.

   - $r < 6m$
   - Not muons or events within 2 ms after muons
   - Events with more than 120 17-inch PMT hits
   - PMT waveforms that contain only 1 peak

   Figure 4·6 shows the result of fitting this adjusted no-hit probability model. THe fitting is performed run-by-run and for each PMT independently.

3. Use the updated no-hit probability pdf in the event energy reconstruction in Equation 4.10.

Making use of the low-gain PMTs can improve energy resolution by up to 3% [54]. Further analysis in this work uses energy reconstructed from the combination of normal and low-gain PMTs.

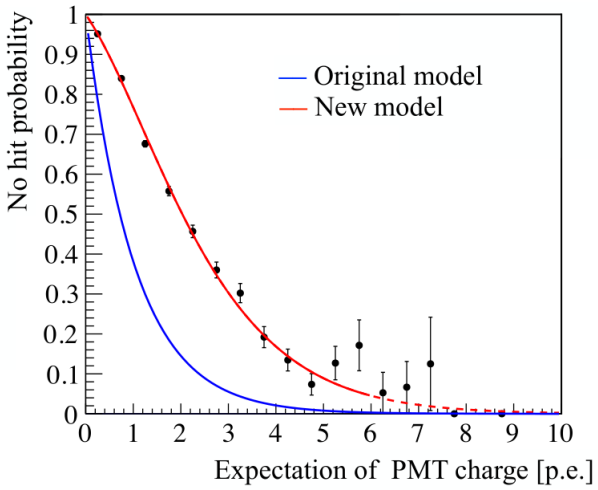

Figure 4·6: Fitting no hit probability to a low gain PMT against the expected charge μ. The original model is shown with the blue line while the red line is the new model which agrees better with low-gain PMT data.

4.2.6 Muon Reconstruction

The selection and understanding of muons and muon-correlated neutrons are essential to multiple background rejections. This section describes the special selection criteria and reconstruction methods used for muons and neutrons.

Muon Selection Criteria

The muon event selection criteria are as follows:

- Total charge of 17-inch PMTs, $Q_{17} \geq 10000$ p.e.
- $Q_{17} \geq 500$ p.e. and the number of hit OD PMTs ≥ 9.

The former criterion selects muons which go through the scintillator volumes of the detector. A total charge of 10,000 p.e. roughly corresponds to an event energy of 30 MeV, which exceeds the energy range of most physical analyses in KamLAND-ZEN. The second selection is for muons that only deposit energy in the outer buffer oil (clipping muons). Muons passing through the buffer oil volumes do not scintillate; as

such, the 500 p.e. threshold in Cherenkov radiation roughly corresponds to about 40 MeV of energy deposition.

Cosmic Ray Muon Reconstruction

Cosmic ray muon events form tracks as opposed to the point-like events caused by single decay events. The process is shown diagramattically in Figure **??**

1. The ID PMT which detects the earliest light is identified. If the charge of this hit is low or isolated in time from the many other hits in the event, it is classed as a dark hit and ignored. A line is drawn from the earliest hit muon PMT and the center of the KamLAND detector. The intersection of this line and the outer balloon is marked as the temporary entrance point.

2. The PMT whose charge is the largest is identified. The brightest hit PMT should be hit later than the earliest PMT and the neighbors of the earliest PMTs. A line is drawn from the brightest hit PMT and the center of the KamLAND detector. The intersection of this line and the outer balloon is marked as the temporary exit.

3. The temporary track is defined as the line connecting the temporary entrance and exit. The temporary track is finally corrected by checking the correlation between the track length and the total charge.

4. The reconstruction quality is evaluated by checking the following:

   - Whether the earliest and the brightest PMTs can be identified
   - Whether the mean hit time of PMTs around the entrance is earlier than the around the exit.

   A "badness" parameter value is assigned to the reconstruction according to this evaluation. With this evaluation, around 15% of muon candidates are

regarded as badly reconstructed though they can still be used in muon-neutron pairing. Bad muon reconstruction is caused by ringing in the PMT signals, muon bundles, and stopped muons.

The light yields in the muon events are estimated in [54]:

$$\langle dQ_C/dX \rangle = 28 \pm 5 \textbf{p.e./cm (Cherenkov muons)} \tag{4.13}$$

$$\langle dQ_S/dX \rangle = 338 \pm 12 \textbf{p.e./cm (Scintillation muons)} \tag{4.14}$$

4.2.7 MoGURA Neutron Reconstruction

Neutrons that are produced during cosmic ray spallation are best detected with the MoGURA DAQ due to the FBE's inability to handle the high after-pulse rate. After-pulsing is also present in MoGURA and needs to be rejected. An effective number of hits N_s was introduced. The neutron reconstruction procedure is as follows:

1. A 200 ns wide time window is opened. The vertex is reconstructed using LT Vertex with the hit information contained in this window.

2. The times of flight to each PMT are calculated assuming the reconstructed vertex. Then the ToF-subtracted hit timing distribution is obtained.

3. The obtained residual hit time distribution includes neutron capture 2.2 MeV gamma scintillation light and fake signals from after-pulses. To calculate the effective number of hits, N_{in} and N_{out}, the number of hits in a 30 ns wide "ontime" window and a 170 ns wide "offtime" window respectively are counted. N_s is then calculated as

$$N_s = N_{in} - N_{out} \times \frac{30\,\text{ns}}{170\,\text{ns}} \tag{4.15}$$

4. The ontime window is shifted by 20 ns, the clock time of MoGDAQ, and step 3 is repeated.

5. The 200 ns time window is shifted and steps 1-4 are repeated. The 200 ns window and 30 ns ontime window that maximize N_s are found. The vertex given by the N_s-maximizing time windows is taken as the reconstructed neutron capture event vertex.

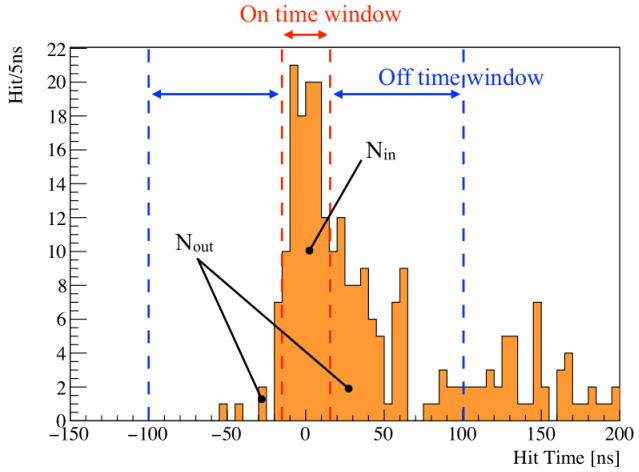

Figure 4·7: A neutron capture events hit times showing the contribution of fake after pulses and the time windows used to calculate N_s

4.2.8 Muon Neutron Correlation

The neutron selection process outlined above contains many noise events, thus the sample is only used in background discrimination when coincident with muons. In particular, MoGURA data neutrons are used to improve the rejection of xenon spallation products. The procedure for selecting muon-neutron pairs is:

1. Check the end unixtime of the previous KamDAQ run and the start unixtime of the current KamDAQ run.

2. Collect the MoGURA runs that collected data during this gap. Muon events collected by MoGURA are used in the gaps between KamDAQ runs; during KamDAQ runs, muons collected with FBE data are used.

3. The delayed coincidence analysis is done to select neutron candidate events in a short time period after muons. The first cuts applied are on $dT > 2500\mu$ and $N_s = N_{in} - N_{out} < 100$, these events are first removed. The subsequent MoGURA neutron selection criteria are outlined below.

The neutron selection in MoGURA is outlined in Figure 4·8. Two quantities are used, dT, the time delay between the neutron event and the previous muon, and N_s. From the 2D distribution, one sees that the event rate is higher in the short dT region due to noise and after-pulses. The N_s values also tend to be small due to signal loss caused by baseline overshoot in the PMTs. The following criteria were chosen to select MoGURA neutrons:

- $N_{total} = N_{in} + N_{out} > 150$ (Number of hit requirement)
- $N_s > 50 \wedge 10 < dT < 1200\mu s$ (reject after-pulses and accidental events)
- $!((N_s < dT(\mu s) + 70 \wedge 10 < dT < 20\mu s)||N_s < -0.8 \times dT(\mu s) + 106 \wedge 20 < dT < 70\mu s)$

Figure 4·9 shows the dT distribution of the MoGURA neutrons collected with the above criteria. The histogram is fitted to an exponential between 500 and 1000 μs, and the fitted function is extrapolated to the rest of the data range. The inefficiency of the neutron tag in the shorter dT period can be seen as the distribution turns off at low dT.

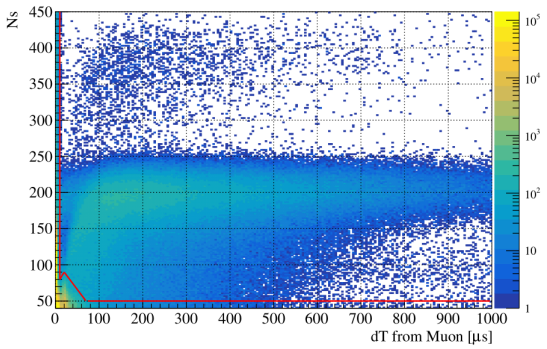

Figure 4·8: distribution showing the dT dependence of N_s. The events above the red line are selected as MoGURA neutrons and used for background rejection [17]

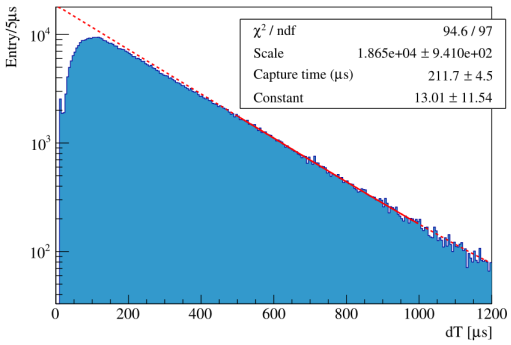

Figure 4·9: The dT distribution of selected MoGURA neutrons. The fit to an exponential is performed between 500 and 1000 μs. [17]

4.3 Event Selection

Candidate $0\nu\beta\beta$ events must pass several event selections. The selections are separated into non-physical events and background cuts. In this section, we first describe the event selections used in this analysis. Then, the impact of these selections on signal inefficiency is discussed.

4.3.1 Unphysical and Bad Quality Event Rejection

Much of the data saved in the KamLAND DAQ systems includes "unphysical" events. Furthermore, many of the events associated with real physical processes are of poor quality. This section describes the criteria by which unphysical events and poor quality events are selected.

1. Flasher PMT

   PMTs can occasionally emit light into the detector. These occurrences are called PMT flashers. There are multiple potential causes for a PMT to flash, such as the discharge of the dynodes and light emission from the epoxy around the breeder circuit. Figure 4·10 shows the typical event display of a flasher event. Such events have a distinct signature, as the PMT that flashes will have

exceptionally high charge and cause a huge deposition of charge in the nearest PMTs as well. The PMT flasher selection criteria are as follows:

- Total charge of ID PMTs $>$ 2500 p.e.
- Maximum ID PMT charge/Total ID PMT Charge $>$ 60%
- Average charge of the neighboring PMTs $>$ 20 p.e.

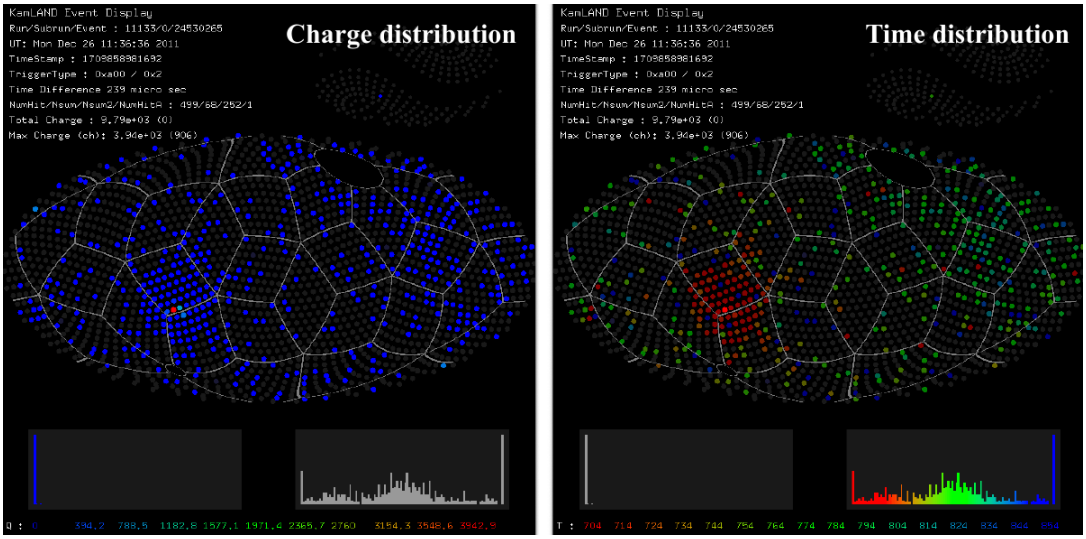

Figure 4·10: Event display of a flasher event. The left shows the charge distribution. One PMT has an exceptionally large charge. Right shows the time distribution. It is relatively flat since the source is not scintillator. The hit timing of the flasher PMTs and its neighbors are very early.

2. Post muon events

   Cosmic ray muons deposit a large amount of energy into the detector. As a result, the detector behavior is unstable for a period afterwards. In particular, the detector suffers from a high fake event rate due to after-pulsing and the shift of baseline from overshoot. This instability causes not only a large amount of unphysical events, but also degrades the reconstructibility of real physical events. Thus, all events in the immediate 2 ms after cosmic ray muons are not

used for the excited state analysis. However, these events may be used for other analyses such as spallation background estimation.

3. Missing waveform events

   High rate after-pulsing from cosmic ray muons can also cause the ATWD to be busy and the DAQ system to get stuck. When the DAQ electronics are in this state, event waveforms cannot be recorded. These are referred to as "missing waveform" events. In these situations, the number of hit 17-inch PMTs within 125 ns after a trigger issue is recorded as "NsumMax". In properly recorded events, NsumMax should be proportional to the total number of 17-inch PMT hits (Nhit17). So the missing waveform events are identified by the ratio between NsumMax and Nhit17; the distributions of these two quantities are shown in Figure 4·11. Events tagged by this selection are removed from the excited state physics analysis. The exact selection criteria are as follows:

   - Nhit17 $<$ NsumMax $\times 0.99 - 25$
   - dT after muon events $<$ 2 ms (if NsumMax$<$1200)
   - dT after muon events $<$ 2 s (if NsumMax$>$1200)

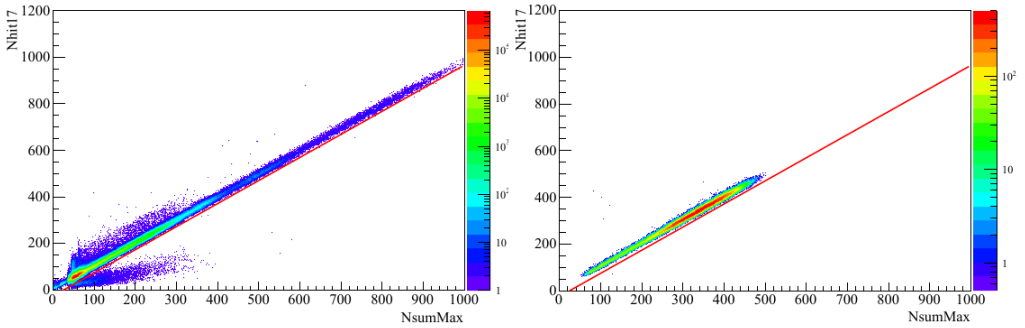

Figure 4·11: Nhit17 vs NHitSumMax distributions for all physics events (left) and Bi214-tagged events (right). The missing waveform cut inefficiency can be calculate from the Bi214-tagged events to be $< 0.01\%$

.

4. Post PPS trigger event

   The PPS trigger is a forced trigger issued once a second used for constant diagnostic monitoring of the detector. However, the PPS trigger has been found to cause an increase in electronics noise and DAQ trigger rate. Thus, events within 100 μs from the last PPS trigger are removed from the analysis.

5. Badly reconstructed events

   The fit quality of an event's vertex reconstruction is the event's "Badness". The quantity is calculated using nine parameters that describe the deviation of an event's PMT hit and charge distribution from the expectation. A detailed explanation of the Badness calculation can be found in section 3.8.3 of [**?**]. These poorly reconstructed events mostly consist of noise events and pileup. The events with large Badness are removed from the analysis by the following energy-dependent threshold:

$$Badness < 25.0 \times \exp(-4.5 \times E_{vis}[\text{MeV}]) + 3.1 \tag{4.16}$$

   Figure 4·12 shows the Badness distribution of all physical events and the Badness of ^{214}Bi events selected by the delayed coincidence method.

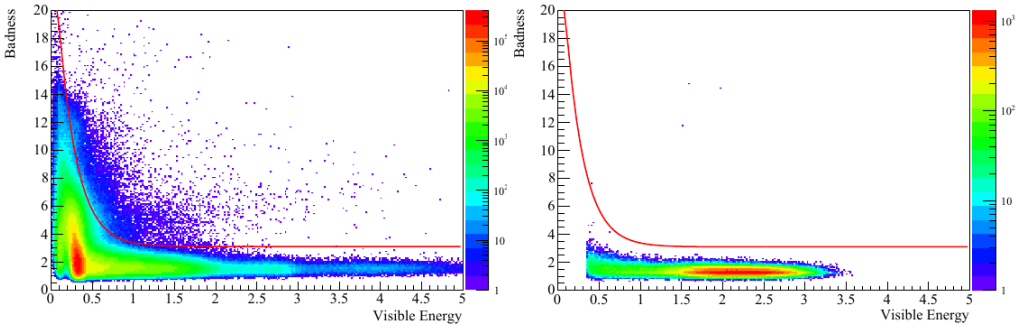

Figure 4·12: The badness distributions of all physics events (left) and Bi214-tagged events (right)

4.4 Background Rejection

4.4.1 Uranium/Thorium

^{214}Bi and ^{212}Bi are radioactive nuclei produced in the uranium and thorium decay series, respectively. They are among the dominant backgrounds in KamLAND-ZEN. These isotopes are introduced to the detector primarily by Uranium/Thorium contamination in the LS itself or on the surface of the inner balloon. There were also some ^{222}Rn introduced when the XeLS was filled, this decayed with a half-life of 3.8 days, as such the ^{222}Rn-related ^{214}Bi decayed away in the early stages of KamLAND-ZEN 800. This time-dependence of the Radon background is accounted for in the physics analysis. These Bismuth-decays are tagged in two ways: Delayed-coincidence veto and Double-pulse fitting.

Delayed Coincidence Veto

Both ^{214}Bi and ^{212}Bi decays are quickly followed by the decays of ^{214}Po/^{212}Po:

$$^{214}\mathrm{Bi} \xrightarrow[19.9\,\mathrm{min},\ 99.98\%]{\beta^-,\ Q=3.27\,\mathrm{MeV}} {}^{214}\mathrm{Po} \xrightarrow[164.3\,\mu\mathrm{s}]{\alpha,\ Q=7.83\,\mathrm{MeV}} {}^{210}\mathrm{Pb} \tag{4.17}$$

$$^{212}\mathrm{Bi} \xrightarrow[60.55\,\mathrm{min},\ 99.98\%]{\beta^-,\ Q=2.25\,\mathrm{MeV}} {}^{212}\mathrm{Po} \xrightarrow[0.299\,\mu\mathrm{s}]{\alpha,\ Q=8.95\,\mathrm{MeV}} {}^{208}\mathrm{Pb} \tag{4.18}$$

These decays are correlated in space and time in KamLAND, they can be vetoed by searching for this correlation. The criteria of the Bi-Po delayed coincidence analysis used in the KamLAND-ZEN analysis is as follows:

- delayed energy : $0.2 < E_d < 1.3$ MeV
- distance between prompt and delayed vertices : $dR < 170$ cm
- timing delay between prompt and delayed vertices : $dT < 1.9$msec

Figure 4·13 shows the delayed-coincidence veto parameter distributions used in the ^{214}Bi selection. Coincident pairs within 10 μsec are excluded and set aside for the ^{212}Bi selection, as ^{212}Po has a much shorter half-life. The delayed energy deposition distribution, two peaks are found. THe lower energy peak corresponds to polonium decays in which some energy is deposited not in the liquid scintillator but in the mini-balloon nylon film. Figure 4·14 shows the delayed-coincidence veto parameter

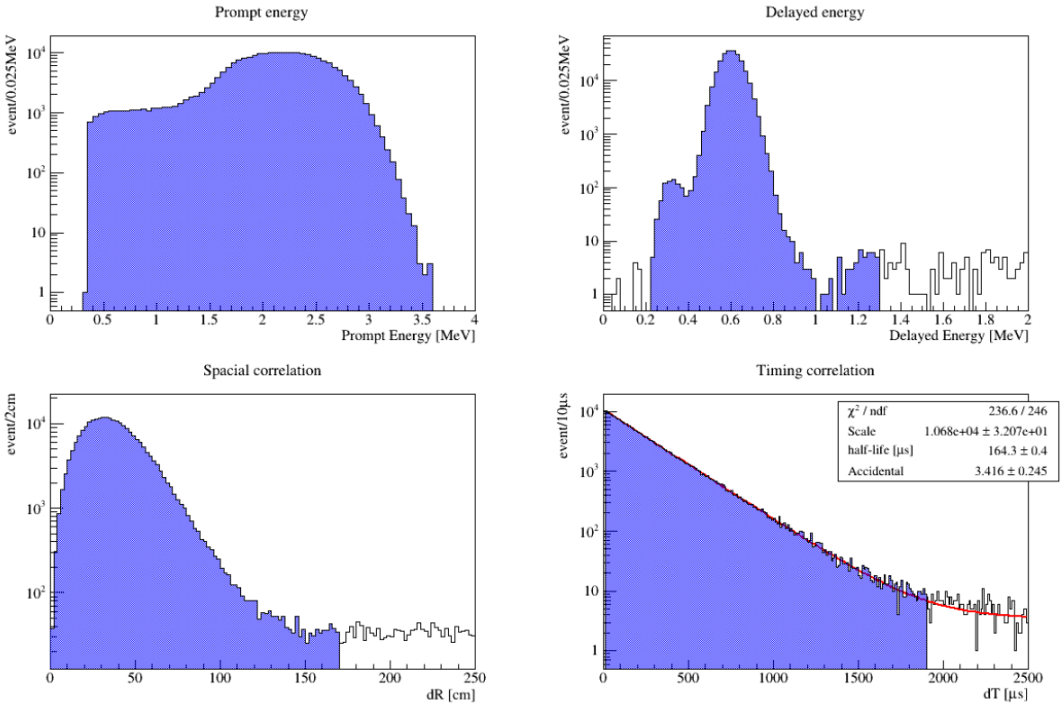

Figure 4·13: The delayed coincidence selection parameters for ^{214}Bi. The distributions of prompt energy, delayed energy, displacement, and delay time are shown. The blue shaded regions indicate the tagged events. Events with $dT < 10\mu sec$ are set aside for ^{212}Bi-Po selection.

distributions used in the ^{212}Bi selection. For this selection, the timing selection is $dT < 10\mu sec$. The veto efficiency of ^{214}Bi-Po decays in the XeLS is $99.89 \pm 0.03\%$. The veto efficiency of ^{214}Bi-Po decays in the balloon film is $48.9 \pm 9\%$. The lower veto efficiency is due to alpha decays depositing their energy in the film not the liquid scintillator. For ^{212}Po decays that occur immediately after the initial ^{212}Bi decay,

they can be tagged by the double pulse fitter, which the next section describes.

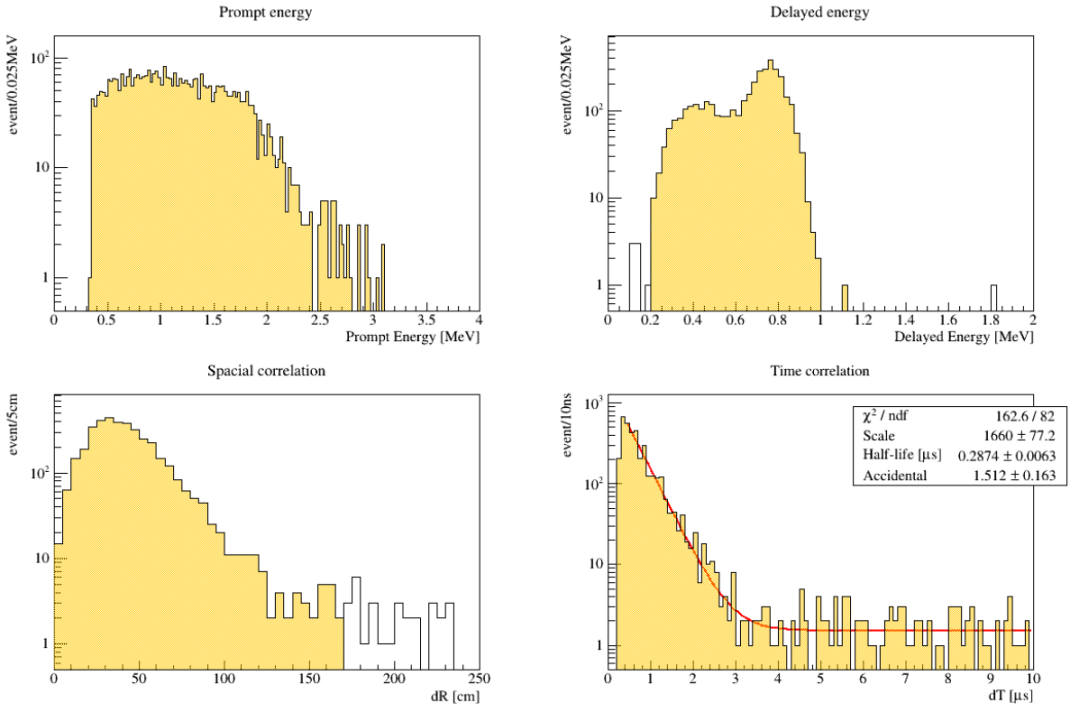

Figure 4·14: The delayed coincidence selection parameters for ^{212}Bi. The distributions of prompt energy, delayed energy, displacement, and delay time are shown. The yellow shaded regions indicate the tagged events. Only events with $dT < 10\mu sec$ are used for this selection.

Pileup Events

When the delay time, dT, between prompt and delayed events is small enough, Bi-Po sequential events can be stored as a single event in KamLAND's data acquisition window. In these cases, the delayed coincidence selection of two related events does not work. Such events are referred to as pile-up events. Since these pileup events contain the kinetic energy of the initial beta decay and the subsequent alpha decay, the combined deposited energy reaches beyond the $0\nu\beta\beta$ ROI and becomes an important background to reduce. The energy spectrum of these ^{212}Bi-Po pile-up events is shown in Figure **??**.

A double pulse fit method has been developed to tag these pile-up events. The method simply searches for events with a hit-timing distribution indicative of two distinct energy depositions, or hit time peaks. The hit time distribution of an event is fitted with 2 reference waveforms by the following procedure:

1. Construct a reference time profile. A reference waveform is made from the hit time profile of $2\nu\beta\beta$-decay candidates. The events are selected with $1.4 < E_{vis} < 1.6$ MeV and $radius < 157$ cm after $0\nu\beta\beta$ background vetoes.

2. Construct the hit timing profile of $0\nu\beta\beta$ decay candidates. The hit timing profile of the candidate events (events to be analyzed) is constructed. In the typical analyses and reconstructions, the time of the first hit on a PMT in an event is used. For this procedure, all hit times and hit charges (multi-hit) information is used to effectively separate the two peaks.

3. Fit the event's hit time profile The hit time profile is fitted by the reference waveform. The fit includes 4 parameters: E_p (prompt signal energy), T_p (prompt signal timing), E_d (delayed signal energy), ΔT (time delay between prompt and delayed signals). Then a maximum likelihood optimization is performed. χ^2 for the fit is defined as:

$$\chi^2 = \begin{cases} 2\sum_i \left\{ -(x_i - f_i) + x_i \log \frac{x_i}{f_i} \right\} & (n_i > 0) \\ 2\sum_i \{ -(x_i - f_i) \} & (n_i = 0) \end{cases} \qquad (5.27) \qquad (4.19)$$

where i, x_i, and f_i denote the i-th bin, the number of hit PMTs in the i-th bin and the expectation of the number of hits in the i-th bin, respectively. The time bins are 1 ns wide. f_i can be calculated as the sum of a dark rate D and the reference waveform $R(i)$ as:

$$F_i = |E_p| R(i - T_p) + |E_d| R(i - T_p - \Delta T) + D \qquad (4.20)$$

Here, the dark rate is a simple global dark rate taken from all the PMTs in the off-time period. The χ^2 minimization is performed with MINUIT in the ROOT analysis framework. For all the $(T_p, \Delta T)$ pairs, E_p and E_d are floated, and the optimal four parameters are found.

4. Correct the reconstructed energies E_p and E_d are used in the double-pulse fit to scale the reference waveform but they are not accurate individual pulse energy reconstructions. The energy reconstruction described in section 4.2.5 is more accurate. This "official" energy reconstruction is incorporated into the individual pulse energies by:

$$E_{p'} = E_{vis} \times \frac{E_p}{E_p + E_d} \tag{4.21}$$

$$E_{d'} = E_{vis} \times \frac{E_d}{E_p + E_d} \tag{4.22}$$

Thus, the double-pulse fit provides the fraction of the total event energy, E_{vis}, to assign to the prompt and delayed signals.

5. Candidate selection Finally, the pile-up tagged events are selected from the candidate events based on their ΔT and $E_{d'}$. The selection criteria are determined using MC simulated events while limiting the $0\nu\beta\beta$ inefficiency to about 0.1%. Figure 4·15 shows the selection criteria over the MC distributions. The remaining ^{212}Bi-Po events that pass pile-up are estimated to be $2.3 \pm 0.5\%$.

4.4.2 Antineutrinos

The original physics objective of the KamLAND experiment was to observe electron anti-neutrinos produced in nuclear reactors, among other sources. The signature of

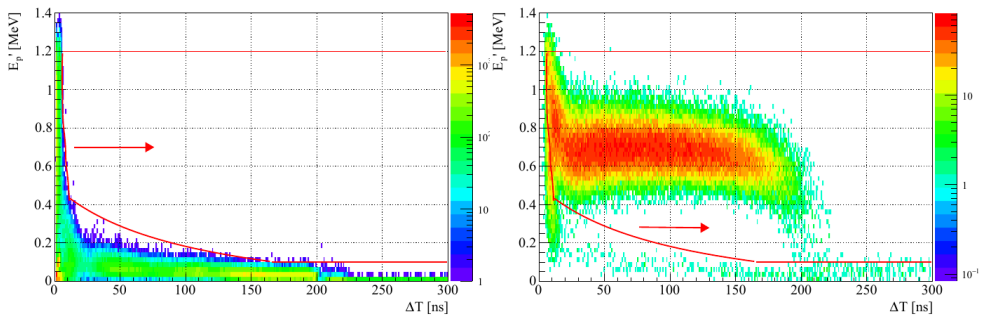

(a) $0\nu\beta\beta$ (b) ^{212}Bi–Po pile-up events

Figure 4·15: The selection criteria over E_d and ΔT used to tag pileup events. The distributions are of MC $0\nu\beta\beta$ (left) and ^{212}Bi-Po (right). The regions enclosed by the red lines are vetoed as pileup events.

anti-neutrinos in KamLAND and KamLAND-ZEN is inverse beta decay (IBD):

$$\bar{\nu}_e + p \rightarrow e^+ + n \tag{4.23}$$

IBD produces a neutron and a positron. The positron annihilates with an electron to produce gamma rays, 2×511 keV gammas. The neutron scatters in the detector until being captured by protons with an average capture time of $\tau = 207\,\mu$s. This two-stage signal is ideal for tagging with the delayed coincidence method.

In the anti-neutrino analysis, IBD events were originally selected by a likelihood ratio selection; but in KLZ, a simple box cut analysis is applied. The IBD selection criteria are:

- delayed energy : $E_d > 1.5$ MeV
- distance between prompt and delayed vertices : $dR < 200$ cm
- timing correlation between prompt and delayed vertices : $dT < 1.0$msec

In the wake of the 2011 Tohoku earthquake and reactor meltdown, the Japanese nuclear power plants were turned off and the rate of anti-neutrino events are less than 0.2 event/day within $r < 550$ cm. The efficiency of the IBD box cuts are

99.14%. Thus, the remaining potential IBD background to the KLZ analyses are negligible.

4.4.3 Short-lived Spallation Products

High energy cosmic ray muons can break apart nuclei in the detector material into lighter nuclei and produce secondary particles. The spallation products of ^{12}C are one of the dominant backgrounds in the $2n\beta\beta^*$ search. Multiple tagging methods have been developedfor identifying so-called short-lived spallation products.

^{12}B Veto

The ^{12}B β-decay has a large contribution to the background in the $0\nu\beta\beta$ ROI. The rate of muons is $\cong$ 3 Hz in the KamLAND detector thus ^{12}B can be removed with a veto after muons. In this analysis, a 150 msec window, corresponding to 5 times the livetime of ^{12}B, is vetoed and counted as detector deadtime.

MoGURA Neutron Veto

Neutrons are also ejected during the muon spallation process. These neutrons are correlated with the spallation products. The MoGURA DAQ system is used to observe neutron captures that occur shortly after cosmic-ray muons. The correlation with these MoGURA neutrons can be used to tag other short-lived spallation products, mainly ^{10}C, ^{6}He, and ^{8}Li. The selection of the MoGURA neutron veto is as follows:

- distance between candidate decay and spallation neutron : $dR < 160$ cm
- timing correlation : $dT < 180$ s (about 5 times the lifetime of ^{10}C)

^{137}Xe Veto

Neutrons capturing onto ^{136}Xe nuclei form ^{137}Xe. The Q-value of ^{137}Xe β^--decay is 4.2 MeV with a half-life of 3.82 minutes. This decay can be tagged by the triple

coincidence of a muon, the neutron capture, and the beta decay itself. The selection criteria is as follows:

- distance between candidate decay and spallation neutron : $dR < 160$ cm
- timing correlation : $dT < 1{,}620$ sec

Since the neutron capture gamma on ^{137}Xe has a gamma energy about 4 MeV, higher than captures on protons, the neutron selection criteria is adjusted slightly. The ^{137}Xe neutrons are required to have N_s values above 240. A schematic of spallation veto of Carbon and Xenon is shown in Figure 4·16.

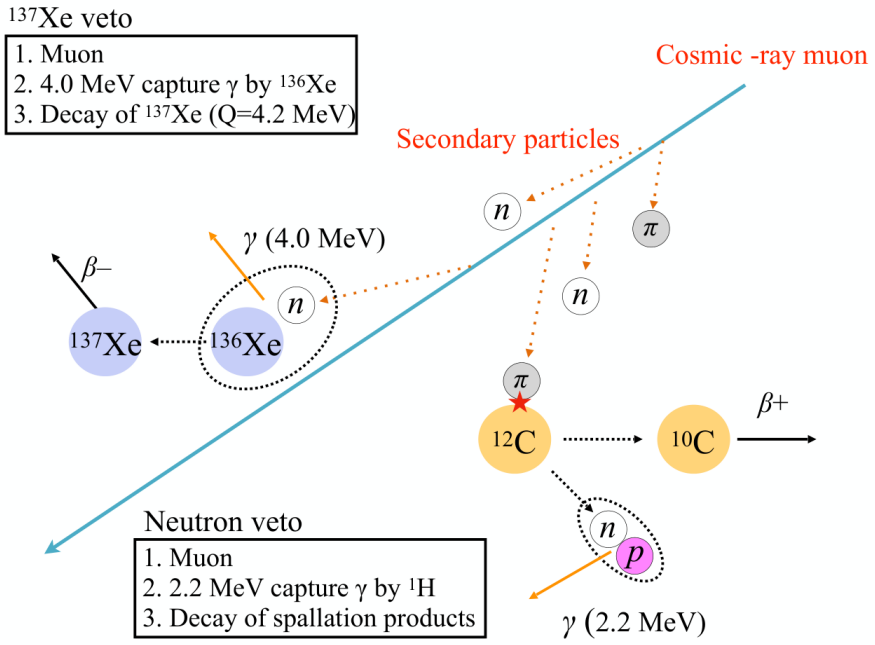

Figure 4·16: A schematic of spallation veto with MoGURA neutrons

4.4.4 Shower Veto

As a cosmic-ray muon passes through the detector, it does not interact with uniform probability along its path. There is a point where it deposits the most energy and

spallates the most nuclei. Secondary decay products are correlated with this position. The shower veto identifies this location of high energy deposition and correlates background with this position.

PDF$(dE/dX, dL)$

dE/dX, the distribution of energy deposition along muon tracks, and dL, the distance from the muon track to the candidate event, are correlated to the decay candidates. A two dimensional PDF$(dE/dX, dL)$ is constructed from muon data vy the following procedure:

1. The cosmic ray muons are selected and their tracks reconstructed.

2. The time when the muon entered the ID T_0 is calculated.

3. THe distance between the muon ID entrance and the generated point L is calculated for each photon. Figure 4·17 shows the schematic of photon generation from cosmic muons.

$$x_2^2 = r^2 + s_1^2 - 2x_1 r\cos\theta \tag{4.24}$$

$$x_1 + nx_2 = c(t - t_0) \tag{4.25}$$

Here, n is the refractive index of the liquid scintillator. These equations are solved for x_1, the distance L can be obtained. For general analysis and reconstruction, only the PMT hit times of the first photons are used. However, for this calculation, multiple photons for each PMT are considered, referred to as multiTQ analysis. L is calculated for each incident photon on each PMT.

^{12}B is used for estimating the PDF$(dE/dX, dL)$ as it can be easily tagged by the dT selection after muon events. Figure 4·18 shows an example of a dE/dX calculation result. The accidental event likelihood can also be calculated using the off-time events. The spallation backgrounds are rejected by calculating a likelihood

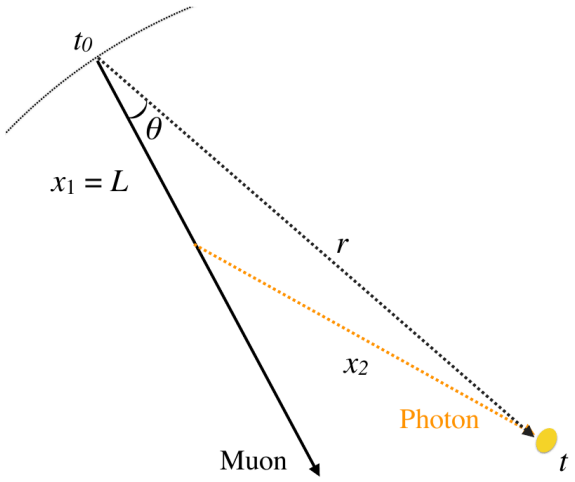

Figure 4·17: dE/dx reconstruction.

ratio value of spallation vs accidental. THe log-likelihood ratio threshold used is -1.8, events with spallation-accidental logarithmic ratios below this value are classified as spallation backgrounds and rejected.

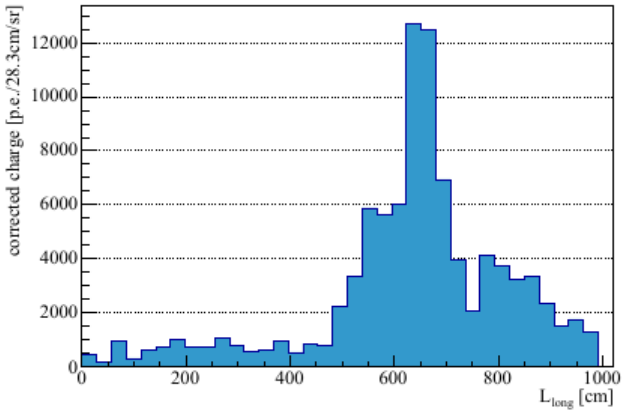

Figure 4·18: An example of a calculated dE/dx. The muon's largest energy deposit can be seen at $L_{long} = 600$ cm.

4.4.5 Xenon Spallation Products

The spallation products of Xenon are an important background to the $0\nu\beta\beta$ search. For the $2\nu\beta\beta^*$ search, they obscure the endpoint of the $2\nu\beta\beta$ spectrum. Rejecting

this background is important to both double-beta physics searches. However, these heavier nuclei can have half-lives of hours or longer, much longer than their Carbon-spallation counterparts; therefore, the MoGURA neutron veto is ineffective against these.

For these backgrounds, a likelihood selection has been developed specifically for these "long-lived" spallation products. The method involves constructing PDFs of dT (time since muon), dR (spatial distance from the nearest neutron created by each muon), and ENN (Effective Number of Neutrons).

^{136}Xe spallation is characterized by the production of many free neutrons; these post-muon neutron captures are useful in identifying likely long-lived spallation isotopes. However, there is a high rate of accidental neutrons and unphysical detector noise that can be attributed to neutrons. The ENN, Effective Number of Neutrons, was developed to define a weighted counting of neutrons by who likely they are to be related to a given event. Each neutron following a muon is assigned a weight based on the spatial distributions of neutron captures from spallation products and accidentals. Figure 4·19 shows the weight over dR.

$$ENN = \sum_{neutrons} \frac{PDF_{spl.}(dR)}{PDF_{spl.}(dR) + PDF_{acc.}(dR)} \tag{4.26}$$

The PDFs are the probability distributions of dR which is the spatial distance between a candidate event and a neutron event. Spallation products and neutrons that originate from the same muon have a spatial correlation. The PDFs are shown in Figure 4·19a. $PDF_{spl.}(dR)$ is modeled with an exponentially modified Gaussian distribution, while $PDF_{acc.}(dR)$ is simply quadratic, assuming uniform distribution in space of uncorrelated events. The exponentially modified Gaussian function features

3 free parameters:

$$f(x;\mu,\sigma,\lambda) = \frac{\lambda}{2} exp\left(\frac{\lambda}{2}(\mu + \lambda\sigma^2 - 2x)\right) erfc\left(\frac{\mu + \lambda\sigma^2 - x}{\sqrt{2}\sigma}\right) \tag{4.27}$$

$erfc(x)$ is the complementary error function defined as $erfc(x) = 1 - erf(x)$. The free parameters are determined using ^{10}C data. The sum in equation 4.26 is over all the neutrons in a short window after a muon, it is a quantity assigned to each muon.

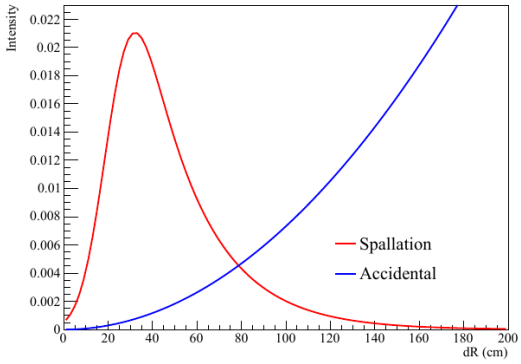

(a) dR distribution for neutrons associated with spallation products and accidental neutrons

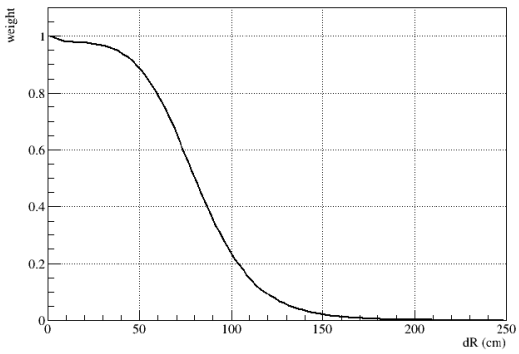

(b) Long-lived events

Figure 4·19: Weighting factor function for ENN.

Long-Lived Spallation Likelihood

Long-lived spallation backgrounds are handled not by rejecting them from the analysis outright, but by separating long-lived spallation candidates into a separate spectrum to be fitted alongside the residual events. The long-lived data (LD) and the singles data (SD) are separated by calculating a likelihood ratio threshold. The likelihood ratio is defined as:

$$R_L = \frac{L_{spl.}}{L_{acc.} + L_{spl.}} \tag{4.28}$$

where $L_{acc.}$ and $L_{spl.}$ are the likelihood functions of accidental events and long-lived spallation backgrounds.

The spallation product likelihood is constructed from:

$$L_{spl.}(dR_{near}, ENN, dT) = \sum_{spl.products} PDF(dT) \times PDF(dR_{near}, ENN) \qquad (4.29)$$

where the sum is calculated for all spallation isotopes listed in Table **??**. There is an implicit assumption that the time-component of the likelihood and the $PDF(dR, ENN)$ are independent. L_{acc} is assumed to be uniform in time and is defined as:

$$L_{acc.}(dR, ENN, dT) = PDF(dR, ENN) \qquad (4.30)$$

The likelihoods are constructed from FLUKA simulations and real muon data in KamLAND-ZEN. The long-lived likelihood uses FLUKA simulations of spallation product production and neutron ejection. The accidental likelihood uses events that occur after muons to get a data-informed dR and ENN distribution. Figure 4·20 shows the 2D profiles of the two likelihood functions. The differences are clear, in particular that the spallation products are more likely to have higher ENN and lower dR. In order to avoid dividing by a joint 0 likelihood in the likelihood ratio, bin-smoothing is done to both likelihoods to extend them into the full range.

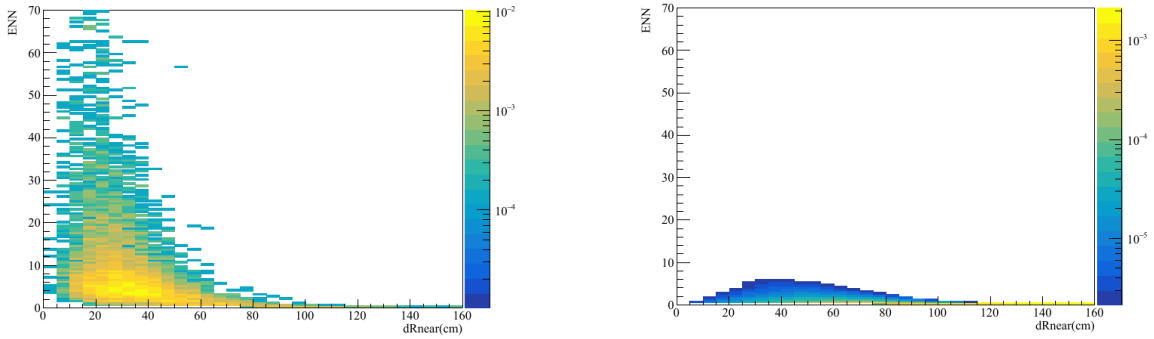

(a) Spallation Products **(b)** Accidental events

Figure 4·20: Weighting factor function for ENN.

Figure 4·21 shows the distributions of log-likelihood ratios, calculated from our PDFs from toy-MC trials. 10^6 events are generated for each PDF. The log-likelihood

ratio is $\log_{10}\left(1-\frac{L_{acc}}{L_{acc}+L_{spl}}\right)$, the logarithm is taken to bring all events into a similar range. With this definition, a smaller likelihood ratio or LHR means a higher likelihood of being a long-lived spallation product and a larger LHR indicates a higher likelihood of being an accidental event.

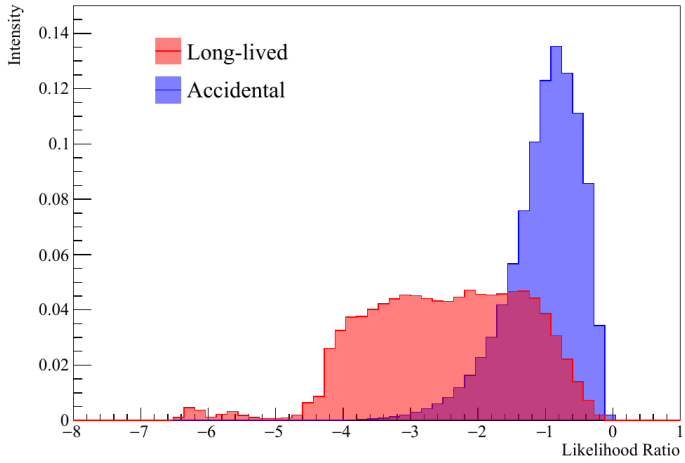

Figure 4·21: Log-Likelihood ratio distributions generated from the PDFs by a ToyMC study. A clear separation between the distributions can be seen.

Figure of Merit

To separate the data events into SD/LD datasets a threshold on the LHR variable must be determined. This threshold is determined by a Figure of Merit calculation (FOM).

$$\text{FOM} = \frac{S(t)}{\sqrt{s(t)+B(t)}} \tag{4.31}$$

$S(t)$ and $B(t)$ are the integrated LHR distributions above threshold, t, of signal and background generated by the toyMC study above. Due to inconsistent run conditions, including MoGURA livetime and efficiency, the datasets is separated into 3 time periods and a threshold is independently determined for each time period.

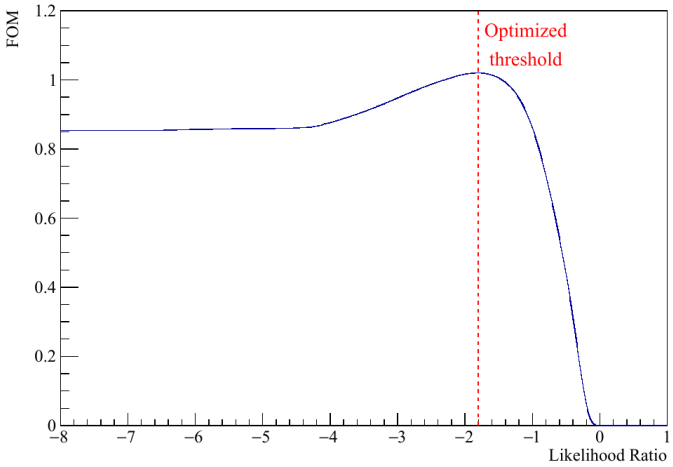

Figure 4·22: Long-lived spallation veto Figure of Merit

Veto Efficiency

The veto efficiency of the long-lived spallation veto is estimated for each spallation background in Table **??** using ToyMC informed by FLUKA simulations. FLUKA simulated isotope production and neutron correlation is convolved with our measured KamLAND-ZEN energy and vertex resolution. The tagging procedure using the above PDFs and likelihood ratio is applied to estimate the veto efficiency.

Furthermore, some of the other background rejection methods will simultaneously help reject some of the long-lived spallation backgrounds. Namely, the pileup veto and MoGURA neutron veto reject some spallation backgrounds; the effects of those vetoes are described as:

- Pileup veto: The double pulse fitter for pileup veto is sensitive to the o-Ps (ortho-positronium decays) of β^+ decaying isotopes. The efficiency of the double-pulse fitter is estimated for each isotope using the lifetime and production rate of o-Ps in [55]. Averaging over the isotopes weighted by production, the efficiency is 4.01%.

- MoGURA neutron veto: Long-lived spallation products that happen to decay

in the 160 s time window of the MoGURA neutron veto are tagged. FLUKA and GEANT4 simulations inform an averaged efficiency of 6.6%.

Uncertainties

Table 4.1 lists the estimated systeamtic errors of the FLUKA simulation of long-lived spallation isotope production. The most significant of these systematic errors is the uncertainty in the FLUKA spallation simulation.

	Error
Time-bin dependence	2.9%
Neutron detection efficiency	2.73%
Comparison between FLUKA and beam experiments	7.5%
Energy resolution of MoGURA	5.67%

Table 4.1: Errors of FLUKA

4.4.6 Signal Inefficiency

The effect of all these background vetoes on the $0\nu\beta\beta$ signal needs to be understood. This signal inefficiency is determined by calculating the livetime of the analysis.

The livetime calculation is done by applying the same event selections to toy MC events distributed uniformly in time and space. Real detector data is used for the Muon-neutron pairs, delayed coincidence analysis, 1PPS trigger event, and missing waveform events. Livetime is the fraction of runtime leftover after event selection.

$$\text{Livetime} = \frac{\#\text{ of Toy MC events after event selection}}{\#\text{ of generated Toy MC events}} \times \text{Runtime} \tag{4.32}$$

The $2\nu\beta\beta^*$ spectral fit is performed over long-lived spallation enriched and depleted events simultaneously. A later section describes this selection. For proper relative normalization, the livetime is calculated for both long-lived enriched and depleted samples. The deadtime of the KLZ physics analysis is listed in Table 4.2.

Table 4.2: Summary of the deadtime

Event selection	**Deadtime ratio** [%]
Spallation veto	14.64
MoGURA neutron veto	4.91
^{8}Xe veto	1.33
Shower veto	7.37
^{12}B veto	3.11
Xe spallation veto	8.56
Detector deadtime veto (post PPS, after muons and missing waveforms)	9.47
Hardware related	0.0078
Delayed coincidence Ra veto	0.0013
Delayed coincidence Reactor veto	0.0010
Total	**29.52**

The signal inefficiency of the double-pulse fitter and vertex Badness are omitted from Table 4.2. This is due to the Toy MC livetime study not being done at the PMT hit level. Sections 4.4.1 & 4.3.1 show that the signal inefficiency from these selections is negligible.

The signal inefficiency of the double-pulse fitter and vertex Badness are omitted from table 4.2. This is due to the Toy MC livetime study not being done at the PMT hit level. Sections 4.4.1 & 4.3.1 show that the signal inefficiency from these selections are negligible.

Chapter 5

Detector Calibration and MC Tuning

Accurate modeling of physics events and detector response are essential for correct interpretations of KamLAND-ZEN experimental data. This chapter outlines the detector calibration and Monte-Carlo (MC) tuning methods used. Since the commissioning of KamLAND-ZEN 800, no deployed laser or radioactive source calibration was done. This was to avoid any radioactive contamination from inserting these components into the detector. Thus, known backgrounds are the primary tools for detector calibration. [15]

5.1 Detector Calibration

The KamLAND detector has taken data for over 20 years. The energy scale, nonlinearity, bias, resolution, and vertex bias and resolutions have been well calibrated and studied. However, it is important to understand the variation of the detector performance over time. Electronics issues, such as HV reduction, channel loss, and detector work can affect our reconstructions.

5.1.1 Variation of Energy Scale Over Time

As PMT channels are lost or deteriorate into bad channels, or have their gains adjusted, the energy scale of the detector can vary over time. Variation from the beginning of the analysis period in 2019 and until the end of KLZ-800 data-taking in 2024, the energy scale varied by 3%.

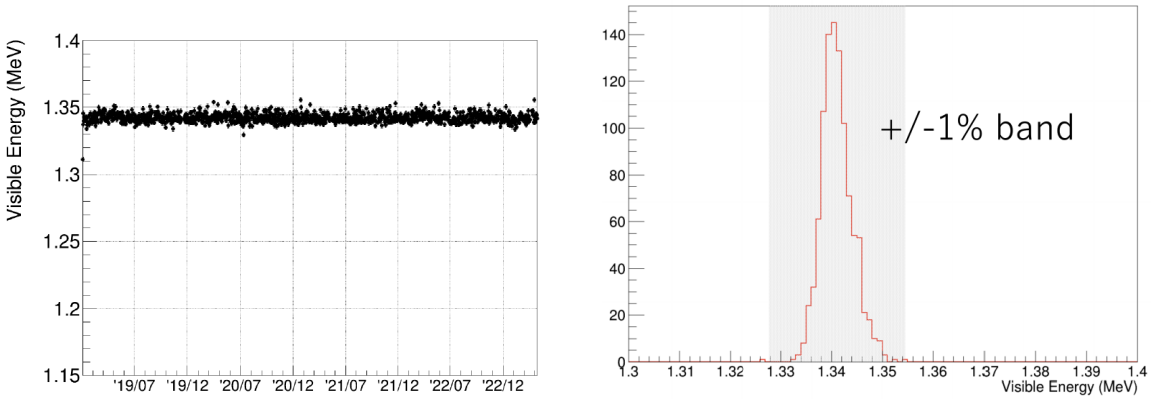

(a) Time variation **(b)** Histogram among runs (%) axis

Figure 5·1: Time variation of ^{40}K peak after correction. (A) Time variation of energy scale is corrected using ^{40}K and this figure is a check using ^{40}K itself. (B) Fluctuations among runs are within 1% (gray band).

^{40}K PEEK Gammas

Reconstructing the ^{40}K-γ peak from balloon PEEK material can help calibrate the energy scale over time. The PEEK material is located 550cm above the center of the detector and is a consistent source of ^{40}K radioactive decays. The decay energy of the ^{40}K electron-capture decay to ^{40}Ar has an energy of $Q_{EC} = 1504$ keV. However, as the energy scale of the detector decreases as you move from the center of the detector. This EC-γ peak is observed at around $E_{vis} = 1.35$ MeV in KamLAND-ZEN. These ^{40}K PEEK events are selected by the following simple selection:

- Passes Flasher Veto
- Passes Muon Veto
- Passes 2msec veto after muons
- cylindrical volume selection around PEEK material ($450 < z < 600$,$\rho < 250$ cm)

Neutron Capture Gammas

The KamLAND energy scale is primarily set by neutron captures on Hydrogen. Figure 5·2 shows the variation in neutron capture visible energy over time in XeLS and KamLS. Events are taken simply in a time window following muons. Due to post-muon instability, such as high after-pulsing, PMT ringing, and baseline shifts, the time directly after muons is excluded. An on-off time analysis is performed to subtract any incidental backgrounds and resolve the neutron capture energy distribution.

- On-time window : $400 < dT < 1500 \mu sec$
- Off-time window : $2800 < dT < 4000 \mu sec$

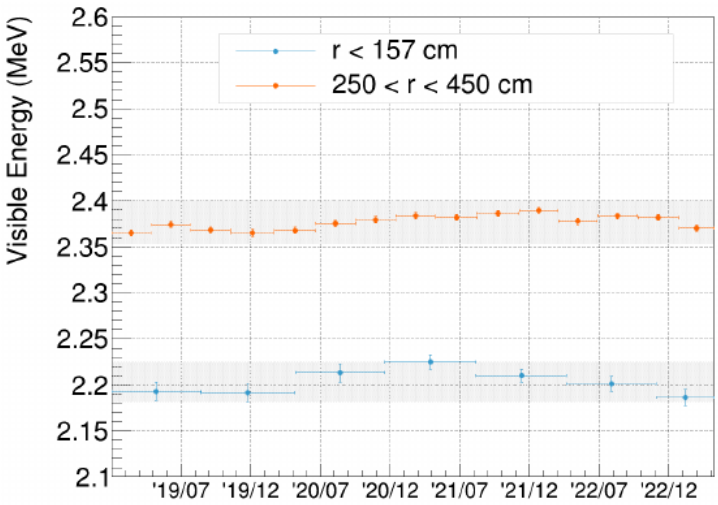

Figure 5·2: Neutron capture energy over KLZ-800 data-taking. The blue and orange points correspond to XeLS and KamLS respectively. Gray bands show ±1% deviation from the average. Note that the energy scale is 7% higher in KamLS due to the higher scintillator light-yield.

$2\nu\beta\beta$ Rate

The tail of the $2\nu\beta\beta$ decay spectrum is another useful handle on variations in energy scale over time. In the abscence of any XeLS leakage out of the inner balloon, the rate

of $2\nu\beta\beta$ events in an energy range can be used to verify the energy scale. We apply all the $0\nu\beta\beta$ analysis event selections and a further $1.85 < E_{vis} < 2.35$ MeV energy selection to select the $2\nu\beta\beta$-dominant region. Figure 5·3 shows minor fluctuations, but no clear trend upward or downwards.

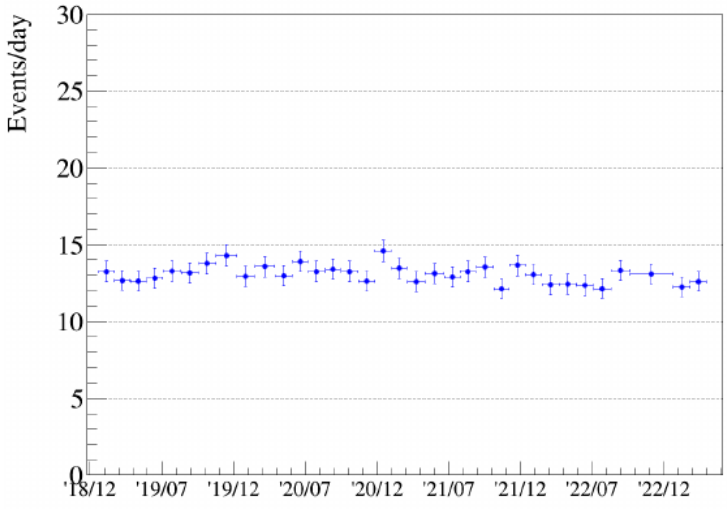

Figure 5·3: The event rate in the $2\nu\beta\beta$ dominant energy region over KLZ-800 data-taking.

5.1.2 MoGURA Stability

Cosmic ray muon induced spallation reactions are a constant source of well understood background. MoGURA's dead-time-free electronics allow it to observe neutron capture's closer in time to the original muons. This higher tagging efficiency than KAMFEE provides more data that can be used for calibration.

The MoGURA stability performance over time is marked by the neutron capture rate and distributions. Figure 5·2 shows the variation over time of MoGURA's neutron tagging performance. The neutron selection in MoGURA was outline in section 4.2.7.

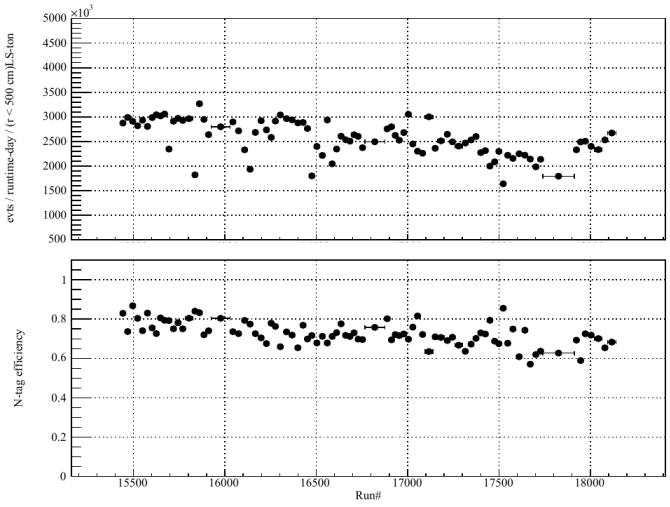

Figure 5·4: MoGURA's neutron capture rate and neutron tagging efficiency over KLZ-800 data-taking.

^{10}C tagging Stability

^{10}C is an easily isolated, well-understood background that can be further used to monitor detector stability. ^{10}C tagging via triple coincidence was described in section 4.4.3. Note that for this study, the ^{10}C selection was adjusted from the $0\nu\beta\beta$ analysis for higher signal purity.

- Select events in KamLS volume ($250 < r < 400cm$) and veto the corrugateed tube ($r > 250cm \& z > 0$)
- $2.0 < E_{vis} < 5.0$ MeV
- On-time window: $10 < dT < 90$ sec
- Off-time window: $300 < dT < 1000$ sec

The on-time window begins at 10 seconds to exclude the ^{6}He spallation background with a 1.16 second lifetime and $Q_\beta = 3.5$ MeV. Figure 5·5 shows the characteristic distributions that identify the dataset as ^{10}C. The rate is estimated by fitting an exponential plus constant background to the dT distribution. The dR, distance to

nearest neutron, distribution is modeled by an *exGaussian*, exponentially modified Gaussian. The variation in ^{10}C rate and mean of the exGaussian function are shown in Figure 5·6

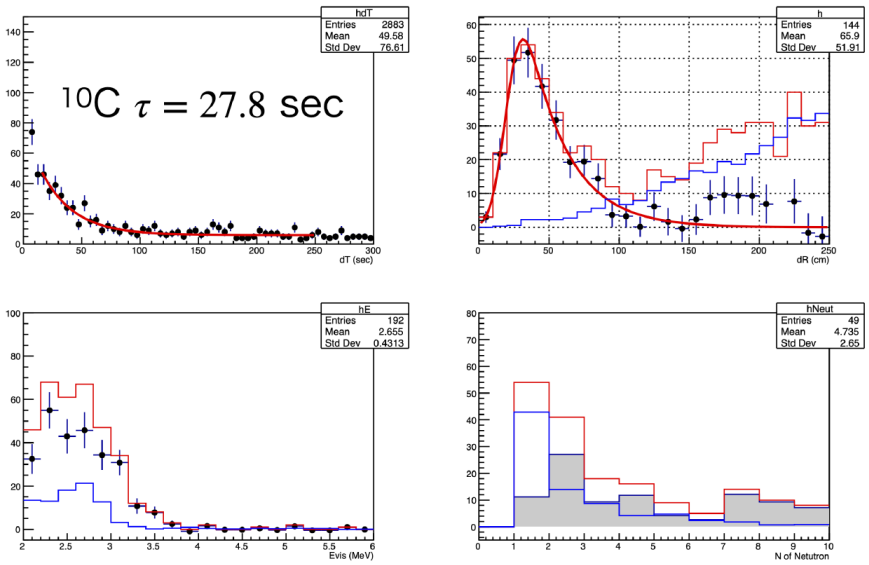

Figure 5·5: Characteristic distributions of ^{10}C decays. Red and blue histograms show on-time and off-time events respectively, and the black markers or grey histograms show the subtracted distributions (on-time - off-time).

5.2 MC Tuning

KamLAND physics simulation is built on two simulation tools: GEANT4 and FLUKA. GEANT4 is used to simulate the distributions of signals, backgrounds decays, and scintillation light propagation in KamLAND detector media. KamLAND's GEANT4-based simulation tool chain is called KLG4Sim. FLUKA is used to simulate cosmic-ray muon induced spallation. Namely for neutron multiplicity and topology and spallation isotope production.

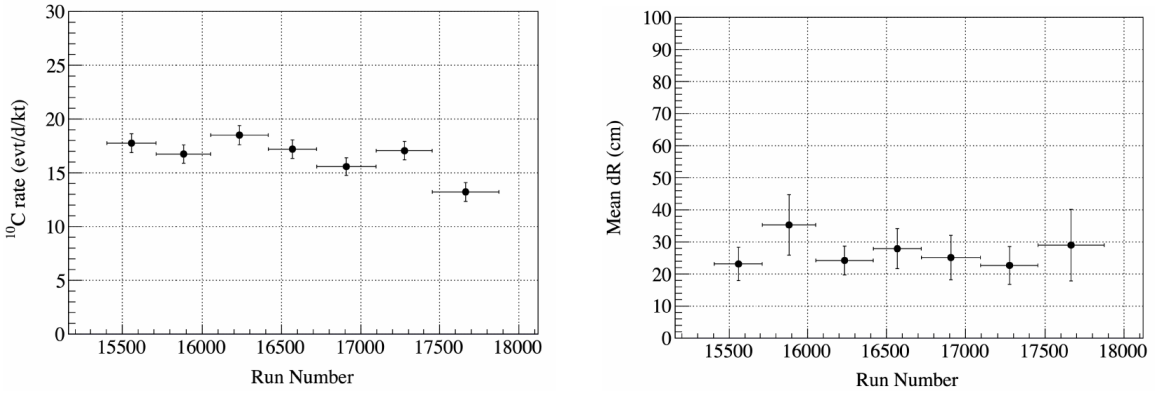

Figure 5·6: Time variation of ^{10}C rate and dR distribution shape over KLZ-800 data-taking.

5.2.1 Geant4 (KLG4)

KLG4 simulations used in this thesis analysis were tuned in [1] and [17]. This section describes their prior work in tuning KLG4 parameters.

KamLS Tuning

KamLS properties, the outer scintillator volume without dissolved xenon, are tuned using source calibration data taken on January 16, 2018. The calibartion deployment involved moving a composite radioactive soure between -550 and 550 cm in 50cm intervals. With 20 minutes of data-taking at each position. Table 5.1 describes the source composition.

Figure 5·7 shows the N_{hit} and total charge spectra of the composite source, with clearly visible gamma peaks. The gamma peaks are used to calibrate the nonlinearity of KamLS energy scale. The figure also shows the tuned KLG4 spectra that agrees well with data after tuning.

The energy scale is also tracked through position, via calibration source deployment. The deployment data was used to tune material properties like attenuation length, re-emission probabilities, and scattering probabilities. Figure 5·8 shows the position dependence of total charge for each source isotope. The variability and sim-

Table 5.1: Summary of radioactive source. Estimated intensities are as of January 17, 2018 on which the calibration DAQ was taken.

Construction date	Aug. 24, 2015		
DAQ date	Jan. 16, 2018		
Source ID	Kam-41 (composite source)		
	^{137}Cs	^{68}Ge	^{60}Co
Particle	1γ	2γ	2γ
Energy (keV)	661.7	511.0	1173.2, 1332.5
Initial Intensity (Bq)	181	419	322
Estimated Intensity (Bq)	180	356	234

ulation reproducibility with tuning is deteriorates as we move from the center of the detector. The physics analysis presented in this thesis focuses on data within 250cm. In this region, the deviation is within 2%.

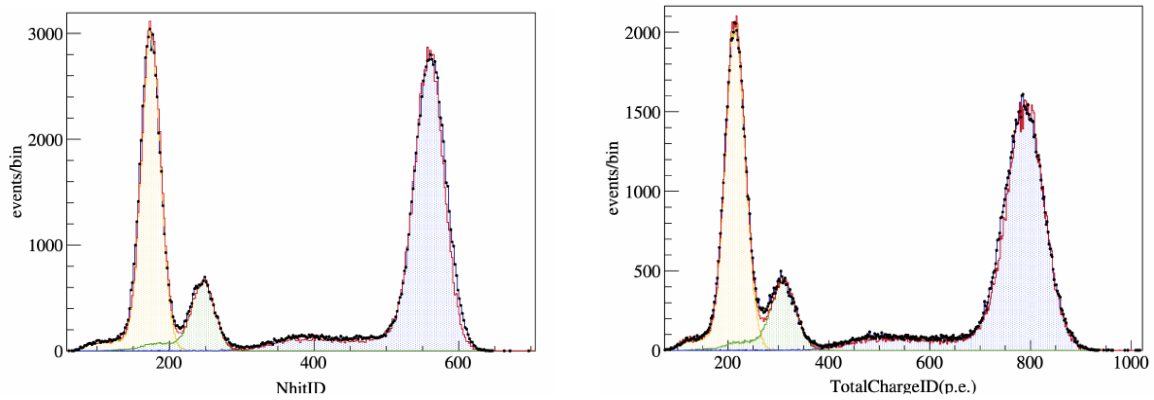

Figure 5·7: N_{hit} and total charge distribution of source calibration. Black plots show data and colored histograms (orange: 137 Cs, green: 68Ge, blue: 60 Co) show MC simulation. MC spectra are well tuned to data in both N_{hit} and total charge. Figures from [1]

XeLS Tuning

There are no source calibration located in XeLS. Alternatively, some background sources are available to calibrate the detector. ^{222}Rn is mixed in XeLS by emanation from pipeline or buffer tanks during xenon resolving work. A sequential decay of

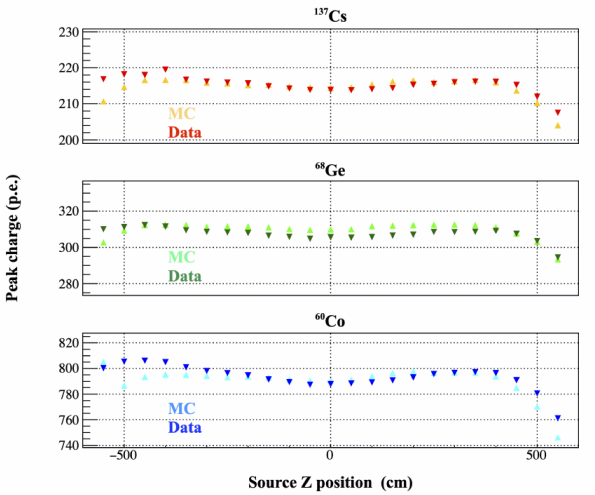

Figure 5·8: Position dependence of total charge peak for each calibration source isotope [1]

daughter isotopes ^{214}Bi-Po can be tagged using delayed coincidence and they exists only in XeLS. The half life of ^{222}Rn is 3.8 days and after completion of xenon resolving work, ^{222}Rn does not supplied. Thus ^{214}Bi-Po as high statistic calibration source is available only in first several months of KamLAND-Zen 800 observation. Birk's constant, attenuation length, scattering probability, LS time properties, and re-emission for XeLS are tuned using ^{214}Bi-Po.

Position-dependent Energy Correction

Position dependence, over radius and θ, of visible energy in XeLS is observed using the ^{214}Po *alpha* decay peak. The deviation from the center of the detector is reproduced in KLG4 as shown in Figure 5·9. The MC correction factors were tuned to ensure that the MC $0\nu\beta\beta$ decay peak in XeLS does not have a position dependence.

Energy Non-Linearity

The visible energy and the energy deposited by charged particles have a nonlinear relation due to the scintillation quenching and the contribution of Cherenkov light.

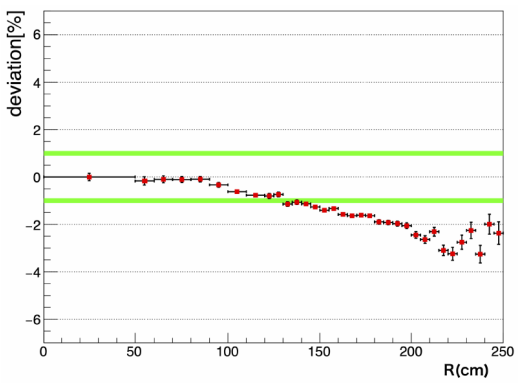

(a) Data

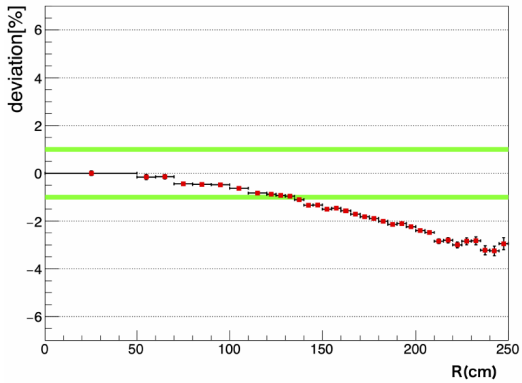

(b) MC (before correction)

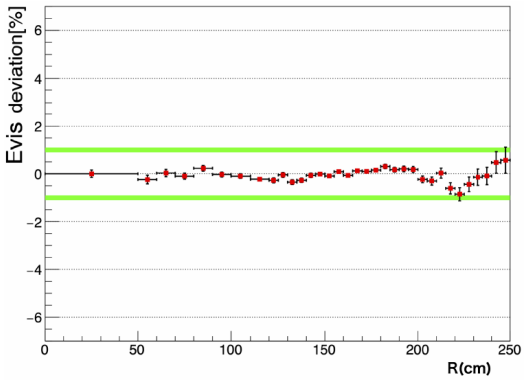

(c) MC (after correction)

Figure 5·9: Radius dependence of total charge of ^{214}Po. Figures from [1].

The following model is well known as Birks formula:

$$\frac{dL}{dx} \propto \frac{dE/dx}{1 + kB \cdot dE/dx'} \tag{5.1}$$

where dL/dx is light yield per unit length along particle track, dE/dx is energy deposited per unit length, and kB is the Birks' constant which is material dependent. Charged particles also emit cherenkov light, the proportion of the light yield attributed to cherenkov radiation is denoted by the chrenkov-scintillation ratio, R. Tagged ^{214}Bi data is used to tune kB and R. The tagged ^{214}Bi data in XeLS is primarily from the early ^{222}Rn-rich period. The tuning analysis was performed in

[1] and [17]. Figure 5·10 shows a $\Delta\chi^2$ scan over kB and R and the best fit of $(kB, R) = (0.31, 0.01)$. These are the values used in KLG4 for background and signal simulation. Figure 5·11 shows the result of XeLS tuning. The BiPo decay energies are matched to data and the spatial correlation between the coincident decays agree.

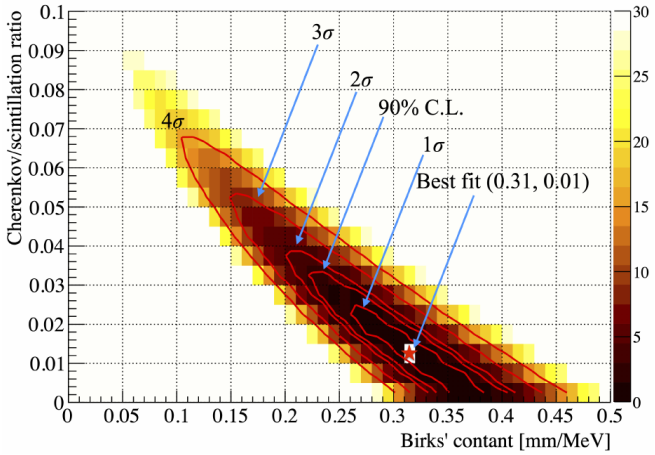

Figure 5·10: $\Delta\chi^2$ scan over kB and R

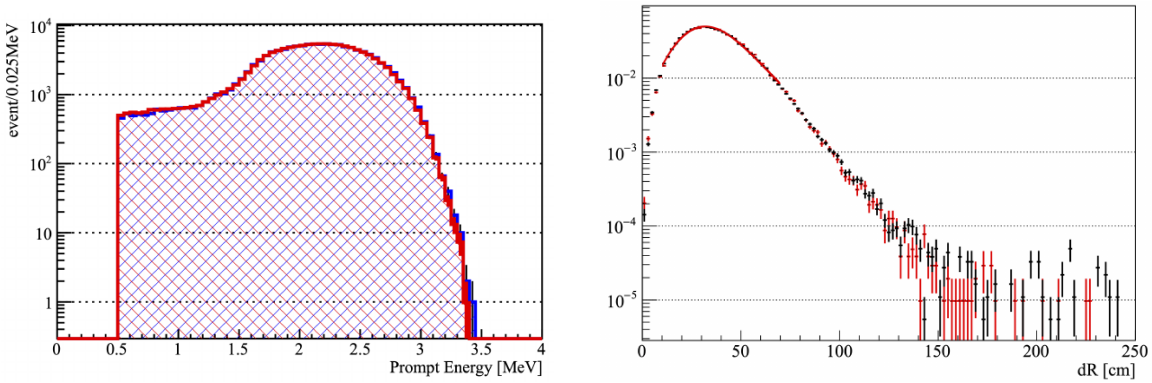

Figure 5·11: Tuned ^{214}Bi-β decay energy spectrum and spatial correlation of delayed-coincidence Bi-Po decays. Figures from [17]

Energy Scale

The overall energy scale of KamLS and XeLS are tuned by the neutron capture gamma peak of 2.2 MeV. XeLS introduces extra quenching by the xenon which reduces the

light yield in XeLS slightly. Figure 5·2 shows the peak energies used. This is the same dataset used for the energy scale time variation check.

5.2.2 FLUKA

FLUKA simulation software is used to predict cosmic muon spallation isotope yields and neutron production. The FLUKA version used in this modeling is FLUKA 2011.08.patch. Simulations and the results are described in [2]. Studies and measurements performed in KamLS are outlined in [56].

Simulation Configuration

The FLUKA physics process packages used in these spallation studies are listed in Table 5.2. FLUKA is only used to generate the production of spallation isotopes and neutrons, their decays and isomer production are disabled. The subsequent decays and neutron capture gammas are simulated in GEANT4.

Cosmic ray muon spallation is simulated by injecting muons into a cylindrical XeLS volume of 10 m radius and 40 m height. The inner balloon radius is only 2m. The volume within 10 m from the side and 5m from the exit is excluded from the analysis to avoid boundary effect. The MUSIC package is used to generate the cosmic ray muon energy distribution[57]. MUSIC takes in the detailed geometric description of the Kamioka mine where KamLAND is located. The generated energy distribution is fed into FLUKA and fired into the simulation's XeLS volume. The mean simulated muon energy is 260 ± 1 GeV. The simulation yields a neutron capture time of $\tau = 207.0 \pm 0.3 \mu$sec which is consistent with the previously measured value. The muon charge ratio is taken to be $\mu^+/\mu^- = 1.3$ in this simulation[58].

Table 5.2: FLUKA physics processes. From Ref.[2].

card	Physics	Status
DEFAULTS	A set of physics models	PRECISIO(n)
PHOTONNUC(lear)	Gamma interactions with nuclei	Activated
MUPHOTON	Muon photonuclear interaction	Activated
PHYSICS	Emission of light fragments	Activated by COALESCE(nse)
PHYSICS	Emission of heavy fragments	Activated by EVAPORAT(ion)
PHYSICS	Ion electromagnetic dissociation	Activated by EM-DISSO(ciation)
PHYSICS	Decay and isomer production	Activated by RADDECAY

Radioactive Decays

As previously described, FLUKA is used only for the direct spallation isotope production and neutron captures. The subsequent radioactive decays are simulated in the "Radioactive Decay" package in Geant4. The GEANT4 version used is Geant4.10.6.p01 with G4ENSDFSTATE2.2 for the Evaluated Nuclear Structure Data File (ENSDF) [59]. Table 5.3 lists the xenon spallation produts considered in this study. In total, 32 isotopes are selected that have production rates exceeding 0.01/day/XeLS-kton in the Region of Interest (ROI). Figure **??** shows the simulated energy spectra.

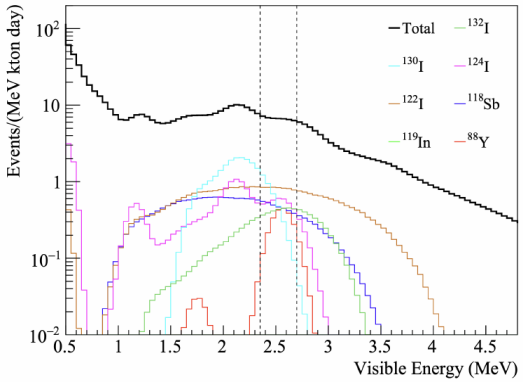

Figure 5·12: Simulated energy spectra of ^{136}Xe spallation products including their decay chain.

Tuning With ^{10}C

FLUKA simulations of radioactive decays and neutron capture gamma do not include detector effects and reconstruction performance. The information given by the FLUKA simulation includes the capture points of neutron captures but not the reconstructed vertices.

To approximate the effect of event reconstruction, the true neutron capture positions from FLUKA are convolved with a Gaussian resolution distribution. The neutron detection efficiency is also emperically modeled by:

$$\epsilon(\log_1 0Q_\mu) = \epsilon\left(1 - \frac{1}{1+e^{-\sigma(\log_1 0Q_\mu - a)}} + b\right) \tag{5.2}$$

The neutron detection efficiency is known to be particularly sensitive to baseline fluctuations in the immediate aftermath of a muon. Since, the baseline recovery time depends on the muon charge, the neutron detection efficiency, ϵ, is assumed ot depend on the charge.

$(1+e^{-\sigma x})^{-1}$ is a sigmoid function which mimics the error function and Q_μ is muon charge. σ controls the steepness of the sigmoid function's transition. Free parameters, σ, a, b are tuned to reproduce the dR and ENN distributions of ^{10}C as shown in Figure 5·13. dR is the spatial distance to the nearest neutron of a given shower, while ENN is the "effective number of neutrons". Vertex resolution affect both of these variables, while the neutron tagging efficiency primarily affects ENN.

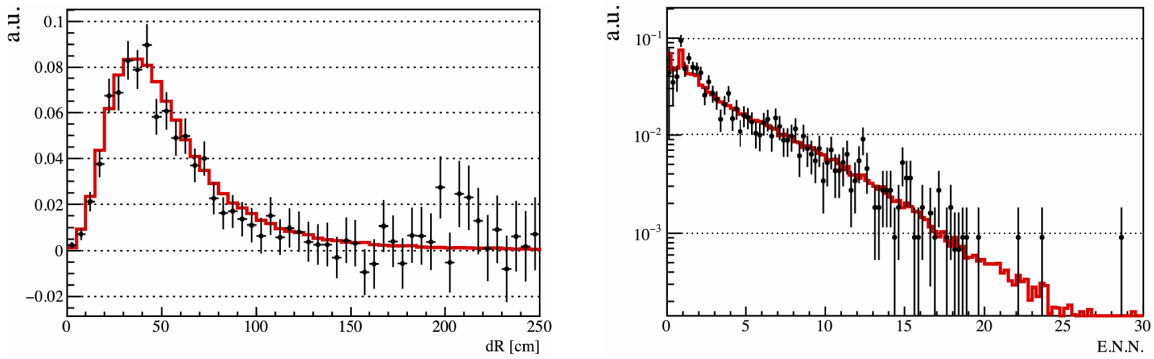

Figure 5·13: Tuned ^{10}C dR (left) and ENN (right) distributions from FLUKA (red curve) and data (black dots) Figures from [18]

Table 5.3: Breakdown of ^{136}Xe spallation products. Isotopes with production rates exceeding 0.01 /day/XeLS-kton in the Region of Interest (ROI) were considered and included in the background model.

isotope	decay mode	Q-value (MeV)	half-life (s)	ROI (day-kton)$^{-1}$	Total (day-kton)$^{-1}$
^{88}Y	EC/β^+/γ	3.62	9.212×10^{6}	0.110	0.136
^{90m}Zr	IT	2.31	8.092×10^{-1}	0.012	0.093
^{90}Y	EC/β^+/γ	6.11	9.212×10^{5}	0.024	0.095
^{96}Tc	EC/β^+/γ	2.97	3.698×10^{5}	0.012	0.059
^{98}Rh	EC/β^+/γ	5.06	5.232×10^{2}	0.011	0.076
^{98}Rh	EC/β^+/γ	3.63	7.488×10^{4}	0.088	0.234
^{103}Ag	EC/β^+/γ	4.28	4.152×10^{3}	0.012	0.160
^{104m}Ag	EC/β^+/γ	4.28	2.010×10^{3}	0.018	0.111
^{107}Cd	EC/β^+/γ	3.43	1.944×10^{3}	0.019	0.135
^{108}In	EC/β^+/γ	5.16	3.480×10^{3}	0.089	0.194
^{110}In	EC/β^+/γ	3.89	1.771×10^{4}	0.053	0.236
^{110m}In	EC/β^+/γ	3.89	4.146×10^{3}	0.066	0.351
^{110}Sn	EC/β^+/γ	3.85	1.080×10^{3}	0.027	0.122
^{113}Sb	EC/β^+/γ	3.92	4.002×10^{2}	0.036	0.231
^{114}Sb	EC/β^+/γ	5.88	2.094×10^{2}	0.020	0.297
^{115}Sb	EC/β^+/γ	3.03	1.926×10^{3}	0.031	0.839
^{116}Sb	EC/β^+/γ	4.71	9.480×10^{2}	0.071	0.939
^{118}Sb	EC/β^+/γ	3.66	2.160×10^{2}	0.165	1.288
^{116}Te	EC/β^+/γ	2.90	5.201×10^{6}	0.016	0.054
^{115}Te	EC/β^+/γ	4.64	3.489×10^{2}	0.012	0.124
^{117}Te	EC/β^+/γ	3.54	3.720×10^{3}	0.052	0.584
^{119}I	EC/β^+/γ	3.51	1.146×10^{3}	0.053	0.533
^{120}I	EC/β^+/γ	5.62	4.896×10^{3}	0.091	0.953
^{122}I	EC/β^+/γ	4.23	2.178×10^{2}	0.289	1.965
^{124}I	EC/β^+/γ	3.16	3.608×10^{5}	0.190	1.654
^{108}I	β^-/γ	2.95	4.450×10^{4}	0.195	1.188
^{132}I	β^-/γ	3.58	8.262×10^{3}	0.148	0.427
^{134}I	β^-/γ	4.18	3.150×10^{3}	0.043	0.183
^{121}Xe	EC/β^+/γ	3.75	2.406×10^{3}	0.100	0.540
^{125}Cs	EC/β^+/γ	3.09	2.802×10^{3}	0.012	0.266
^{126}Cs	EC/β^+/γ	4.82	9.840×10^{1}	0.011	0.080
^{128}Cs	EC/β^+/γ	3.93	2.196×10^{2}	0.031	0.229

Chapter 6

Backgrounds

In the analysis for excited state decays in KamLAND-ZEN, the signal is searched for via energy spectrum fit. While chapter 4 described event selections applied in data to reduce backgrounds, this chapter describes how the background energy distributions are modeled and estimated. This chapter describes expected distributions of background events that pass those event selections. These distributions are implemented in the spectral fit of Chapter **??**, along with any independent constraints that can be placed on their intensities.

While in other KamLAND-ZEN analyses, the spatial distribution of the events is used in distinguishing signals from backgrounds, due to issues in the radial distribution modeling, only the innermost part of the detector is used. Further discussion of the volume selection used for the excited state analysis can be found in Chapter **??**

6.1 $2\nu\beta\beta$: Double-Beta Decay

Two neutrino double-beta decay ($2\nu\beta\beta$) is the largest background in the search for $2\nu\beta\beta$s by far. The search for excited state decays is largely reduced to a search for a distortion in the $2\nu\beta\beta$ decay spectrum.

In KamLAND-ZEN, two isotopes of Xenon undergo $2\nu\beta\beta$, ^{134}Xe and ^{136}Xe. Of the Xenon dissolved in the XeLS, approximately 90% is ^{136}Xe and 9% is ^{134}Xe. ^{136}Xe decays have been studied in many experiments, the rate of this background is allowed to float freely in this analysis. ^{134}Xe decays have yet to be observed, the world-

leading limit on this isotope's half-life is $T_{1/2} > 8.2 \times 10^{20}$ years at 90% C.L.. This rate corresponds to an event rate of 2.7×10^4 events/day/kton in KamLAND-ZEN's XeLS.

While ^{134}Xe decay could be a secondary physics goal of KamLAND-ZEN, in practice, the signal is completely masked by residual ^{85}Kr and ^{210}Bi contamination in the detector. In addition, theoretical predictions place the expected ^{134}Xe half-life around 3 orders of magnitude higher than ^{136}Xe. For these reasons, ^{134}Xe is neglected in this analysis.

6.2 Radioactive Contamination

6.2.1 ^{238}U Series

^{238}U is a naturally occurring radionuclide with half-life $T_{1/2} = 4.468 \times 10^9$ years. ^{238}U is responsible for 40% of the radioactive heat generated in the earth. As an omnipresent radioactive contaminant it is present in all components of the detector to some degree.

The decay series of Uranium includes U, Th, Pa, Ra, Rn, Po, At, Pb, Bi, and Tl. All of the radioactive decays with energy spectra above 0.5 MeV are included in the background model. A distinction is made between the decays before ^{222}Rn, henceforth referred to as "Series 1", and after ^{222}Rn, henceforth referrred to as "Series 2". ^{238}Us1 enters the detector as ^{238}U as radioactive contamination from construction. Thus, all the ^{238}Us1 decays are in specular equilibrium with each other. ^{238}Us2 is introduced to the detector as ^{222}Rn during the original introduction of Xenon into the XeLS. In this and most KamLAND-ZEN analyses, the rates of ^{238}Us1 and ^{238}Us2 are fitted independently from each other. ^{238}Us1 is floated freely and is determined from the spectral fit, while ^{238}Us2 is constrained by the rate of tagged ^{214}Bi decays via the delayed-coincidence method described in Chapter 4. A penalty term is added to the

fit likelihood to implement this constraint.

6.2.2 ^{232}Th Series

^{232}Th is another omnipresent radioactive contaminant on earth. Just as in the ^{238}U model, the ^{232}Th decay chain is split into 2 series. The decays upstream of ^{228}Th are henceforth referred to as "Series 1", while the decays downstream of ^{228}Th are henceforth referred to as "Series 2". Once again the lower energy threshold of 0.5 MeV is used.

The rates of both decay chains are fitted independently in the energy spectral fit. It is worth noting that in the higher-energy window of 3-5 MeV, the dominant contributor is ^{208}Tl decay. Thus, the rate of ^{208}Tl can be comparatively well determined by the spectral fit, and the other backgrounds in the decay chain can be determined by the rate of ^{208}Tl decays in KamLAND-ZEN.

6.2.3 ^{40}K

^{40}K is another omnipresent, common radionuclide on earth. It decays via $beta^-$ decay with 89.28% B.R. and electron capture with 10.72% B.R. with a half-life of $T_{1/2} = 1.28 \times 10^9$ years. Like the other backgrounds it is assumed to be present in all the detector materials including XeLS, balloon film, and KamLS. But due to the high level of liquid scintillator purity, it is expected that the contamination of ^{40}K in the liquid scintillator volumes to be negligible and that the ^{40}K background to be concentrated on the inner balloon film. In this analysis a special study was done to estimate the amount of film ^{40}K is present in KamLAND-ZEN.

The most important feature of ^{40}K decay with regard to the analysis for excited state decays of ^{136}Xe is the ^{40}K electron capture gamma peak, $Q = 1.5$ MeV. In the KamLS, outside the inner balloon, this peak is prominent enough to resolve on its own.

In order to estimate the amount of film-related ^{40}K background that gets reconstructed in the innermost XeLS volumes, the radial distribution outside the balloon is measured. The volumes just inside and just outside the inner balloon were separated into equal volume spherical shells. The data in each of these spherical shells was independently fitted with a simplified version of the full KamLAND-ZEN spectral fit. The purpose of each of these fits is to measure the prominence of the ^{40}K electron-capture gamma peak over the broad $2\nu\beta\beta$ background. The trend of the individually-fitted rates of ^{40}K in each of the spherical "volume bins" is compared to the expected radial distribution from KLG4Sim simulations of ^{40}K. A simple least squares "fit of fits" is performed to determine the measured rate of ^{40}K from the inner balloon film.

While an initial deviation from the expected distribution was found, vetoing the upper balloon neck region yielded an excellent qualitative match between the measured and simulated ^{40}K radial distributions. This independent measurement of the radial distribution supports the hypothesis that the ^{40}K contamination is mostly limited to inner balloon film itself and much lower in the liquid scintillator volumes. This behavior matches the relative contamination levels of ^{238}U and ^{232}Th.

$$Y_{K40\ film} = 183 \pm 13 \text{events/day} \tag{6.1}$$

This indepedently measured rate of ^{40}K is implemented in the spectral analysis as a penalty term.

6.2.4 ^{85}Kr

^{85}Kr is a radioactive isotope realeased into the atmosphere when spent nuclear fuel is reprocessed. It decays via β^- decay with a half-life of $T_{1/2} = 10.76$ years. Despite such a short half-life the atmospheric contribution of ^{85}Kr continues to increase. ^{85}Kr is expected to be introduced to KamLAND-ZEN during liquid scintillator purification.

Previous KamLAND-400 and KamLAND analyses observed a non-uniformity in the rate of^{85}Kr along the z-axis of the detector. In this study, the ^{85}Kr rate is allowed to float freely in the inner XeLS volume. ^{85}Kr is a major contributing background in the lower energy region.

6.3 Carbon Spallation

A major class of backgrounds for both the $0\nu\beta\beta$ and $2\nu\beta\beta^{*}$analyses are radioactive isotopes produced when cosmic ray muons spallate Carbon nuclei in the detector. In this work, a distinction is made from the isotopes with half-lives of seconds or minutes, henceforth referred to as "short-lived", and the spallation isotopes, usually from Xenon with much longer half-lives, henceforth referred to as "long-lived". The following sections describe the modeling of the expected contribution of these short-lived isotopes.

6.3.1 Short-Lived Spallation Products

The short-lived carbon spallation products, primarily ^{6}He, ^{8}B, ^{8}Li, ^{10}C, and ^{12}B are effectively vetoed by the triple coincidence methods described in Chapter 4.

The contribution of the background rate that passes the triple coincidence veto can be simply estimated by Energy-dT fitting. dT is the time delay from the muon event that produces the isotope and the isotope's eventual decay. The event rate of the candidate spallation products over time can be written as

$$\frac{dN}{dt} = \sum_{i} N_i \times \exp\left(\frac{-dT}{\tau_i} + C\right) \tag{6.2}$$

where N_i is the number of observed events of isotope, i. τ_i is the i-th isotope's average lifetime and C is the rate of accidental events, not cosmic muon related. By fitting the event rates of each of the isotopes and accidentals with the above function, the

rate of overall spallation backgrounds can be estimated.

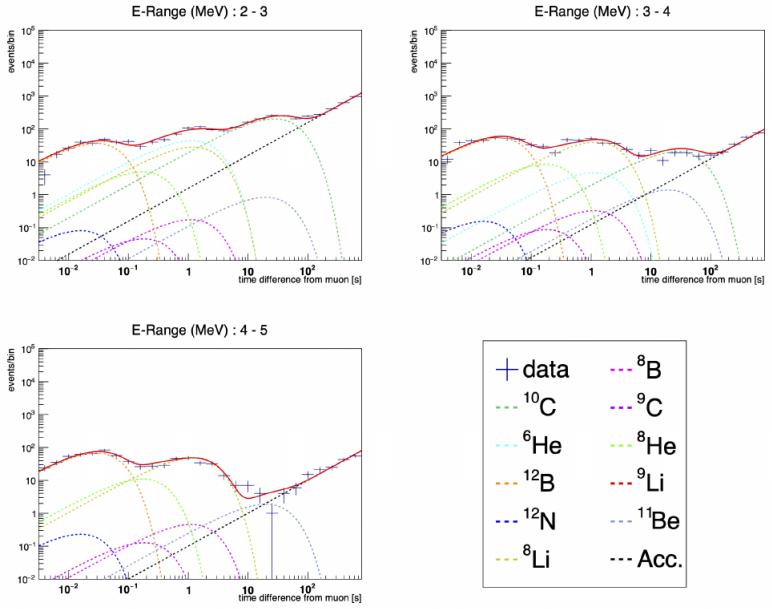

Figure 6·1: The fit to short-lived spallation backgrounds over Energy and dT. While the fit for the spallation rates is performed in the energy range 2-5 MeV, the full expected energy distributions are used in the excited state analysis spectral fit. Figure taken from [18]

The fit is performed simultaneously over the three energy regions shown in Figure 6·1. The residual rate of these backgrounds that are not triple coincidence vetoed are estimated using the fitted rates and the shower likelihood selection efficiency. The estimation was performed with KamLS events, the possible discrepancy between spallation production rates in KamLS and XeLS is included in the systematic errors. The short-lived spallation results are summarized in table 6.1.

6.3.2 ^{11}C Spallation Estimation

^{11}C is the dominant spalation isotope in KamLAND-ZEN, FLUKA estimates the production of ^{11}C to be 679 ± 49 event/day/kton. The estimated rate is a clear outlier compared to the other short and long-lived isotopes. It is also the dominant background in the medium-energy range of the KamLAND-ZEN analysis, 1-2 MeV,

Table 6.1: Production and background rate of carbon spallation products

	E [MeV]	τ	Prod. rate [evt/d/kton]	Bkg. rate [evt/d/kton]	Rej. eff. [%]
^{6}He	3.51 (β^-)	1.16 s	$12.36^{+1.22}_{-1.28}$ (28 ± 2)	$0.33^{+0.23}_{-0.02}$	$97.6^{+1.7}_{-1.7}$
^{10}C	3.65 (β^+)	27.8 s	$18.70^{+0.72}_{-0.64}$ (23 ± 2)	$0.00^{+0.03}_{-0.00}$	$100^{+0.00}_{-0.66}$
^{8}Li	16.0 (β^-)	1.21 s	$25.77^{+0.92}_{-1.04}$ (47 ± 3)	$0.025^{+0.13}_{-0.14}$	$99.1^{+0.5}_{-0.5}$
^{12}B	13.4 (β^-)	29.1 ms	$56.14^{+1.29}_{-1.28}$ (42 ± 3)	$0.015^{+0.002}_{-0.002}$	$100.0^{+0.0}_{-0.0}$
^{8}B	18.0 (β^+)	1.11 s	$0.58^{+0.71}_{-0.44}$ (11 ± 1)	$0.07^{+0.09}_{-0.07}$	$88.3^{+14.8}_{-19.8}$
^{12}N	17.3 (β^+)	15.9 ms	$0.218^{+0.20}_{-0.12}$ (0.74 ± 0.06)	0^{+0}_{-0}	$100^{+0}_{-0.0}$
^{9}C	16.5 (β^+)	182.5 ms	$0.53^{+0.54}_{-0.44}$ (1.5 ± 0.1)	$0^{+0.01}_{-0}$	$100^{+0.0}_{-1.0}$
^{8}He	10.7 (β^-)	171.7 ms	$4.89^{+0.93}_{-0.86}$ (0.55 ± 0.04)	$0^{+0.02}_{-0}$	$100^{+0}_{-0.3}$
^{9}Li	13.6 (β^-)	257.2 ms	$0.00^{+1.19}_{-0}$ (4.9 ± 0.4)	$0^{+0.01}_{-0}$	-
^{11}Be	11.5 (β^-)	19.9 s	$1.06^{+0.69}_{-0.21}$ (1.1 ± 0.1)	$0.00^{+0.26}_{-0}$	$100^{+0.0}_{-22.1}$

aside from $2\nu\beta\beta$ itself. Thus, the determination of the ^{11}C production rate is key for constraining the $2\nu\beta\beta$ rate.

The production rate of ^{11}C was measured in previous phases of the experiment in KamLS using muon-coincidence. The measurement was replicated in KamLAND-ZEN 800's XeLS using MoGURA neutron coincidence.

The independent measurement of ^{11}C decays is performed by observing $\mu - ^{11}C$ pairs in KamLAND-ZEN 800. The following selections were applied to the ^{11}C decay candidate events.

- dT, Muon delay from event : $100 < dT < 18,000$ sec/5 hours
- Event quality cuts as described in Chapter 4, excluding Badness veto to include ^{11}C-orthopositronium decays
- Excluding other spllation-related selections: Longlived veto, MoGURA neutron veto, and ^{137}Xe
  - The cut on muon delay, $dT > 100s$, excludes most of the short-lived backgrounds.

- $dR < 80$ cm : Nearest neutron per muon shower
- $0 < radius < 160$ cm : Fiducal Volume selection for pure XeLS events
- $1.0 < E_{vis} < 1.6$ MeV : Energy selection for S/B optimization

Applying the ^{11}C selection to the full KamLAND-ZEN 800 dataset, the distribution of dT is observed in Figure 6·2. The accidental background from $2\nu\beta\beta$ decays is significant, but the ^{11}C decay distribution is clear. The distribution is fitted to an exponential decay with fixed ^{11}C lifetime $\tau = 1,764$ secs, and a linearly sloping background.

A similar selection was also applied to the KamLS region in KamLAND-ZEN 800. The adjusted selections are on reconstructed event radius $220 < r < 350$ cm and event energy $1.0 < E_{vis} < 2.2$ MeV, the KamLS distribution is also shown in 6·2. The ^{11}C decay signature is especially clear in KamLS as the relative background is much lower due to the reduction in $2\nu\beta\beta$ events.

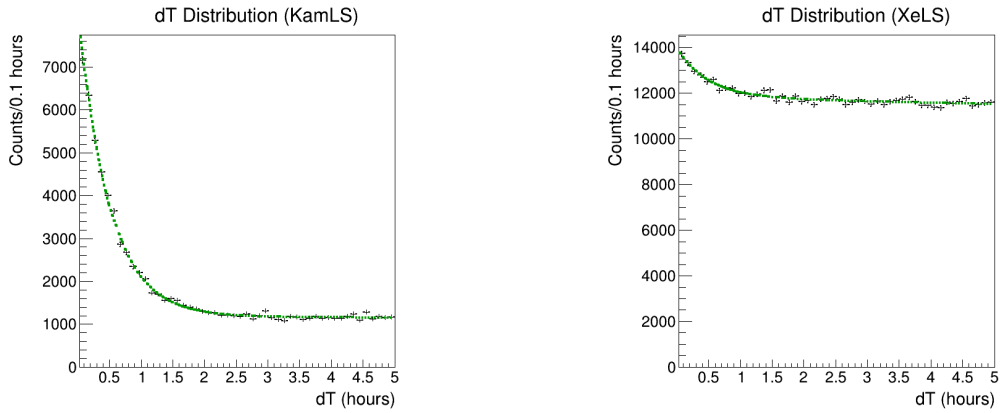

(a) KamLS **(b)** XeLS

Figure 6·2: Distribution of dT (time delay from muon to event) for muon-event pairs passing all selection cuts, shown separately for KamLS and XeLS.

Another crosscheck is performed with the energy distribution of the selected ^{11}C candidate events. The $\mu - ^{11}C$ pair dT distribution is seperated into "ontime" and

"offtime" bins. Then the energy distribution of the offtime events are subtracted from the energy distribution of the ontime events. The subtracted energy distributions are shown in Figure 6·3. In KamLS, the observation of simulated the ^{11}C energy spectrum is clear. While in XeLS, the fluctuations in the significant background worsen the comparison to simulation, the broad ^{11}C spectrum is clearly resolved. This crosscheck using an ontime-offtime analysis of the energy distribution gives us confidence that ^{11}C is indeed being selected with good purity.

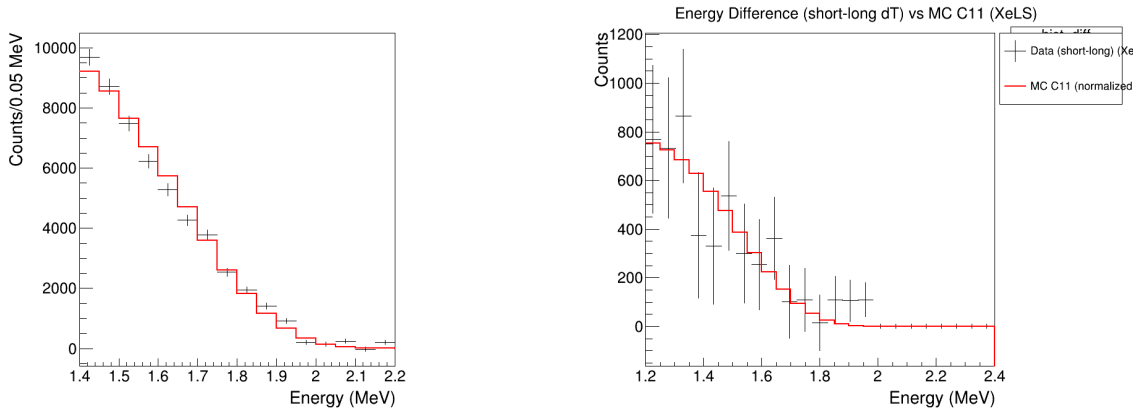

(a) KamLS **(b)** XeLS

Figure 6·3: Subtracted energy distributions compared to MC ^{11}C in XeLS and KamLS.

There are many spallation isotopes produced in Xenon-spallation with lifetimes of similar orders of magnitude $10^3 - 10^4$ seconds as ^{11}C, $\tau = 1,764$ seconds. Instead of estimating the relative production of each of these isotopes, the effect of the cumulative background is modeled with an uncosntrained linear slope to the background.

^{11}C Rate Calculation

From the exponential fit results of the dT distribution, the production rate of ^{11}C in XeLS can be estimated. The calculation of expected number of detected, selected,

and correlated ^{11}C-μ pairs is modeled as:

$$I_{C11} = Y_{C11} \times E_{FBE} \times (1 - dt_{MoG}) \times \epsilon_{dR} \times \epsilon_{dT} \times \epsilon_{FV} \times \epsilon_{E} \tag{6.3}$$

- $I_{C11} = 10,028$: Integral of the exponential component of the fit, "Observed $\mu-^{11}$C pairs" [*events*]

$$I_{C11} = A_{C11} \cdot \tau \cdot \frac{e^{\frac{-100}{\tau}} - e^{\frac{-18000}{\tau}}}{(18000 - 100)/50} \tag{6.4}$$

- Y_{C11}: **Final Result** Production rate of ^{11}C in KamLS, XeLS [$events/kton{\cdot}days$]
- $E_{FBE} = 22.71$: XeLS Exposure [$kton \cdot days$]
- $dt_{MoG} = 1.88\%$: MoGURA Deadtime Fraction
- $\epsilon_{dR} = 57\%$: $dR < 80$ cm cut efficiency (from FLUKA tuned with ^{11}C), for each data period [unitless]
- $\epsilon_{dT} = 94.5\%$: dT $>$ 100s cut efficiency (from known ^{11}C half-life) [unitless]
- $\epsilon_{FV-E} = 79.7\%$: Fiducial Volume & Energy Cut Efficiency taken from KLG4Sim [unitless]

From the integrated observed events from the exponential component of the fit, and the estimation of the relevant efficiency factors, the production rate of ^{11}C in XeLS is calculated.

$$Y_{C11} = 1,050 \pm 110 \; events/kton \cdot day \tag{6.5}$$

The uncertainty is estimated by considering a few major sources of uncertainty, the included uncertainties are listed in Table 6.2.

Table 6.2: Sources of uncertainty in the ^{11}C production rate calculation.

Source	Uncertainty (%)
Statistical	5.4
Exposure uncertainty	4.0
Exponential fit model choice	7.0
Neutron production	7.8
Total uncertainty	10.7

6.3.3 ^{137}Xe

When neutrons spallated by cosmic ray muons are captured on ^{136}Xe, ^{137}Xe is produced. The Q-value of its β^- decay is 4.16 MeV with a half-life of $T_{1/2} = 229$ sec. The neutron capture cross section calculation yields a production rate of 3.9 event/day/kton. The tagging efficiency of ^{137}Xe is estimated as $74 \pm 7\%$. The long-lived spallation veto, described in the next section, also removes ^{137}Xe. The veto efficiency by the long-lived spallation veto is estimated from FLUKA simulation to be 42%. The residual rate in the singles dataset is estimated to be 0.43 ± 0.36 event/day/kton.

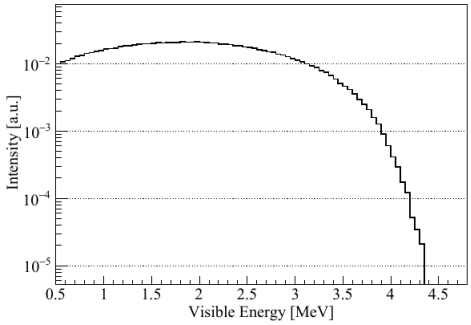

Figure 6·4: The fit to short-lived spallation backgrounds over Energy and dT. While the fit for the spallation rates is performed in the energy range 2-5 MeV, the full expected energy distributions are used in the excited state analysis spectral fit. Figure taken from [18]

6.4 Long-Lived Xenon Spallation Products

Spallation products from ^{136}Xe are the second most dominant bacvkground in the $0\nu\beta\beta$ ROI. Long lived spallation affects the resolution of the $2\nu\beta\beta$ endpoint which affects the energy scale resolution and the final rate of $2\nu\beta\beta$.

The half-lives of these isotopes are longer than the carbon spallation products, typically taking hours or days to decay. This makes tagging their decays and estimating their contributions difficult with simple box cuts or coincidence analyses. In the $0\nu\beta\beta$ analysis, a likelihood-based tagging method was developed to separate the datasets into one with lower spallation background contamination, "Singles data" and one with higher spallation background concentration, "Long-Lived data". In the excited state fit, to reduce systematic uncertainty in the ^{11}C background estimation which is a much larger contributor to the excited state energy region, this separation of the dataset based on likelihood of being a long-lived spallation event is not done. Instead, the long-lived background contribution has to be carefully estimated by the methods described in this section.

6.4.1 FLUKA Simulation

To estimate the production rate of the spallation products, muons are injected into a simplified version of the KamLAND detector. In the FLUKA simulation environment, concentric spheres of XeLS ($0 < r < 192cm$), KamLS ($192 < r < 650cm$), and Buffer Oil ($r = 9m$) are simulated. Cosmic ray muon flux including angular and energy distributions are taken from the MUSIC simulation of muon flux at the KamLAND site. 10^7 μ^+ and μ^- events are simulated which corresponds to 37 years of cosmic ray observation with KamLAND. The muon sign ratio is taken to be $\mu^-/\mu^+ = 1.3$. Figure 6·5a shows the production rate of each nuclide in XeLS.

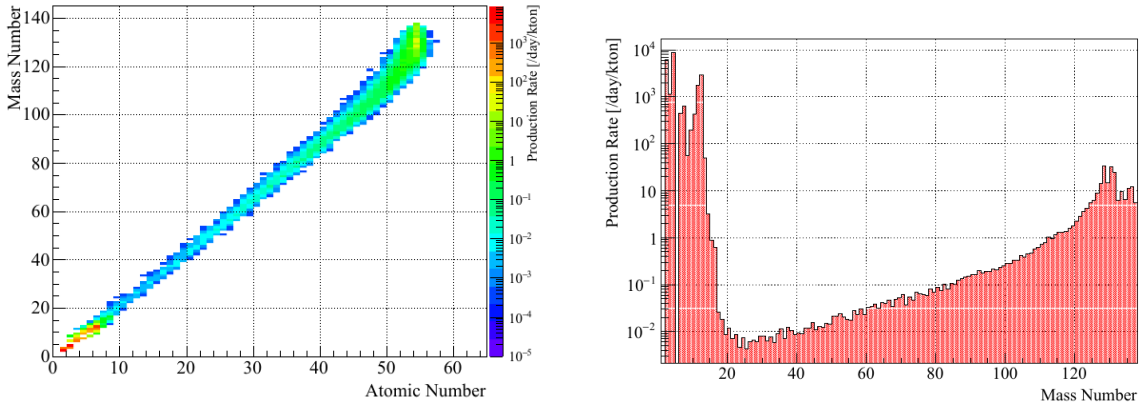

(a) Atomic Mass vs Atomic Number **(b)** Atomic Mass

Figure 6·5: Production rates of spallation nuclei in KamLAND-ZEN XeLS. There are two concentrations, one near ^{136}Xe the original heavy isotope in XeLS, and one near the ligher scintillator components ($A \sim 10$) like Carbon and Oxygen. Figure taken from [17].

6.4.2 ENSDF Database

FLUKA is used to simulate the spallation processes, but the radioactive products' final decays are not simulated. Instead the simulation of the decay vertices are done in KLG4Sim just as the other backgrounds and signals. From FLUKA, the relative production rates of the spallation isotopes are collected. The half-lives and branching ratios of each species' decay is read from the ENSDF database and the decay chains are followed using the RadioactiveDecay package in GEANT4 simulation. Then the rates of each background in the excited state region of interest is evaluated. Table **??** shows the rates of the dominant long-lived spallation backgrounds. There are hundreds of produced spallation isotopes, but those listed account for more than 95% of the expected background contribution.

6.4.3 Spectrum Distortion

In the abscence of dedicated cosmic-ray muon induced xenon-spallation measurements, checking the validity of FLUKA's spallation simulation is difficult. The results

of 2 beam experiments are taken into account. The first is an experiment where a 490 GeV μ^+ beam on gaseous xenon reports the production of charged hadrons [60]. Test FLUKA simulations can reproduce their measurements.

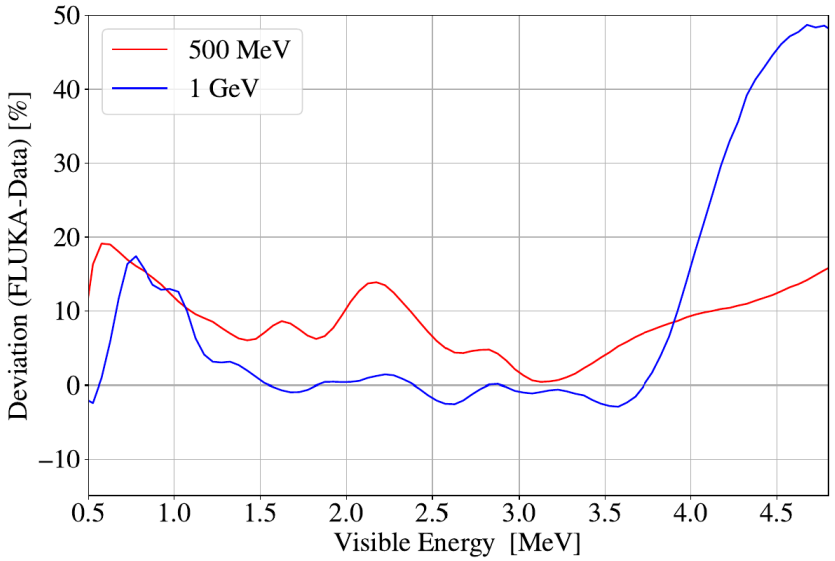

Figure 6·6: The comparison between FLUKA simulation and Xenon beam experiment data. Red line show the difference from [19]. Blue line shows the difference from [20]. The red line is adopted as the error and considered in the spectrum fit since the deviation in $0\nu\beta\beta$ ROI is larger

Another expriment measured the cross section of a ^{136}Xe beam on a 1 cm^3 liquid-hydrogen target. The incident energy per nucleon used was 500 MeV [19] and 1 GeV [20]. The comparison of our FLUKA derived long-lived spallation decay spectrum and these beam measurements are shown in Figure 6·6.

The discrepancy shown in Figure 6·6 indicates a potential mismodeling of the long-lived spallation background energy distribution. This uncertainty is implemented in the spectral fit, by introducing a distortion parameter that varies the model of the long-lived spallation background, based on this discrepancy with experiment.

6.5 Other Backgrounds

6.5.1 External Gamma-Rays

Gamma rays emitted by radioactive isotopes from outside the detector can travel into the sensitive regions and deposit energy. The most dominant of these backgrounds is the 2.6 MeV gamma ray from ^{208}Tl in the PMT glass. The energy and spatial distributions are simply estimated from actual experimental data. The external gamma contribution decays exponentially as it travels into the inner regions of the detector, so it can be extrapolated from the outer regions.

Figure 6·7a shows the radial distribution of external gamma events within the visible energy range of 2.6-2.65 MeV. The distribution is fitted with a sum of exponential and 2nd polynoiail functions (modeling external gamma rays and radially uniform events). Extrapolating the exponential component into the inner detector, the background rate within $r < 300$ cm is calculated to be 0.32 ± 0.05 event/day/kton for $z < 0$ and 0.69 ± 0.12 event/day/kton for $z > 0$. The radius and energy distribution of the external gamma ray modeled background is shown in Figure 6·7b.

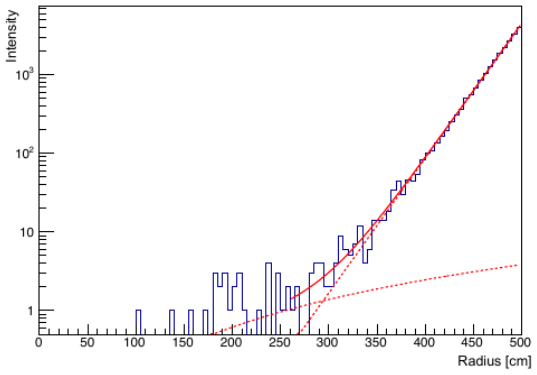

(a) Fit to the external gamma background over radius. The solid line is the total fit, while the dashed liens show the exponential and 2nd degree polynomial components. Figure taken from [17].

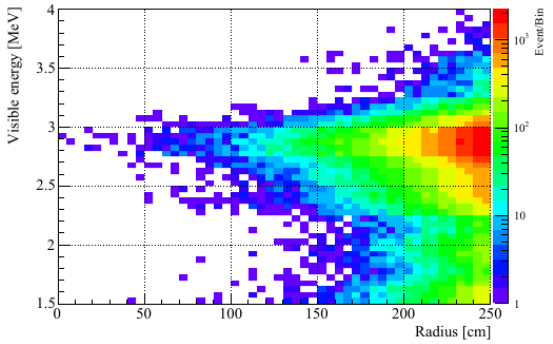

(b) Modeled background of external gamma rays. Note that the 2.6 MeV ^{208}Tl peak is reconstructed at a higher energy, $\sim$ 2.8 MeV. This is due to the higher light-yield of the outer KamLS, and the calibration of E_{vis} to XeLS events. Figure taken from [17].

Within the inner FV $r < 1.33$m that the excited state analysis is performed in,

the external gamma background is expected to be negligible from extrapolation of the fitted exponential distribution. Thus, the external gamma background is not implemented in the spectral fit for the excited state decays.

6.5.2 Solar Neutrinos

Neutrino interactions are an irreducible background for the excited state decay search. Notable neutrino fluxes in KamLAND include, solar neutrinos, atmospheric neutrinos, geoneutrinos, and reactor neutrinos. Among those solar neutrinos have the highest flux at energies below 20 MeV. Neutrions interact in the detector either via elastic scattering (ES) or charged current interactions (CC).

In ES, a neutrino scatters off an electron in the detector. The emitted electron then deposits energy in the liquid scintillator. An energy spectum of solar neutrino fluxes is shown in Figure 6·8. Of these, ^{8}B solar neutrinos are the most significant in the $2\nu\beta\beta$ endpoint region. While other neutrino fluxes are present at lower energies, they are insignificant compared to the other backgrounds and are neglected in this work.

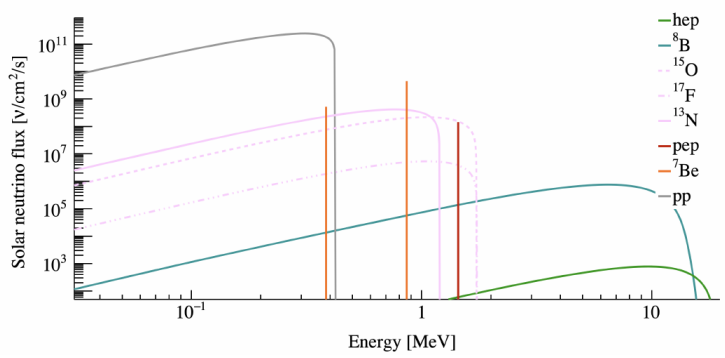

Figure 6·8: Solar neutrino fluxes. Figure from [21]

In CC interactions, ^{136}Xe interacts with neutrinos via inverse β decay:

$$^{136}Xe + \nu_e \rightarrow ^{136}Cs + e^- \tag{6.6}$$

^{136}Cs decays to ^{136}Ba with a half-life of $T_{1/2} = 13.01$ days and with $Q = 2.55$ MeV. Figure 6·9 shows the expenected visibl energy spectrum of ^{136}Cs decays. In this excited state decay search, both ^{136}Cs and ^{8}B decays are implemented in the spectral fit.

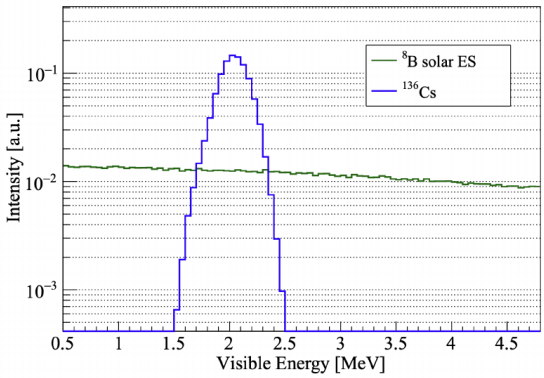

Figure 6·9: Modeled solar neutrino background included in excited state analysis. Figure from [17]

Chapter 7

$2\nu\beta\beta^*$ Analysis

This chapter describes the data analysis framework used to search for $2\nu\beta\beta^*$. First the KamLAND-ZEN 800 full dataset is described, including any vetoed data-taking periods. This description is followed by an overview of the systematic uncertainties. Then, the energy spectral fitting procedure is outlined, including the definition of the chi-square metric. Finally, the statistical results are presented, culminating in a limit on the $2\nu\beta\beta^*$rate.

7.1 Xenon Enrichment in KamLAND-ZEN

The amount of xenon gas dissolved into the XeLS is a normalization factor in the final xenon decay rates. The value is determined by subtracting off the xenon that remains after xenon installation:

1. initial Xe mass : 769 ± 1 kg
2. Xe left in LS in tanks and pipe lines : 21.5 ± 2.8 kg
3. Xe left in storage bottles : 1 ± 1 kg
4. Xe trapped by charcoal filter or used for sampling : 1.5 ± 0.5 kg

From the above calculation, the installed Xenon gas is determined to be, 745 ± 3 kg. The composition of the enriched xenon is evaluated using a mass spectrometer. The measured values agree well with the values provided by the procurement company. The enrich xenon composition can be seen in Table 7.1.

Table 7.1: Enriched Xenon Composition

	^{136}Xe	^{134}Xe	Others	Total
Provided ratio [%]	90.85	8.82	0.33	100.00
Measured ratio [%]	90.77 ± 0.08	8.96 ± 0.02	–	–
Atomic mass [u]	135.907	133.905	–	–
Total mass [kg]	677.39	64.83	2.79	745.0

7.2 Full KamLAND-ZEN 800 Dataset

The dataset used in this analysis was taken between February 5, 2019 and April 30, 2023, run range : 15431-18691. Unlike the $0\nu\beta\beta$ analysis, the dataset is not divided by Long-lived spallation background likelihood into a singles and long-lived dataset. Instead all the events are combined into a single energy spectrum for joint fitting.

7.2.1 Vetoed Data Periods

In addition to the regular deadtime due to maintenance, run quality, described in Chapter 4, there are additional vetoed data periods specifically for this analysis.

Electric Power Supply Instability

The run range 16790-16874 are excluded from this analysis because the DAQ was unstable due to AVR (automatic voltage regulator) trouble. The constant restarting of the DAQ leads to short runs which make it difficult to perform the run-by-run calibration described in Chapter 5.

MoGURA disorder period

The MoGURA DAQ system was unstable between September-November 2022 and raw data files were corrupted. While the KamDAQ files are readable, the MoGDAQ data is crucial for constructing events near after cosmic ray muons. These events are a key tag for cosmic related spallation backgrounds. Thus, runs 17768-17905 are

excluded from this analysis.

7.3 Systematic Uncertainties

While the $0\nu\beta\beta$ and $2\nu\beta\beta^*$analyses are statistical uncertainty dominated, this section discusses estimates of several sources of systematic error.

The uncertainty in the total amount of xenon dissolved in the XeLS was estimated in an internal study, the estimated uncertainty is 0.4%.

As for the xenon enrichment factor, the 0.1% difference in the supplier stated enrichment and our measuremed enrichment, described in the previous section, is used as the systematic uncertainty in xenon enrichment.

The detector energy scale varies over time as electronics fail, are repaired, and PMTs degrade. Using the neutron capture gamma peak at 2.2 MeV, a maximum error of 0.9% was determined.

Finally, the uncertainty in the fiducial volume is the uncertainty in the true volume of events encapsulated by the fiducial volume selection of 157.49 cm. This is determined using the early KLZ-800 data, just after xenon dissolving work. As the xenon is introduced, ^{222}Rn is incidentally introduced from the atmosphere, ^{222}Rn has a half-life of 3.8 days, and its decay is soon followed by a ^{214}Bi-Po sequential decays. Data for a month after xenon is introduced to the XeLS is used and the Bi-Po coincident events are analyzed. The volume ratio between spheres of 157.49cm and 192cm, the inner balloon radius, is 0.5686. While the ratio of Bi-Po events observed in these spherical regions is 0.5454. Since it is expected that the ^{222}Rn is distributed uniformly throughout the XeLS, a 4.1% difference is taken as the fiducial volume uncertainty.

7.4 Spectral Fit

The $2\nu\beta\beta^*$decay rate is estimated by fitting background and signal models to the energy distribution of reconstructed KLZ-800 data. Namely, the energy distribution of events within the reduced FV of ($r < 1.33m$) and that pass the event selections discussed in Chapter 4.

Unlike the $0\nu\beta\beta$ analysis [15], the data is not separated into time and hemipsherical volume bins. This is done to reduce systematic uncertainties and simplify the analysis. As this analysis is dominated by the statistics of the $2\nu\beta\beta$ background, the modeling of time-dependent changes in detector response should be marginal. By reducing the fiducial volume to ($r < 1.33m$) we sacrifice statistics but gain robustness by focusing on the best characterized region of the detector.

Thus, a simple 1-dimensional spectral fit is performed over the energy range (0.5-4.8) MeV wiht 0.05 MeV wide bins. This energy range spans the ^{210}Bi and ^{85}Kr peaks, the low-energy portion of the $2\nu\beta\beta$ spectrum, the ^{11}C and ^{40}K decays, the $2\nu\beta\beta$ endpoint, the $0\nu\beta\beta$ ROI, the ^{212}Tl peak, and the $2\nu\beta\beta^*$ ROI.

7.4.1 Chi-Square Definition

In this study, a binned chi-square, maximum likelihood fit is performed. The chi-square has multiple components, a energy-bin term and penalty terms.

$$\chi^2 = (\sum_{energy} \chi^2_{energy}) + \chi^2_{penalty} \tag{7.1}$$

Here, $\sum_{energy}$, denotes a sum over each 0.05 MeV energy bin from the range 0.5-4.8 MeV. In each energy bin, the χ^2 is computed.

$$\chi^2_{\text{energy}} = \begin{cases} 2\sum_i \left(\nu_i - n_i + n_i \log \frac{n_i}{\nu_i}\right) & (n_i > 0) \\ 2\sum_i (\nu_i - n_i) & (n_i = 0) \end{cases} \tag{7.2}$$

Now, ν_i is the model expected energy spectrum for the given fit parameters, and n_i denotes the observed number of events in the i-th bin. The penalty terms constrains certain parameters that have independent constraints. The fit parameter configuration is summarized in Table 7.2, and described in more detail in the later sections. The penalty χ^2 terms are simply defined as:

$$\chi^2_{penalty} = \sum_i \left(\frac{O_n - E_n}{\sigma_n} \right)^2 \tag{7.3}$$

where O_n is the estimated parameter value, E_n are the central expected values, and σ_n are the expected parameter errors.

7.4.2 Minimizer

The ROOT implementation of the MINUIT package distributed by CERN is the minimization package used for this analysis.

7.4.3 Fit Parameters

The spectral rate parameters are divided by origin volume. This analysis is only concerned with backgrounds originating in the XeLS and the inner balloon film. Each of the backgrounds described in Chapter **??** is implemented in the spectral fit.

7.4.4 Penalty Terms

The first penalty terms are on the rate of the constrained background sources. ^{238}U series 2, ^{222}Rn, ^{232}Th series 2 are determined from the rate of coincidence tagged ^{214}Bi-Po and ^{212}Bi-Po events. Next, the independent background constraints determined by this study in 6, ^{11}C and ^{40}K. ^{137}Xe is determined from coincidence with MoGURA neutron captures, the determination of the rate that passes the coincident cut is also described in 6.

A penalty term is also included for the detector response parameters. An overall

Table 7.2: Fit parameter configuration for the spectral analysis. The fit condition column indicates whether the parameter is free, fixed, scanned, or constrained in the fit.

Material	Parameter	Fit Condition
XeLS	^{136}Xe $2\nu\beta\beta^*$	scan
	^{136}Xe $2\nu\beta\beta$	free
	^{238}U series 2	constrain
	^{222}Rn	constrain
	^{232}Th series 2	constrain
	^{210}Bi	free
	^{85}Kr	free
	^{11}C	constrain
	^{137}Xe	constrain
	Xe spallation	free
	solar ν ES + CC	fix
	^{136}Cs	constrain
Film	^{238}U series 1	fix
	^{238}U series 2	free
	^{232}Th series 1	free
	^{232}Th series 2	free
	^{40}K	constrain
	^{210}Bi	free
all	Energy scale	constrained
	k_B, R	fix
	LL-distortion	constrain
	^{6}He	fix
	^{12}B	fix
	^{8}Li	fix
	^{8}B	fix

energy scale, scales all of the background and signal energy spectra via linear interpolation. The energy scale $\alpha_E = \frac{E_{vis}}{E_{sim}}$ is constrained to 1 ± 0.016. The Birks constant, k_B, and Chrenkov Ratio, R, are kept fixed for stability in the fit. In later analyses, the constraints on them should either be tightened or their effect quantified as another systematic uncertainty.

7.5 $2\nu\beta\beta^*$Results

7.5.1 Best Fit Result

The best fit result for the $2\nu\beta\beta^*$decay rate as given by MINUIT is 0, no significant excess over the background expectation was found. Figure 7·1 shows the fitted energy spectra.

Table **??** list the best fit parameter values. Constrained values are within their constraints with no significant biases, a notable deviation from previous analyses is the railing of ^{232}Th S1 film to 0, this background is also present in the ^{232}Th S2P film background. Without the radial component to differentiate the two, it is a superfluous parameter in the fit.

7.5.2 $2\nu\beta\beta^*$ Half-life Limits

In lieu of a positive $2\nu\beta\beta^*$signal, the upper limit on the rate can be determined from the 90% confidence level (C.L.). We perform a scan over the $2\nu\beta\beta^*$signal rate. The signal rate is fixed to various values and at each value, a new fit of the backgrounds is performed to the data. The worsening of the fit-data match is quantified by the $\Delta\chi^2$, the difference between the NLL test statistic from the best fit and the fit with a fixed signal rate. Figure 7·2 shows the scan results.

An estimate of the 90% C.L. upper limit on the rate is determined by searching for the threshold value of $\Delta\chi^2 = 2.71$. This threshold is given by Wilks' theorem for

Parameter	Value	Fit Condition
^{12}B Spallation	0.016	fix
^{8}B Spallation	0.239	fix
^{210}Bi (XeLS)	26000	floated
^{210}Bi (film)	22930	floated
^{11}C (XeLS)	983	constrained
^{136}Cs (XeLS)	0.8	fix
^{6}He Spallation	0.33	fix
^{40}K (film)	186	constrained
^{85}Kr (XeLS)	41500	floated
^{8}Li Spallation	0.525	fix
Long-lived (XeLS)	0.68	floated
Monochromatic	3.4e+07	fix
^{222}Rn (XeLS)	8002.15	constrained
Signal ($2\nu\beta\beta^*$, XeLS)	0	floated
Solar ν (XeLS)	4.87	fix
^{232}Th S1 (film)	0	floated
^{232}Th S2P (XeLS)	114	constrained
^{232}Th S2P (film)	98.7	floated
^{238}U S1 (film)	25	fix
^{238}U S2 (XeLS)	30.2	constrained
^{238}U S2 (film)	61.3	floated
^{136}Xe $2\nu\beta\beta$ (XeLS)	107601	floated
^{137}Xe (XeLS)	0.980653	constrained
Energy Scale α (Internal)	0.991	constrained
LL distortion	0.118	constrained
R (Internal)	0.018	fix
k_B (Internal)	0.31	fix

Table 7.3: The best fit parameter values and their fit conditions.

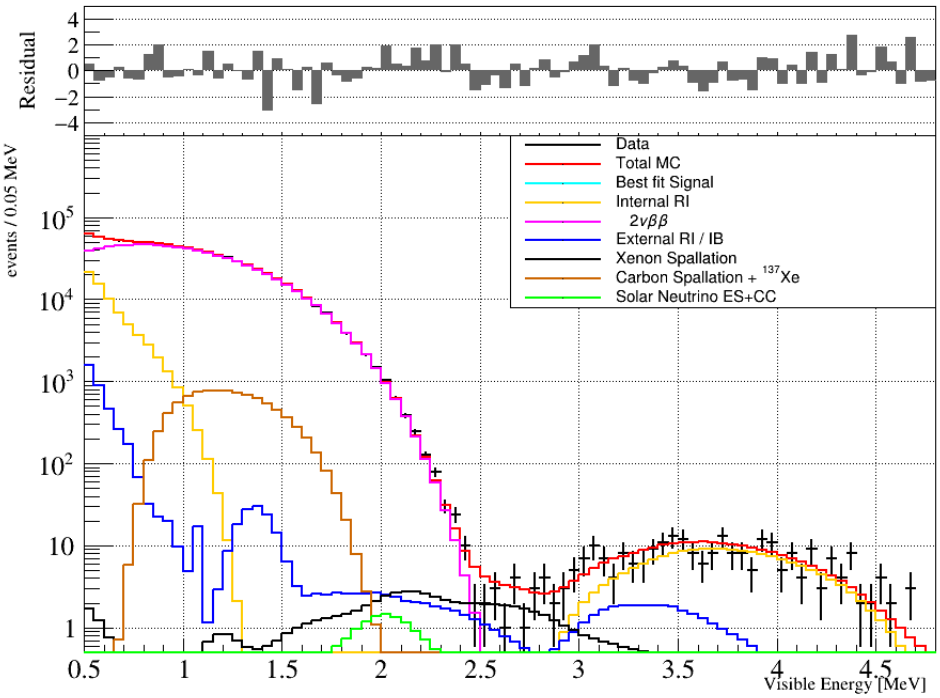

Figure 7·1: Best fit energy spectrum to full KLZ800 dataset in the reduced FV.

the 90% coverage of the test χ^2 distribution for a single parameter.

This upper limit on the rate is simply converted to a lower limit on the half-life by the following formula:

$$T_{1/2} = \frac{\ln(2) \times N_{Xe136}}{rate \times 365.2} \tag{7.4}$$

Where N_{Xe136} is the number of ^{136}Xe atoms in the XeLS. This can be calculated from the concentration listed in Table 7.1.

$$C_{Xe} = \frac{\text{mass of Xe in total XeLS}}{\text{mass of total XeLS}} \tag{7.5}$$

$$= \frac{745 \text{ kg}}{30.5 \text{ m}^3 \times 780.13 \text{ kg/m}^3} \times 100 \tag{7.6}$$

$$= 3.13 \pm 0.01 \text{ (wt\%)} \tag{7.7}$$

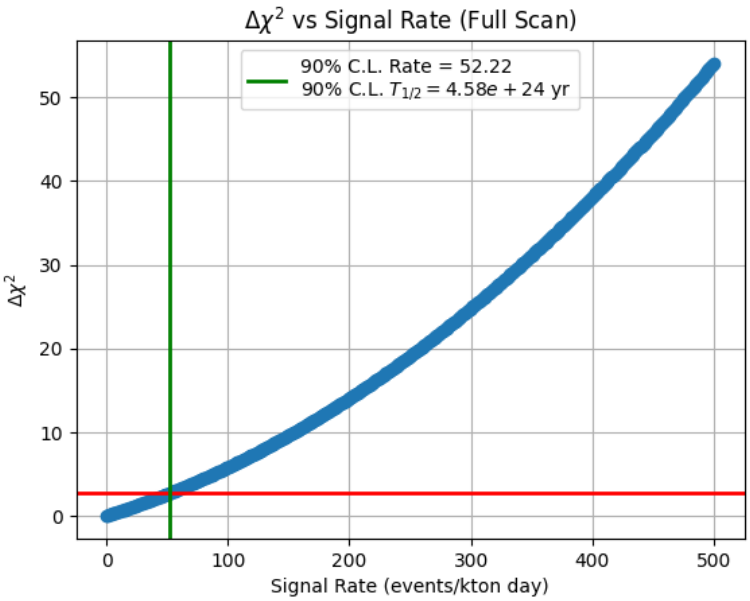

Figure 7·2: Difference in the NLL test statistic over fixed signal rates, the intersection with the Wilks' Theorem 1-parameter 90% C.L. threshold is shown.

$$\begin{aligned} N_{^{136}\mathrm{Xe}} &= (1\text{ kton} \times \text{concentration of Xe in XeLS} \times \text{ratio of } {}^{136}\mathrm{Xe}) \\ &\quad \times N_A/(\text{atomic mass number of mixed Xe}) \\ &= 3.13 \times 0.9085/135.80 \times 6.022 \times 10^{23} \\ &= (1.261 \pm 0.004) \times 10^{29}\ (\text{kton-XeLS})^{-1} \end{aligned} \tag{7.8}$$

Here, N_A is Avogrado's number. From these formulae, the upper limit on $2\nu\beta\beta^*$rate is converted to a lower limit on $2\nu\beta\beta^*$half-life.

However, the 90% C.L. given by Wilks' theorem is likely invalid for this analysis for two reasons. First, the signal rate parameter has a physical boundary at zero, violating the regularity conditions required by Wilks' theorem. Second, the χ^2 profile is not quadratic and falls sharply as the rate approaches zero, indicating that asymptotic approximations may not hold. For these reasons, the Wilks' theorem result should be considered a preliminary and potentially aggressive limit. A later section describes a more accurate determination using the Feldman-Cousins technique.

7.5.3 Feldman-Cousins Calculation

Given that Wilks' theorem conditions are likely not satisfied for this analysis, the upper limit on the $2\nu\beta\beta^*$rate is determined using the Feldman-Cousins (FC) approach. While Wilks' theorem would allow us to assume -2 log(likelihood ratio) follows a χ^2 distribution asymptotically, the FC method instead constructs confidence intervals by simulating the test statistic distribution under various hypothesized signal rates. This allows us to obtain proper 90% coverage intervals without relying on asymptotic approximations.

We perform the FC calculation by scanning over $2\nu\beta\beta^*$signal rates. At each signal rate hypothesis, multiple Toy MC datasets are generated with the best fit background levels. For each toy MC dataset, the fit is performed and the χ^2 test statistic value calculated.

7.5.4 Discussion

The Feldman-Cousins limit reveals that without additional inputs, this analysis is unable to set a world-leading limit on $2\nu\beta\beta^*$. Better characterization of detector response, and modeling of the film and KamLS backgrounds will allow us to use the full XeLS volume and improve the sensitivity of the analysis.

Chapter 8

Conclusions

8.1 Summary of the thesis

Time to get philosophical and wordy.

Important: In the list of references at the end of thesis, abbreviated journal and conference titles aren't allowed. Either you must put the full title in each item, or create a List of Abbreviations at the beginning of the references, with the abbreviations in one column on the left (arranged in alphabetical order), and the corresponding full title in a second column on the right. Some abbreviations, such as IEEE, SIGMOD, ACM, have become standardized and accepted by librarians, so those should not be spelled out in full.

Bibliography

[1] H. Ozaki. *High Sensitivity Search for Neutrinoless Double-Beta Decay in KamLAND-Zen with Double Amount of ^{136}Xe.* PhD thesis, Tohoku University, 2019.

[2] S. Abe, S. Asami, M. Eizuka, S. Futagi, A. Gando, Y. Gando, T. Gima, A. Goto, T. Hachiya, K. Hata, K. Hosokawa, K. Ichimura, S. Ieki, H. Ikeda, K. Inoue, K. Ishidoshiro, Y. Kamei, N. Kawada, Y. Kishimoto, M. Koga, M. Kurasawa, T. Mitsui, H. Miyake, T. Nakahata, K. Nakamura, R. Nakamura, H. Ozaki, T. Sakai, I. Shimizu, J. Shirai, K. Shiraishi, A. Suzuki, Y. Suzuki, A. Takeuchi, K. Tamae, H. Watanabe, Y. Yoshida, S. Obara, A. K. Ichikawa, S. Yoshida, S. Umehara, K. Fushimi, K. Kotera, Y. Urano, B. E. Berger, B. K. Fujikawa, J. G. Learned, J. Maricic, S. N. Axani, Z. Fu, J. Smolsky, L. A. Winslow, Y. Efremenko, H. J. Karwowski, D. M. Markoff, W. Tornow, S. Dell'Oro, T. O'Donnell, J. A. Detwiler, S. Enomoto, M. P. Decowski, K. M. Weerman, C. Grant, A. Li, and H. Song. Measurement of cosmic-ray muon spallation products in a xenon-loaded liquid scintillator with kamland. *Phys. Rev. C*, 107:054612, May 2023.

[3] J. J. Gomez-Cadenas, J. Martin-Albo, M. Mezzetto, F. Monrabal, and M. Sorel. The Search for neutrinoless double beta decay. *Riv. Nuovo Cim.*, 35(2):29–98, 2012.

[4] Michael Duerr, Manfred Lindner, and Alexander Merle. On the quantitative impact of the schechter-valle theorem. *JOURNAL OF HIGH ENERGY PHYSICS*, JHEP06, 2011.

[5] Jonathan Engel and Javier Menéndez. Status and Future of Nuclear Matrix Elements for Neutrinoless Double-Beta Decay: A Review. *Reports on Progress in Physics*, 80(4):046301, mar 2017.

[6] L. Jokiniemi, B. Romeo, C. Brase, J. Kotila, P. Soriano, A. Schwenk, and J. Menéndez. Two-neutrino $\beta\beta$ decay of 136xe to the first excited 0+ state in 136ba. *Physics Letters B*, 838:137689, 2023.

[7] Lotta Jokiniemi, Beatriz Romeo, Pablo Soriano, and Javier Menéndez. Neutrinoless $\beta\beta$-decay nuclear matrix elements from two-neutrino $\beta\beta$-decay data. *Phys. Rev. C*, 107:044305, Apr 2023.

[8] Daniel Castillo, Lotta Jokiniemi, Pablo Soriano, and Javier Menéndez. Neutrinoless $\beta\beta$ decay nuclear matrix elements complete up to n2lo in heavy nuclei. *Physics Letters B*, 860:139181, 2025.

[9] S. Abe, T. Araki, K. Chiba, T. Eda, M. Eizuka, Y. Funahashi, A. Furuto, A. Gando, Y. Gando, S. Goto, T. Hachiya, K. Hata, K. Ichimura, S. Ieki, H. Ikeda, K. Inoue, K. Ishidoshiro, Y. Kamei, N. Kawada, Y. Kishimoto, M. Koga, A. Marthe, Y. Matsumoto, T. Mitsui, H. Miyake, D. Morita, R. Nakajima, K. Nakamura, R. Nakamura, R. Nakamura, J. Nakane, T. Ono, H. Ozaki, K. Saito, T. Sakai, I. Shimizu, J. Shirai, K. Shiraishi, A. Suzuki, K. Tachibana, K. Tamae, H. Watanabe, K. Watanabe, S. Yoshida, S. Umehara, K. Fushimi, K. Kotera, Y. Urano, B. E. Berger, B. K. Fujikawa, J. G. Learned, J. Maricic, Z. Fu, S. Ghosh, J. Smolsky, L. A. Winslow, Y. Efremenko, H. J. Karwowski, D. M. Markoff, W. Tornow, S. Dell'Oro, T. O'Donnell, J. A. Detwiler, S. Enomoto, M. P. Decowski, K. M. Weerman, C. Grant, O. Penek, H. Song, A. Li, S. N. Axani, M. Garcia, and M. Sarfraz. Search for majorana neutrinos with the complete kamland-zen dataset. 2024.

[10] S. Al Kharusi, G. Anton, I. Badhrees, P.S. Barbeau, D. Beck, V. Belov, T. Bhatta, M. Breidenbach, T. Brunner, G.F. Cao, W.R. Cen, C. Chambers, B. Cleveland, M. Coon, A. Craycraft, T. Daniels, L. Darroch, S.J. Daugherty, J. Davis, S. Delaquis, A. Der Mesrobian-Kabakian, R. DeVoe, J. Dilling, A. Dolgolenko, M.J. Dolinski, J. Echevers, W. Fairbank Jr., D. Fairbank, J. Farine, S. Feyzbakhsh, P. Fierlinger, Y.S. Fu, D. Fudenberg, P. Gautam, R. Gornea, G. Gratta, C. Hall, E.V. Hansen, J. Hoessl, P. Hufschmidt, M. Hughes, A. Iverson, A. Jamil, C. Jessiman, M.J. Jewell, A. Johnson, A. Karelin, L.J. Kaufman, T. Koffas, R. Krücken, A. Kuchenkov, K.S. Kumar, Y. Lan, A. Larson, B.G. Lenardo, D.S. Leonard, G.S. Li, S. Li, Z. Li, C. Licciardi, Y.H. Lin, R. MacLellan, T. McElroy, T. Michel, B. Mong, D.C. Moore, K. Murray, O. Njoya, O. Nusair, A. Odian, I. Ostrovskiy, A. Perna, A. Piepke, A. Pocar, F. Retière, A.L. Robinson, P.C. Rowson, J. Runge, S. Schmidt, D. Sinclair, K. Skarpaas, A.K. Soma, V. Stekhanov, M. Tarka, S. Thibado, J. Todd, T. Tolba, T.I. Totev, R. Tsang, B. Veenstra, V. Veeraraghavan, P. Vogel, J.-L. Vuilleumier, M. Wagenpfeil, J. Watkins, M. Weber, L.J. Wen, U. Wichoski, G. Wrede, S.X. Wu, Q. Xia, D.R. Yahne, L. Yang, Y.-R. Yen, O.Ya. Zeldovich, T. Ziegler, and (EXO-200 Collaboration) . Search for two-neutrino double-beta decay of 136xe to the 0_1^+ excited state of 136ba with the complete exo-200 dataset. *Chinese Physics C*, 47(10):103001, oct 2023.

[11] S. Matsuda. *Search for Neutrinoless Double-Beta Decay in ^{136}Xe after Intensive Background Reduction with KamLAND-Zen.* PhD thesis, Tohoku University, 2016.

[12] A. Li. *The Tao and Zen of neutrinos: neutrinoless double beta decay in KamLAND-ZEN 800*. PhD thesis, Boston University, 2020.

[13] Stefano Dell'Oro, Simone Marcocci, and Francesco Vissani. New expectations and uncertainties on neutrinoless double beta decay. *Phys. Rev. D*, 90:033005, Aug 2014.

[14] Nufit 5.0. Nufit 5.0. available at http://www.nu-fit.org, 2020.

[15] S. Abe, T. Araki, K. Chiba, T. Eda, M. Eizuka, Y. Funahashi, A. Furuto, A. Gando, Y. Gando, S. Goto, T. Hachiya, K. Hata, K. Ichimura, S. Ieki, H. Ikeda, K. Inoue, K. Ishidoshiro, Y. Kamei, N. Kawada, Y. Kishimoto, M. Koga, A. Marthe, Y. Matsumoto, T. Mitsui, H. Miyake, D. Morita, R. Nakajima, K. Nakamura, R. Nakamura, R. Nakamura, J. Nakane, T. Ono, H. Ozaki, K. Saito, T. Sakai, I. Shimizu, J. Shirai, K. Shiraishi, A. Suzuki, K. Tachibana, K. Tamae, H. Watanabe, K. Watanabe, S. Yoshida, S. Umehara, K. Fushimi, K. Kotera, Y. Urano, B. E. Berger, B. K. Fujikawa, J. G. Learned, J. Maricic, Z. Fu, S. Ghosh, J. Smolsky, L. A. Winslow, Y. Efremenko, H. J. Karwowski, D. M. Markoff, W. Tornow, S. Dell'Oro, T. O'Donnell, J. A. Detwiler, S. Enomoto, M. P. Decowski, K. M. Weerman, C. Grant, O. Penek, H. Song, A. Li, S. N. Axani, M. Garcia, and M. Sarfraz. Search for majorana neutrinos with the complete kamland-zen dataset, 2024.

[16] H. Yoshida. *Limit on Majorana Neutrino Mass with Neutrinoless Double Beta Decay from KamLAND-Zen*. PhD thesis, Tohoku University, 2014.

[17] A. Takeuchi. *First Search for Majorana Neutrinos in the Inverted Mass Hierarchy Region with KamLAND-Zen*. PhD thesis, Tohoku University, 2023.

[18] H. Miyake. *Search for Neutrinoless Double-Beta Decay in KamLAND-ZEN Applying Improved Long-Lived Spallation Background Reduction*. PhD thesis, Tohoku University, 2023.

[19] L. Giot, J.A. Alcántara-Núñez, J. Benlliure, D. Pérez-Loureiro, L. Audouin, A. Boudard, E. Casarejos, T. Enqvist, J.E. Ducret, B. Fernández-Domínguez, M. Fernández Ordóñez, F. Farget, A. Heinz, V. Henzl, D. Henzlova, A. Kelić-Heil, A. Lafriaskh, S. Leray, P. Napolitani, C. Paradela, J. Pereira, M.V. Ricciardi, C. Stéphan, K.-H. Schmidt, C. Schmitt, L. Tassan-Got, C. Villagrasa, C. Volant, and O. Yordanov. Isotopic production cross sections of the residual nuclei in spallation reactions induced by 136xe projectiles on proton at 500mev. *Nuclear Physics A*, 899:116–132, 2013.

[20] P. Napolitani, K.-H. Schmidt, L. Tassan-Got, P. Armbruster, T. Enqvist, A. Heinz, V. Henzl, D. Henzlova, A. Kelić, R. Pleskač, M. V. Ricciardi, C. Schmitt, O. Yordanov, L. Audouin, M. Bernas, A. Lafriaskh, F. Rejmund,

C. Stéphan, J. Benlliure, E. Casarejos, M. Fernandez Ordonez, J. Pereira, A. Boudard, B. Fernandez, S. Leray, C. Villagrasa, and C. Volant. Measurement of the complete nuclide production and kinetic energies of the system ^{136}Xe+hydrogen at 1 gev per nucleon. *Phys. Rev. C*, 76:064609, Dec 2007.

[21] Matteo Agostini, Giovanni Benato, Jason A. Detwiler, Javier Menéndez, and Francesco Vissani. Toward the discovery of matter creation with neutrinoless $\beta\beta$ decay. *Rev. Mod. Phys.*, 95:025002, May 2023.

[22] Leslie Lamport. *LaTeX—A Document Preparation System—User's Guide and Reference Manual*. Addison-Wesley, 1985.

[23] W. Pauli. Dear radioactive ladies and gentlemen. *Phys. Today*, 31N9:27, 1978.

[24] C. L. Cowan, F. Reines, F. B. Harrison, H. W. Kruse, and A. D. McGuire. Detection of the free neutrino: a confirmation. *Science*, 124(3212):103–104, 1956.

[25] M. Grunewald et al. Precision electroweak measurements on the Z resonance. *Physics Reports*, 427(5):257–454, 2006.

[26] NobelPrize.org. The Nobel Prize in Physics 2015. `https://www.nobelprize.org/prizes/physics/2015/summary/`. Accessed: 2025-01-24.

[27] B. Pontecorvo. Mesonium and anti-mesonium. *Soviet Journal of Experimental and Theoretical Physics*, 6:429, 1957.

[28] Ivan Esteban, M. C. Gonzalez-Garcia, Michele Maltoni, Ivan Martinez-Soler, João Paulo Pinheiro, and Thomas Schwetz. NuFit-6.0: Updated Global Analysis of Three-Flavor Neutrino Oscillations. *Journal of High Energy Physics*, 2024(12), 2024.

[29] Alessandro Paoloni. Status of the JUNO experiment. *Proceeding of Science*, HQL2023:017, 2024.

[30] Ali Ajmi. Status of the Hyper-Kamiokande Experiment. *Proceeding of Science*, HQL2023:098, 2024.

[31] Inés Gil-Botella. The Deep Underground Neutrino Experiment (DUNE) Program. *Proceeding of Science*, ICHEP2024:165, 2025.

[32] M. Aker et al. Direct Neutrino-Mass Measurement With Sub-Electron Volt Sensitivity. *Nature Physics*, 18(2):160–166, 2022.

[33] A. Ashtari Esfahani, S. Böser, N. Buzinsky, M. C. Carmona-Benitez, C. Claessens, L. de Viveiros, P. J. Doe, M. Fertl, J. A. Formaggio, J. K. Gaison, L. Gladstone, M. Grando, M. Guigue, J. Hartse, K. M. Heeger, X. Huyan,

J. Johnston, A. M. Jones, K. Kazkaz, B. H. LaRoque, M. Li, A. Lindman, E. Machado, A. Marsteller, C. Matthé, R. Mohiuddin, B. Monreal, R. Mueller, J. A. Nikkel, E. Novitski, N. S. Oblath, J. I. Peña, W. Pettus, R. Reimann, R. G. H. Robertson, D. Rosa De Jesús, G. Rybka, L. Saldaña, M. Schram, P. L. Slocum, J. Stachurska, Y.-H. Sun, P. T. Surukuchi, J. R. Tedeschi, A. B. Telles, F. Thomas, M. Thomas, L. A. Thorne, T. Thümmler, L. Tvrznikova, W. Van De Pontseele, B. A. VanDevender, J. Weintroub, T. E. Weiss, T. Wendler, A. Young, E. Zayas, and A. Ziegler. Tritium Beta Spectrum Measurement and Neutrino Mass Limit from Cyclotron Radiation Emission Spectroscopy. *Physical Review Letters*, 131:102502, Sep 2023.

[34] Eleonora Di Valentino, Stefano Gariazzo, and Olga Mena. Most constraining cosmological neutrino mass bounds. *Physical Review D*, 104:083504, Oct 2021.

[35] Carlo Giunti and Chung W. Kim. *Fundamentals of Neutrino Physics and Astrophysics*. Oxford University Press, 03 2007.

[36] Sacha Davidson, Enrico Nardi, and Yosef Nir. Leptogenesis. *Physics Reports*, 466(4–5):105–177, September 2008.

[37] Wayne Hu and Scott Dodelson. Cosmic microwave background anisotropies. *Annual Review of Astronomy and Astrophysics*, 40(1):171–216, September 2002.

[38] M. Abdul Karim, J. Aguilar, S. Ahlen, S. Alam, L. Allen, C. Allende Prieto, O. Alves, A. Anand, U. Andrade, E. Armengaud, A. Aviles, S. Bailey, C. Baltay, P. Bansal, A. Bault, J. Behera, S. BenZvi, D. Bianchi, C. Blake, S. Brieden, A. Brodzeller, D. Brooks, E. Buckley-Geer, E. Burtin, R. Calderon, R. Canning, A. Carnero Rosell, P. Carrilho, L. Casas, F.J. Castander, M. Charles, E. Chaussidon, J. Chaves-Montero, D. Chebat, X. Chen, T. Claybaugh, S. Cole, A.P. Cooper, A. Cuceu, K.S. Dawson, A. de la Macorra, A. de Mattia, N. Deiosso, J. Della Costa, R. Demina, A. Dey, B. Dey, Z. Ding, P. Doel, J. Edelstein, D.J. Eisenstein, W. Elbers, P. Fagrelius, K. Fanning, E. Fernández-García, S. Ferraro, A. Font-Ribera, J.E. Forero-Romero, C.S. Frenk, C. Garcia-Quintero, L.H. Garrison, E. Gaztañaga, H. Gil-Marín, S. Gontcho A. Gontcho, D. Gonzalez, A.X. Gonzalez-Morales, C. Gordon, D. Green, G. Gutierrez, J. Guy, B. Hadzhiyska, C. Hahn, S. He, M. Herbold, H.K. Herrera-Alcantar, M.-F. Ho, K. Honscheid, C. Howlett, D. Huterer, M. Ishak, S. Juneau, N.V. Kamble, N.G. Karaçayl, R. Kehoe, S. Kent, A.G. Kim, D. Kirkby, T. Kisner, S.E. Koposov, A. Kremin, A. Krolewski, O. Lahav, C. Lamman, M. Landriau, D. Lang, J. Lasker, J.M. Le Goff, L. Le Guillou, A. Leauthaud, M.E. Levi, Q. Li, T.S. Li, K. Lodha, M. Lokken, F. Lozano-Rodríguez, C. Magneville, M. Manera, P. Martini, W.L. Matthewson, A. Meisner, J. Mena-Fernández, A. Menegas, T. Mergulhão, R. Miquel, J. Moustakas, A. Muñoz-Gutiérrez, D. Muñoz-Santos, A.D. Myers, S. Nadathur, K. Naidoo, L. Napolitano, J.A. Newman, G. Niz,

H.E. Noriega, E. Paillas, N. Palanque-Delabrouille, J. Pan, J.A. Peacock, M.P. Ibanez, W.J. Percival, A. Pérez-Fernández, I. Pérez-Ràfols, M.M. Pieri, C. Poppett, F. Prada, D. Rabinowitz, A. Raichoor, C. Ramírez-Pérez, M. Rashkovetskyi, C. Ravoux, J. Rich, A. Rocher, C. Rockosi, J. Rohlf, J.O. Román-Herrera, A.J. Ross, G. Rossi, R. Ruggeri, V. Ruhlmann-Kleider, L. Samushia, E. Sanchez, N. Sanders, D. Schlegel, M. Schubnell, H. Seo, A. Shafieloo, R. Sharples, J. Silber, F. Sinigaglia, D. Sprayberry, T. Tan, G. Tarlé, P. Taylor, W. Turner, L.A. Ureña-López, R. Vaisakh, F. Valdes, G. Valogiannis, M. Vargas-Magaña, L. Verde, M. Walther, B.A. Weaver, D.H. Weinberg, M. White, M. Wolfson, C. Yèche, J. Yu, E.A. Zaborowski, P. Zarrouk, Z. Zhai, H. Zhang, C. Zhao, G.B. Zhao, R. Zhou, and H. Zou. Desi dr2 results. ii. measurements of baryon acoustic oscillations and cosmological constraints. *Physical Review D*, 112(8), October 2025.

[39] M. Goeppert-Mayer. Double Beta-Disintegration. *Physical Review*, 48:512–516, Sep 1935.

[40] J. Kotila and F. Iachello. Phase-space factors for double-β decay. *Physical Review C*, 85:034316, Mar 2012.

[41] Mihai Horoi and Andrei Neacsu. Shell Model Study of Using an Effective Field Theory for Disentangling Several Contributions to Neutrinoless Double-β Decay. *Physical Review C*, 98:035502, Sep 2018.

[42] B. Pritychenko and V.I. Tretyak. Comprehensive Review of 2β decay half-lives. *Atomic Data and Nuclear Data Tables*, 161:101694, 2025.

[43] Jouni Suhonen and Joel Kostensalo. Double β Decay and the Axial Strength. *Frontiers in Physics*, 7, 2019.

[44] W. H. Furry. On Transition Probabilities in Double Beta-Disintegration. *Physical Review*, 56(12):1184, 12 1939.

[45] J. Schechter and J. W. F. Valle. Neutrinoless double-β decay in su(2)×u(1) theories. *Phys. Rev. D*, 25:2951–2954, Jun 1982.

[46] Lukáš Gráf, Sudip Jana, Oliver Scholer, and Nele Volmer. Neutrinoless double beta decay without vacuum majorana neutrino mass. *Physics Letters B*, 859:139111, 2024.

[47] M. Agostini, G. R. Araujo, A. M. Bakalyarov, M. Balata, I. Barabanov, L. Baudis, C. Bauer, E. Bellotti, S. Belogurov, A. Bettini, L. Bezrukov, V. Biancacci, D. Borowicz, E. Bossio, V. Bothe, V. Brudanin, R. Brugnera, A. Caldwell, C. Cattadori, A. Chernogorov, T. Comellato, V. D'Andrea, E. V. Demidova, N. Di Marco, E. Doroshkevich, F. Fischer, M. Fomina, A. Gangapshev,

A. Garfagnini, C. Gooch, P. Grabmayr, V. Gurentsov, K. Gusev, J. Hakenmüller, S. Hemmer, R. Hiller, W. Hofmann, J. Huang, M. Hult, L. V. Inzhechik, J. Janicskó Csáthy, J. Jochum, M. Junker, V. Kazalov, Y. Kermaïdic, H. Khushbakht, T. Kihm, I. V. Kirpichnikov, A. Klimenko, R. Kneißl, K. T. Knöpfle, O. Kochetov, V. N. Kornoukhov, P. Krause, V. V. Kuzminov, M. Laubenstein, A. Lazzaro, M. Lindner, I. Lippi, A. Lubashevskiy, B. Lubsandorzhiev, G. Lutter, C. Macolino, B. Majorovits, W. Maneschg, L. Manzanillas, M. Miloradovic, R. Mingazheva, M. Misiaszek, P. Moseev, Y. Müller, I. Nemchenok, K. Panas, L. Pandola, K. Pelczar, L. Pertoldi, P. Piseri, A. Pullia, C. Ransom, L. Rauscher, S. Riboldi, N. Rumyantseva, C. Sada, F. Salamida, S. Schönert, J. Schreiner, M. Schütt, A.-K. Schütz, O. Schulz, M. Schwarz, B. Schwingenheuer, O. Selivanenko, E. Shevchik, M. Shirchenko, L. Shtembari, H. Simgen, A. Smolnikov, D. Stukov, A. A. Vasenko, A. Veresnikova, C. Vignoli, K. von Sturm, T. Wester, C. Wiesinger, M. Wojcik, E. Yanovich, B. Zatschler, I. Zhitnikov, S. V. Zhukov, D. Zinatulina, A. Zschocke, A. J. Zsigmond, K. Zuber, and G. Zuzel. Final Results of GERDA on the Search for Neutrinoless Double-β Decay. *Physical Review Letters*, 125:252502, Dec 2020.

[48] E. Armengaud, C. Augier, A. S. Barabash, F. Bellini, G. Benato, A. Benoît, M. Beretta, L. Bergé, J. Billard, Yu. A. Borovlev, Ch. Bourgeois, V. B. Brudanin, P. Camus, L. Cardani, N. Casali, A. Cazes, M. Chapellier, F. Charlieux, D. Chiesa, M. de Combarieu, I. Dafinei, F. A. Danevich, M. De Jesus, T. Dixon, L. Dumoulin, K. Eitel, F. Ferri, B. K. Fujikawa, J. Gascon, L. Gironi, A. Giuliani, V. D. Grigorieva, M. Gros, E. Guerard, D. L. Helis, H. Z. Huang, R. Huang, J. Johnston, A. Juillard, H. Khalife, M. Kleifges, V. V. Kobychev, Yu. G. Kolomensky, S. I. Konovalov, A. Leder, P. Loaiza, L. Ma, E. P. Makarov, P. de Marcillac, R. Mariam, L. Marini, S. Marnieros, D. Misiak, X.-F. Navick, C. Nones, E. B. Norman, V. Novati, E. Olivieri, J. L. Ouellet, L. Pagnanini, P. Pari, L. Pattavina, B. Paul, M. Pavan, H. Peng, G. Pessina, S. Pirro, D. V. Poda, O. G. Polischuk, S. Pozzi, E. Previtali, Th. Redon, A. Rojas, S. Rozov, C. Rusconi, V. Sanglard, J. A. Scarpaci, K. Schäffner, B. Schmidt, Y. Shen, V. N. Shlegel, B. Siebenborn, V. Singh, C. Tomei, V. I. Tretyak, V. I. Umatov, L. Vagneron, M. Velázquez, B. Welliver, L. Winslow, M. Xue, E. Yakushev, M. Zarytskyy, and A. S. Zolotarova. New Limit for Neutrinoless Double-Beta Decay of ^{100}Mo from the CUPID-Mo Experiment. *Physical Review Letters*, 126:181802, May 2021.

[49] D. Q. Adams, C. Alduino, K. Alfonso, F. T. Avignone, O. Azzolini, G. Bari, F. Bellini, G. Benato, M. Beretta, M. Biassoni, A. Branca, C. Brofferio, C. Bucci, J. Camilleri, A. Caminata, A. Campani, L. Canonica, X. G. Cao, S. Capelli, C. Capelli, L. Cappelli, L. Cardani, P. Carniti, N. Casali, E. Celi, D. Chiesa, M. Clemenza, S. Copello, O. Cremonesi, R. J. Creswick, A. D'Addabbo, I. Dafinei, F. Del Corso, S. Dell'Oro, S. Di Domizio, S. Di Lorenzo, V. Dompè,

D. Q. Fang, G. Fantini, M. Faverzani, E. Ferri, F. Ferroni, E. Fiorini, M. A. Franceschi, S. J. Freedman, S. H. Fu, B. K. Fujikawa, S. Ghislandi, A. Giachero, A. Gianvecchio, L. Gironi, A. Giuliani, P. Gorla, C. Gotti, T. D. Gutierrez, K. Han, E. V. Hansen, K. M. Heeger, R. G. Huang, H. Z. Huang, J. Johnston, G. Keppel, Yu. G. Kolomensky, R. Kowalski, R. Liu, L. Ma, Y. G. Ma, L. Marini, R. H. Maruyama, D. Mayer, Y. Mei, S. Morganti, T. Napolitano, M. Nastasi, J. Nikkel, C. Nones, E. B. Norman, A. Nucciotti, I. Nutini, T. O'Donnell, M. Olmi, J. L. Ouellet, S. Pagan, C. E. Pagliarone, L. Pagnanini, M. Pallavicini, L. Pattavina, M. Pavan, G. Pessina, V. Pettinacci, C. Pira, S. Pirro, S. Pozzi, E. Previtali, A. Puiu, S. Quitadamo, A. Ressa, C. Rosenfeld, S. Sangiorgio, B. Schmidt, N. D. Scielzo, V. Sharma, V. Singh, M. Sisti, D. Speller, P. T. Surukuchi, L. Taffarello, F. Terranova, C. Tomei, K. J. Vetter, M. Vignati, S. L. Wagaarachchi, B. S. Wang, B. Welliver, J. Wilson, K. Wilson, L. A. Winslow, S. Zimmermann, and S. Zucchelli. New Direct Limit on Neutrinoless Double Beta Decay Half-Life of ^{128}Te with CUORE. *Physical Review Letters*, 129:222501, Nov 2022.

[50] D. Gooding. *Enhancing the Neutrinoless Double Beta Decay Sensitivity of SNO+ with Deep Learning.* PhD thesis, Boston University, 2025.

[51] A. Belley, C. G. Payne, S. R. Stroberg, T. Miyagi, and J. D. Holt. Ab Initio Neutrinoless Double-Beta Decay Matrix Elements for ^{48}Ca, ^{76}Ge, and ^{82}Se. *Physical Review Letters*, 126:042502, Jan 2021.

[52] M. Horoi, A. Neacsu, and S. Stoica. Statistical analysis for the neutrinoless double-β-decay matrix element of ^{48}Ca. *Phys. Rev. C*, 106:054302, Nov 2022.

[53] Lotta Jokiniemi, Beatriz Romeo, Pablo Soriano, and Javier Menéndez. Neutrinoless $\beta\beta$-decay nuclear matrix elements from two-neutrino $\beta\beta$-decay data. *Phys. Rev. C*, 107(4):044305, 2023.

[54] Y. Karino. *Improvement of Background Rejection for Cosmic Muon Spallation in KamLAND-Zen.* PhD thesis, Tohoku University, 2017.

[55] T. Hachiya. e^+/e^- Discrimination in KamLAND. *Proceedings of the 10th International Workshop on Neutrino-Nucleus Interactions in Few-GeV Region (NuInt15)*, 2016.

[56] S. Abe, S. Enomoto, K. Furuno, Y. Gando, H. Ikeda, K. Inoue, Y. Kibe, Y. Kishimoto, M. Koga, Y. Minekawa, T. Mitsui, K. Nakajima, K. Nakajima, K. Nakamura, M. Nakamura, I. Shimizu, Y. Shimizu, J. Shirai, F. Suekane, A. Suzuki, Y. Takemoto, K. Tamae, A. Terashima, H. Watanabe, E. Yonezawa, S. Yoshida, A. Kozlov, H. Murayama, J. Busenitz, T. Classen, C. Grant, G. Keefer, D. S. Leonard, D. McKee, A. Piepke, T. I. Banks, T. Bloxham, J. A. Detwiler, S. J. Freedman, B. K. Fujikawa, F. Gray, E. Guardincerri, L. Hsu, K. Ichimura,

R. Kadel, C. Lendvai, K. B. Luk, T. O'Donnell, H. M. Steiner, L. A. Winslow, D. A. Dwyer, C. Jillings, C. Mauger, R. D. McKeown, P. Vogel, C. Zhang, B. E. Berger, C. E. Lane, J. Maricic, T. Miletic, M. Batygov, J. G. Learned, S. Matsuno, S. Pakvasa, J. Foster, G. A. Horton-Smith, A. Tang, S. Dazeley, K. E. Downum, G. Gratta, K. Tolich, W. Bugg, Y. Efremenko, Y. Kamyshkov, O. Perevozchikov, H. J. Karwowski, D. M. Markoff, W. Tornow, K. M. Heeger, F. Piquemal, J. S. Ricol, and M. P. Decowski. Production of radioactive isotopes through cosmic muon spallation in kamland. *Phys. Rev. C*, 81:025807, Feb 2010.

[57] P. Antonioli, C. Ghetti, E.V. Korolkova, V.A. Kudryavtsev, and G. Sartorelli. A three-dimensional code for muon propagation through the rock: Music. *Astroparticle Physics*, 7(4):357–368, 1997.

[58] Y. Kamei. *Hunting Massive Majoron Emission in Neutrinoless Double-Beta Decay of ^{136}Xe with KamLAND-Zen.* PhD thesis, Tohoku University, 2021.

[59] Brookhaven National Laboratory National Nuclear Data Center. Evaluated nuclear structure data file (ensdf). webpage.

[60] E665 Collaboration, M.R. Adams, M. Aderholz, and et al. Production of charged hadrons by positive muons on deuterium and xenon at 490 gev. *Z. Phys. C – Particles and Fields*, 61:179–198, 1994.

CURRICULUM VITAE

Hasung Song

Department of Physics
Boston University
Email: hwsong@bu.edu

Education

- **Ph.D. in Physics**, Boston University, 2019–Present
- **M.Sc. in Physics**, Boston University, 2019–2022
- **B.Sc. in Physics**, University of California, Berkeley, 2016-2018

Professional Experience

- **Post-Baccalaureate Researcher**, University of California, Berkeley, 2018–2019

Selected Publications

- "Search for Majorana Neutrinos with the Complete KamLAND-Zen Dataset" KamLAND-Zen Collaboration, arXiv:2406.11438 [hep-ex] (2024)
- "Eos: conceptual design for a demonstrator of hybrid optical detector technology" T. Anderson et al. JINST 18 P02009 (2023)
- "KamNet: An integrated spatiotemporal deep neural network for rare event searches in KamLAND-Zen" A. Li, et al. Phys. Rev. C 107, 014323 (2023)
- "RFSoC-based front-end electronics for pulse detection" S.N. Axani et al. 2024 JINST 19 P03013 (2024)
- "Search for the Majorana Nature of Neutrinos in the Inverted Mass Ordering Region with KamLAND-Zen" KamLAND-Zen Collaboration, Phys. Rev. Lett. 130, 051801 (2023)

Scientific Collaborations

- EoS Collaboration 2023–Present
- NuDOT Collaboration 2022–Present
- KamLAND Collaboration 2020–Present
- NIM+ 2020–2021
- Mu2E Collaboration 2018–2019

Conferences and Presentations

- "Getting Excited About Double Beta Decay in KamLAND-Zen", APS DNP, Talk, Boston, MA, 2024.
- "Understanding KamNet Performance in KamLAND-ZEN with ML Interpretability", SLAC Summer Institute, Poster, SLAC, 2023.
- "KamLAND-Zen's New ML Tricks", Neutrino Physics and Machine Learning, Talk, Northeastern University, 2023.
- "Rejecting Spallation Backgrounds in KamLAND-ZEN with KamNet", Neutrino, Poster, Seoul, Korea, 2022.
- "Rejecting Spallation Backgrounds in KamLAND-ZEN with KamNet", TAUP, Poster, Valenica, Spain, 2021.
- "Neutrinoless Muon-to-Positron Conversion at Mu2e", APS April Meeting, Talk, Denver, Colorado, 2019.

Teaching Experience

- Physics 211 General Physics I, Teaching Assistant, Boston University, Summer 2020.
- Physics 211 General Physics I, Teaching Assistant, Boston University, Fall 2019.

Professional Service

- Member, Graduate Student Council, Boston University Physics Department, 2019–Present.